Measurement of the forward-backward asymmetry of Z boson decays in electron-positron pairs with the ATLAS detector in proton-proton collisions at $\sqrt{s} = 7$ TeV at the LHC

Dissertation zur Erlangung des Grades
DOKTOR DER NATURWISSENSCHAFTEN
am Fachbereich 08: Physik, Mathematik und Informatik der Johannes Gutenberg-Universität in Mainz

von
Sebastian König
geboren in Hagen (Westf.)

Mainz, den 2. Dezember 2013

Abstract

In this thesis the measurement of the effective weak mixing angle $\sin^2\theta_W^{\text{eff}}$ in proton-proton collisions is described. The results are extracted from the forward-backward asymmetry (A_{FB}) in electron-positron final states at the ATLAS experiment at the LHC. The A_{FB} is defined upon the distribution of the polar angle between the incoming quark and outgoing lepton. The signal process used in this study is the reaction $pp \to Z/\gamma^* + X \to e^+e^- + X$ taking a total integrated luminosity of $4.8\,\text{fb}^{-1}$ of data into account. The data was recorded at a proton-proton center-of-mass energy of $\sqrt{s} = 7\,\text{TeV}$. The weak mixing angle is a central parameter of the electroweak theory of the Standard Model (SM) and relates the neutral current interactions of electromagnetism and weak force. The higher order corrections on $\sin^2\theta_W^{\text{eff}}$ are related to other SM parameters like the mass of the Higgs boson.

Because of the symmetric initial state constellation of colliding protons, there is no favoured forward or backward direction in the experimental setup. The reference axis used in the definition of the polar angle is therefore chosen with respect to the longitudinal boost of the electron-positron final state. This leads to events with low absolute rapidity have a higher chance of being assigned to the opposite direction of the reference axis. This effect called dilution is reduced when events at higher rapidities are used. It can be studied including electrons and positrons in the forward regions of the ATLAS calorimeters. Electrons and positrons are further referred to as electrons. To include the electrons from the forward region, the energy calibration for the forward calorimeters had to be redone. This calibration is performed by inter-calibrating the forward electron energy scale using pairs of a central and a forward electron and the previously derived central electron energy calibration. The uncertainty is shown to be dominated by the systematic variations.

The extraction of $\sin^2\theta_W^{\text{eff}}$ is performed using χ^2 tests, comparing the measured distribution of A_{FB} in data to a set of template distributions with varied values of $\sin^2\theta_W^{\text{eff}}$. The templates are built in a forward folding technique using modified generator level samples and the official fully simulated signal sample with full detector simulation and particle reconstruction and identification. The analysis is performed in two different channels: pairs of central electrons or one central and one forward electron. The results of the two channels are in good agreement and are the first measurements of $\sin^2\theta_W^{\text{eff}}$ at the Z resonance using electron final states at proton-proton collisions at $\sqrt{s} = 7\,\text{TeV}$. The precision of the measurement is already systematically limited mostly by the uncertainties resulting from the knowledge of the parton distribution functions (PDF) and the systematic uncertainties of the energy calibration.

The extracted results of $\sin^2\theta_W^{\text{eff}}$ are combined and yield a value of $\sin^2\theta_{W\,\text{comb}}^{\text{eff}} = 0.2288 \pm 0.0004(\text{stat.}) \pm 0.0009(\text{syst.}) = 0.2288 \pm 0.0010(\text{tot.})$. The measurements are compared to the results of previous measurements at the Z boson resonance. The deviation with respect to the combined result provided by the LEP and SLC experiments is up to 2.7 standard deviations.

Kurzfassung

In dieser Arbeit wird die Messung des effectiven schwachen Mischungswinkels $\sin^2\theta_W^{\text{eff}}$ in Proton-Proton-Kollisionen beschrieben. Die Resultate werden aus der Vorwärts-Rückwärts-Asymmetrie (A_{FB}) der Verteilung des Polarwinkels in Elektron-Positron-Endzuständen im ATLAS-Experiment am LHC extrahiert. Der Signalprozess, der in dieser Studie genutzt wird, ist die Reaktion $pp \to Z/\gamma^* + X \to e^+e^- + X$ unter Berücksichtigung der totalen integrierten Luminosität der Daten von $4{,}8\,\text{fb}^{-1}$. Die Daten wurden bei Proton-Proton Schwerpunksenergien von $\sqrt{s} = 7\,\text{TeV}$ aufgenommen. Der schwache Mischungswinkel is ein zentraler Parameter der elektroschwachen Theorie des Standardmodells und verbinded die Kopplung der neutralen Ströme von Elektromagnetismus und der schwachen Kraft. Korrekturen höherer Ordnung, die zu $\sin^2\theta_W^{\text{eff}}$ beitragen, beinhalen Abhängigkeiten von weiteren SM-Parametern, wie der Masse des Higgs-Bosons.

Wegen der symmetrischen Anfangsbedingungen der kollidierenden Protonen gibt es keine bevorzugte Vorwärts- oder Rückwärtsrichtung in diesem experimentellen Aufbau. Die Referenzachse, die zur Definition des Polarwinkels dient, wird daher im Bezug auf den longitudinalen Boost des Elektron-Positronendzustands definiert. Dies führt dazu, dass für Ereignisse mit einer niedrigen absoluten Rapidität eine höhere Chance besteht, die entgegengesetzte Richtung der Referenzachse zu wählen. Dieser Effekt, der mit “dilution” bezeichnet wird, fällt bei höheren Rapiditäten geringer aus. Er kann unter Hinzunahme der Elektronen und Positronen aus den Vorwärtsregionen der ATLAS-Kalorimeter untersucht werden. Elektronen und Positronen werden im Weiteren als Elektronen zusammengefasst. Um diese Elektronen in den Vorwärtsregionen zu benutzen, muss die Energiekalibraion für die Vorwärtskalorimeter neu bestimmt werden. Diese Kalibration wird durchgeführt, indem die bekannte Energiekalibration der zentralen Elektronen angewendet wird und Paare aus einem Zentralelektron und einem Vorwärtselektron zur Extraktion der Kalibrationskonstanten herangezogen werden. Es wird gezeigt, dass die Unsicherheiten durch die in Betracht gezogenen systematischen Unsicherheiten dominiert sind.

Die Extraktion von $\sin^2\theta_W^{\text{eff}}$ wird mit Hilfe von χ^2-Tests durchgeführt, in denen die gemessene A_{FB} Verteilung aus Daten mit einem Satz von A_{FB} Template-Verteilungen verglichen werden, in denen der Wert von $\sin^2\theta_W^{\text{eff}}$ variiert wird. Die Templates werden mit Hilfe einer Vorwärtsfaltungstechnik aus Datensätzen auf Generatorebene und den vollständig simulierten signal Datensatz hergestellt, in dem sowohl der Detektor als auch die Teilchenrekonstruktion und -identifikation simuliert sind. Die Analyse wird in zwei Kanälen durchgeführt: Paare von Zentralelektronen oder einem Zentral- und einem Vorwärtselektron. Die Resultate der beinen Kanäle stimmen gut miteinander überein und sind die ersten Messungen von $\sin^2\theta_W^{\text{eff}}$ an der Z-Resonanz, in denen Elektronenendzustände in Proton-Proton-Kollisionen bei $\sqrt{s} = 7\,\text{TeV}$ analysiert werden. Die Präzision der Messung ist bereits systematisch limitiert und hauptsächlich durch die Kenntnis der Parton-Verteilungsfunktionen (PDF) und systematische Unsicherheiten der Energiekalibration gegeben.

Die gemessenen Werte von $\sin^2\theta_W^{\text{eff}}$ werden miteinander kombiniert und ergeben $\sin^2\theta_{W\,\text{comb}}^{\text{eff}} = 0.2288 \pm 0.0004(\text{stat.}) \pm 0.0009(\text{syst.}) = 0.2288 \pm 0.0010(\text{tot.})$. Diese Ergebnisse werden mit Resultaten früherer Messungen an der Z-Bosonresonanz verglichen. Die Abweichung zum kombinierten Messwert der LEP und SLC Experimente beträgt dabei bis zu 2,7 Standardabweichungen.

Contents

1. Introduction

The Standard Model (SM) of particle physics is a theoretical concept that uses a gauge invariant formalism to describe the interaction of quantised point-like objects with each other, that build the forces and matter constituents of the known universe. Of the four fundamental forces the three that are dominant at the subatomic scale are described by the SM. Only gravity is not included in the gauge invariant formalism of the SM as of today. The forces are mediated by gauge bosons while the matter particles are represented as fermions in the Standard Model. The forces that are described by the SM are the strong nuclear force, the electromagnetic force and the weak force, of which the latter two are successfully unified in the electroweak force. The matter particles, that are found to be realised in three families, can be divided in two groups that differ by the forces they are related to. The quarks are interacting with the strong and electroweak forces while the leptons are only related to the electroweak force.

The following observations are a personal list of highlights in the discovery of new particles and the measurement of particles and parameters of the SM at leading particle physics experiments at their time: The experimental observations on which the Standard Model is evaluated, go back to the findings of fundamental relations between the numerous particles, that were discovered in the 1960s. At that time a "zoo" of particles was discovered in experimental studies, that could be included in a systematic way by Gell-Mann and Zweig [1]. The static quark model could describe the new findings as hadrons, which are bound states of fundamental particles called quarks. In this model the quarks can be combined to mesons (quark anti-quark bound states) or baryons (tri-quark or tri-anti-quark bound states). By expanding on the possible set of bound states, the Ω^- baryon, that had not yet been seen, could be predicted and finally discovered in 1964 [2].

In later experiments for example in 1979 at the PETRA (Positron-Elektron-Tandem-Ring-Anlage) accelerator at DESY (Deutsches Elektron-SYnchrotron) in Hamburg, Germany, events could be detected, that consisted of three decay products in the same interaction. This let to the discovery of the gluon [3, 4, 5, 6], the gauge boson mediating the strong nuclear force. In 1983 at the Sp$\bar{\text{p}}$S (Super Proton Anti-Proton Synchrotron) located at CERN (Conseil Européen pour la Recherche Nucléaire[1]), Switzerland, the particles mediating the weak force, the $W^{\pm}$ and Z^0-boson, could also be produced and measured in resonant production [7, 8]. Using the knowledge of the Sp$\bar{\text{p}}$S, the Tevatron was built and sequentially improved at the Fermilab in Batavia, IL, USA. It was run at center of mass energies of 1.8 - 1.9 TeV from 1987 until end of 2011 and managed to discover the heaviest known fundamental particle - the top quark - in 1995 at the CDF and DØ experiments [9, 10]. These experiments also performed the currently most precise measurement of the W boson mass so far [11].

In the mean time the newly built Large Electron Positron collider (LEP) at CERN was finished and collected data from 1989 - 2000. The collision energies in the first run (LEP I) were adjusted to scan the resonance of the Z^0-boson. At the ALEPH [12], DELPHI [13], L3 [14] and OPAL [15] experiments at LEP I and at the SLAC Large Detector (SLD) [16] at the SLAC Linear Collider (SLC) at Stanford Linear Accelerator Center (SLAC), Stanford, CA, USA, the properties of the Z^0-boson were determined at very

[1] European council for nuclear research

high precision [17]. The SLC was operated from 1992 - 1998 delivering collisions for the SLD. At LEP the energies were raised in the LEP II program above the threshold of on-shell W-boson pair production to study the W-boson and to look for events in which a Higgs boson [18] was produced. The properties of the charged current interaction could be studied in detail but no evidence for a Standard Model Higgs boson was found at LEP until the LEP II program ended in the year 2000.

Finally on July 4$^{\text{th}}$, 2012 the ATLAS [19] and CMS [20] experiment at the Large Hadron Collider (LHC) at CERN, that started its physics program in 2010 could claim the discovery of the Higgs boson, the last missing particle of the Standard Model [21, 22]. Additionally the Nobel Prize in Physics 2013 was awarded to Peter Higgs and Franọis Englert "for the theoretical discovery of a mechanism that contributes to our understanding of the origin of mass of subatomic particles, and which recently was confirmed through the discovery of the predicted fundamental particle, by the ATLAS and CMS experiments at CERNs Large Hadron Collider" [23].

The measurement of the mixing angle of the weak and electromagnetic force has been performed at different experiments and scales. The most precise results are obtained by the LEP and SLC experiments using hadronic final states [17] at the Z^0-boson resonance. The two results with the highest precision of the experiments at each of these colliders show a disagreement of about three standard deviations with respect to one another. This leads to the question if either one of the experiments is right and the other is wrong or if both of them are varying from a true value of $\sin^2\theta_W^{\text{eff}}$ that would then most likely be close to the average of their results. Also the relation of this SM parameter to e.g. the mass of the Higgs-boson implies that both individual results are showing tensions, while the combined result is in agreement with the predictions from global fits on the parameters of the Standard Model.

The extraction of $\sin^2\theta_W^{\text{eff}}$ has also been performed at the CDF and DØ experiments at the Tevatron [24, 25, 26, 27], setting the currently most precise results at hadron colliders for the extraction at the Z^0-resonance. These two studies were performed in electron final states and are limited in precision by the available data statistics. At the LHC the CMS collaboration was the first publishing the results of the extraction of the weak mixing angle from muon pairs in proton-proton collisions. This measurement was also using events at the resonance of the Z^0-boson but published their findings with a limited amount of $1\,\text{fb}^{-1}$ of 2011 data.

The study discussed in this thesis is the first analysis performed in electron final states at a proton-proton collider. Here electron refers to electrons as well as positrons. It is part of a combined analysis effort on behalf of the ATLAS collaboration, performing the weak mixing angle extraction in one muon and two electron final state selections, where the electron channels differ in kinematic conditions. It can be shown that the precision that is obtainable in this setup is limited by systematic uncertainties. These uncertainties are dominated by variations within the parton distribution functions. The analysis discussed in this thesis is direct contribution to the preliminary results shown at the DIS 2013 conference [28]. On behalf of this an publication is currently in preparation.

This thesis is giving a brief theory overview in chapter 2, introducing the fundamental relations of the Standard Model and defining the reference frame in which the study is performed. Here the electroweak theory is introduced in which the weak mixing angle is defined. In chapter 3 the experimental setup is described, giving detailed information about relevant components of the ATLAS detector that are mainly used for the determination of other final states and describing briefly the other components in the experiment. Chapter 4 describes the conditions of the 2011 data recording and introduces the event simulation procedure and the relevant simulated physics processes. In chapter 5 the commonly used definition of electrons within the ATLAS collaboration is introduced. This includes the properties of the reconstruction identification and trigger routines available for electron signatures. Chapter 6 is showing the baseline event selection used in this study. Also the recommended preselections and calibrations for

data and simulated samples are mentioned. For the use of electrons in the forward calorimeter regions the energy calibration had to be re-optimized. This is discussed in chapter 7. The estimate of contributions to the electron selection originating from multijet processes is not feasible with the simulation approach. Therefor it is discussed in chapter 8 how these processes are estimated from data using relaxed identification requirements in an orthogonal selection. Here the resulting data and Monte Carlo distributions are compared including the data driven multijet estimates. Chapter 9 shows the raw distributions of the forward backward asymmetry (A_{FB}) and introduces the systematic variations that are studied. In chapter 10 the template method is introduced, which is used to extract the weak mixing angle $\sin^2\theta_W^{\text{eff}}$ from the asymmetry distribution. Finally the results of the analysis are compared to the measurements of previous experiments. Chapter 11 concludes the discussions in this thesis and gives an outlook towards the perspectives of a continuation of the measurement with the later data set recorded in 2012 and after the long shut down of the LHC in the years 2013-2015.

2. Theory

In this chapter the Standard Model (SM) of high energy particle physics is introduced. The fundamental forces and constituents described by the SM are discussed as well as the possibility to measure the particles of the SM in high energy particle physics (HEP) experiments. Especially the setup of hadron or parton colliders is introduced. Finally the motivation and underlying calculations of the forward-backward asymmetry (A_{FB}) of the Z^0-boson and its relation to the effective weak mixing angle $\sin^2\theta_W^{\text{eff}}$ of the electroweak theory within the Standard Model is given.

2.1. Standard Model in particle physics

The Standard Model of particle physics has been developed within the last decades and is a very powerful and inclusive model of its kind. It includes the very precise description of three out of the four fundamental forces that are related to particle physics [29, 30, 31]. With the Standard Model the elementary point-like constituents of mater can be categorized in two groups, that are distinguished by their spin. The bosons (integral spin) mediate the fundamental forces, where as the fermions (half-integral spin) build up the ordinary matter. These fermions are interacting with one another only by the exchange of bosons.

The bosons can be categorised in terms of the elementary forces they are related to. The photon (γ) is related to the electromagnetic interaction, while the $W^{\pm}$-bosons mediate the charged weak force. The Z^0-boson, that mediates the neutral weak force, and the set of eight gluons (g) of the strong interaction complete the set of bosons related to the three fundamental forces. One more fundamental gauge boson that does not directly relate to a fundamental force but is responsible for the propagation of masses is the Higgs boson (H).

The fermions are divided in two groups of three families each. The leptons carry integral charges and interact with the bosons of the weak force. Depending whether the charge of the lepton is non-zero they are also interacting with the photons of the electromagnetic interaction. The quarks on the other hand carry third-integral charges and interact additionally to the electromagnetic and weak force also with the gluons of the strong force. The interaction with the gluons is related to the fact that the quarks as well as the gluons carry a quantity called color-charge that relates to the strong interaction. A summary of the important quantum numbers of the fermions is given in Tab. 2.1 while their masses are listed in Tab. 2.2.

The SM is a gauge theory with the symmetry group $SU(3)_{color} \times SU(2)_L \times U(1)_Y$. This symmetry group is not an exact symmetry but is spontaneously broken on the "electroweak scale" at about 1 TeV to $SU(3)_{color} \times U(1)_{em}$. The related mechanism is described in Sec. 2.1.2.

The Lagrange function of the Standard Model is of the form:

$$\mathcal{L}_{SM} = \mathcal{L}_{QCD} + \mathcal{L}_{EW}. \tag{2.1.1}$$

particle	1st family	2nd family	3rd family	Q/e	Y	$\lvert\vec{I}\rvert$	I_3
leptons	$\begin{pmatrix}\nu_e\\ e\end{pmatrix}_L$	$\begin{pmatrix}\nu_\mu\\ \mu\end{pmatrix}_L$	$\begin{pmatrix}\nu_\tau\\ \tau\end{pmatrix}_L$	0	-1	1/2	1/2
				-1	-1	1/2	$-1/2$
	e_R	μ_R	τ_R	-1	-2	0	0
quarks	$\begin{pmatrix}u\\ d\end{pmatrix}_L$	$\begin{pmatrix}c\\ s\end{pmatrix}_L$	$\begin{pmatrix}t\\ b\end{pmatrix}_L$	2/3	1/3	1/2	1/2
				$-1/3$	1/3	1/2	$-1/2$
	u_R	c_R	t_R	2/3	4/3	0	0
	d_R	s_R	b_R	$-1/3$	$-2/3$	0	0

Table 2.1.: Fermions of the Standard Model with the related quantum numbers for charge, hyper-charge and weak iso-spin [32].

particle	1st family		2nd family		3rd family		Q/e
leptons	ν_e	< 2 eV	ν_μ	< 2 eV	ν_τ	< 2 eV	0
	e	0.511 MeV	μ	105.7 MeV	τ	1.777 GeV	-1
quarks	u	1.5 - 3.3 MeV	c	1.27 GeV	t	171.2 GeV	2/3
	d	3.5 - 6.0 MeV	s	$\sim$ 104 MeV	b	4.20 GeV	$-1/3$

Table 2.2.: Fermions of the Standard Model with the related mass measurements. In the SM neutrinos are further treated massless [32].

The first term in this function describes the theory of the strong interaction, called quantum chromodynamics (QCD) [33], which is discussed in Sec. 2.1.1. The second term describes the electroweak interaction which is explained in Sec. 2.1.2.

In the following there is no distinction made between the set of particles and their corresponding set of anti-particle partners. If not stated otherwise the name of the particles relates to the particle as well as the anti-particle. Further in the discussion below natural units[1] are used.

2.1.1. Strong interaction

In quantum chromodynamics the interaction of particles with respect to their color-charge is described. This includes the quarks from the side of the fermions and the gluons from the side of the bosons. The symmetry group the theory is based on is the $SU(3)_{color}$. The Lagrange function of the QCD has the form

[1] In natural units: $\hbar \equiv c \equiv k_B \equiv 1$

gauge bosons	symbol	spin	masses / GeV	Q/e	interaction
$W^\pm$-boson	$W^\pm$	1	80.398	± 1	weak
Z^0-boson	Z^0	1	91.188	0	electroweak
photons	γ	1	0	0	electromagnetic
gluon	g	1	0	0	strong
Higgs	H	0	$\sim$125	0	– (mass propagation)

Table 2.3.: Gauge bosons of the Standard Model with their properties of mass, charge and the related interaction [32].

$$\mathcal{L}_{QCD} = \left[\bar{q}(\imath\gamma^{\mu}\partial_{\mu})q\right] - \imath g_s(\bar{q}\gamma^{\mu}T_a q)G^a_{\mu} - \frac{1}{4}G^a_{\mu\nu}G^{\mu\nu}_a \tag{2.1.2}$$

using the field strength tensor

$$G^a_{\mu\nu} = \partial_{\mu}G^a_{\nu} - \partial_{\nu}G^a_{\mu} - g_s f^a_{bc}G^b_{\mu}G^c_{\nu}. \tag{2.1.3}$$

Here q and $\bar{q}$ are the quarks and anti-quark wave functions respectively, g_s is the strong coupling constant. Further ∂_{μ} is the covariant derivative and T_a is the non-Abelian generator of the $SU(3)_{color}$. Its commutator defines the structural constants f_{abc} with $(a, b, c = 1, \ldots, 8)$ to be:

$$[T_a, T_b] = \imath f_{abc}T_c, \text{ with } T_a = \frac{\lambda_a}{2}. \tag{2.1.4}$$

The λ_a are called the three dimensional Gell-Mann matrices [1]. The term in (2.1.2) that is set in parentheses is the kinetic term of the fermions and is to appear only once in the combined Lagrange function (2.1.1). For completeness it is used here but belongs to the fermion Lagrange function (2.1.13) defined below. In the QCD self interaction is possible due to the fact that the gluons, as mediators of the interaction, carry a color charge themselves. This leads to the fact that its coupling strength is increasing with distance. The confinement, that cannot be described in a perturbative theory, is the result of the self coupling. In contrast to that, high energetic quarks and gluons in bound systems can be treated as "asymptotically free". Here the strength of the coupling is weak enough to measure and calculate the scattering of individual quarks and gluons. Further the role of the t-quark is special in this respect as well. It has a life time that is short enough to decay to a b-quark and a W-boson, before it can be confined in a bound state. Therefore it is the only quark found to be unconfined in the current measurements.

The bound states that are described by the QCD are required to provide a neutral color charge to be stable. This can be realized by the combination of a quark and an anti-quark of the correspondingly same color (anti-) charge. These bound states are called mesons. The lightest and most frequently found mesons are pions and kaons denoted by the symbols π and K. These mesons can be built electrically charged as well as in neutral state. There is no stable state for them, so all mesons decay. Depending on their constituents and binding energies, the decay products can either be lighter mesons, photons or lepton pairs via a strong or electroweak interaction.

Additionally it is possible to combine quarks and anti-quarks in sets of three quarks or three anti-quarks. This way the bound states have to consist of (anti-)quarks with all three different color charges to build a color charge neutral state. These bound states are called baryons. Protons and neutrons are two examples of the lightest baryons realized in nature.

2.1.2. Electroweak interaction

The theory of the electroweak interaction as part of the Standard Model belongs to the symmetry group $SU(2)_L \times U(1)_Y$. The $SU(2)_L$ describes the weak interaction while the $U(1)_Y$ relates a coupling to the hyper-charge. The weak interaction only takes into account left-handed particles (and right-handed anti-particles) which is indicated by the index $_L$ of the respective symmetry group. This feature is described by the properties of the weak iso-spin. Left-handed fermions are only found in iso-spin-doublets with values for the weak iso-spin of $|\vec{I}| = \frac{1}{2}$ and $I_3 = \pm\frac{1}{2}$. Right-handed particles are identified as iso-spin-singlets with $|\vec{I}| = I_3 = 0$.

The generator of the $U(1)_Y$ is the hyper-charge Y, that is related to the electrical charge Q by the Gell-Mann-Nishijima relation $Q = I_3 + \frac{Y}{2}$.

The respective Lagrange function has to be invariant under transformations of the $SU(2)_L \times U(1)_Y$ group, which leads to four vector fields that are needed. There is the iso-spin-triplet $W^i_\mu (i = 1, 2, 3)$ that couples with the constant g to the weak iso-spin, while the vector field B_μ couples with g' to the hyper-charge. The Lagrange function of the electroweak theory can be structured in the following components:

$$\mathcal{L}_{EW} = \mathcal{L}_{Gauge} + \mathcal{L}_{Fermion} + \mathcal{L}_{Higgs} + \mathcal{L}_{Yukawa}. \tag{2.1.5}$$

The first term includes the kinetic term of the gauge bosons

$$\mathcal{L}_{Gauge} = -\frac{1}{4} B_{\mu\nu} B^{\mu\nu} - \frac{1}{4} W^a_{\mu\nu} W^{\mu\nu}_a, \tag{2.1.6}$$

where the field strength tensors have the form

$$B_{\mu\nu} = \partial_\mu B_\nu - \partial_\nu B_\mu \tag{2.1.7}$$

$$W^a_{\mu\nu} = \partial_\mu W^a_\nu - \partial_\nu W^a_\mu - g\varepsilon^a_{bc} W^b_\mu W^c_\nu. \tag{2.1.8}$$

Here ϵ_{abc} is the total antisymmetric tensor that builds the structure constant of the $SU(2)_L$. B_μ and W^i_μ are not the physical fields that are visible in nature ($W^\pm$, Z^0 and γ). These are rotations of the respective fields $W^{1,2}_\mu$, as well as W^3_μ and B_μ. The latter two are the neutral fields that rotate with

$$Z^0_\mu = -B_\mu \sin\theta_W + W^3_\mu \cos\theta_W \tag{2.1.9}$$

$$A_\mu = B_\mu \cos\theta_W + W^3_\mu \sin\theta_W \tag{2.1.10}$$

into the Z^0-boson and the photon field A_μ. The angle θ_W is defined to be the weak mixing angle or Weinberg-angle, named after Steven Weinberg [30, 31], that relates to the amount of mixing in the rotation of the fields.

The charged gauge bosons are represented by a rotation of the components W^1_μ and W^2_μ of the iso-spin-triplet

$$W^\pm_\mu = \frac{1}{\sqrt{2}} \left(W^1_\mu \mp \imath W^2_\mu \right). \tag{2.1.11}$$

The physical neutral gauge bosons couple to left-handed as well as to right-handed particles while the charged gauge bosons of the electroweak interaction only couple to left-handed particles. The electrical charge is related to the electroweak coupling constants in the following way:

$$g \sin\theta_W = g' \cos\theta_W = e. \tag{2.1.12}$$

The second term in the Lagrange function (2.1.5) describes the kinetic term of the fermions and its coupling to the gauge bosons:

$$\mathcal{L}_{Fermion} = \bar{L}(\imath D^L_\mu \gamma^\mu) L + \bar{R}(\imath D^R_\mu \gamma^\mu) R. \tag{2.1.13}$$

Here D^L_μ and D^R_μ are the two covariant derivatives

$$D^L_\mu = \partial_\mu - \imath g' B_\mu Y - \imath g W^a_\mu T^a \tag{2.1.14}$$

$$D^R_\mu = \partial_\mu - \imath g' B_\mu Y. \tag{2.1.15}$$

The difference between left- (L) and right-handed (R) fermions is made because of the different coupling of the gauge bosons to them. These fermions are behaving according to a structure that combines vector- (V) and axial-vector (A) operators that follow the structure V-A. Therefor the theory is also referred to as "V-A-theory". To relate to the observed couplings of the weak interaction, projection operators are defined with respect to the helicity of the fermions. These projectors are built by insertion of terms including the antisymmetric Dirac matrix γ_5 in the form $\mathcal{P}_L = \frac{1}{2}(1-\gamma_5)$ and $\mathcal{P}_R = \frac{1}{2}(1+\gamma_5)$. This way the dirac spinors of the leptons $l = e, \mu, \tau$ and the corresponding neutrinos ν_l are interacting with the weak fields in their projected form.

$$L^l = \frac{1}{2}(1-\gamma_5)\begin{pmatrix}\nu_l\\ l\end{pmatrix} = \begin{pmatrix}\nu_l\\ l\end{pmatrix}_L, \qquad R^l = \frac{1}{2}(1+\gamma_5)l^- = l^-_R. \tag{2.1.16}$$

Within the electroweak theory the physical gauge bosons can be described, but by this theory the masses of the gauge bosons would have to be zero as mass terms of the form $\frac{1}{2}M_A^2 A_\mu A^\mu$ would not be *locally gauge invariant* [2]. Because the electroweak gauge bosons are measured to be massive (see Tab. 2.3), the related symmetry can not be exact. The electroweak theory has to be a broken symmetry. A way to introduce a symmetry breaking mechanism that keeps the other features of the electroweak theory intact can be explained by spontaneous symmetry breaking that is related to the Higgs-mechanism [18].

2.1.3. Spontaneous Symmetry Breaking and the Higgs-mechanism

To include the spontaneously broken symmetry into the electroweak theory, a scalar doublet has to be introduced to the Lagrange function:

$$\mathcal{L}_{Higgs} = (D^L_\mu \Phi)^\dagger (D^\mu_L \Phi) - V(\Phi). \tag{2.1.17}$$

Here $\Phi = \binom{\Phi^+}{\Phi^0}$, the doublet of complex scalar fields has to have a potential of the form:

$$V(\Phi) = -\mu^2 \Phi^\dagger \Phi + \lambda(\Phi^\dagger \Phi)^2. \tag{2.1.18}$$

The potential $V(\Phi)$ is invariant under local gauge transformation of the SM. It has a degenerate ground state with $\mu^2 < 0$ and $\lambda > 0$: $\Phi^\dagger\Phi = -\frac{\mu^2}{2}\lambda = v^2$. v is the vacuum expectation value (VEV). By choosing the ground state to be $\langle\Phi\rangle = \frac{1}{\sqrt{2}}\binom{0}{v}$ the $SU(2)_L \times U(1)_Y$ symmetry is broken towards $U(1)_{em}$. Performing an expansion around v only a single complex scalar field remains:
$H(x)$, the Higgs-field

$$\Phi(x) = \frac{1}{\sqrt{2}}\begin{pmatrix}0\\ v + H(x)\end{pmatrix}. \tag{2.1.19}$$

The other three degrees of freedom are absorbed into three of the electroweak gauge bosons and represent the degree of freedom of mass of these three bosons.

When performing the covariant derivative

$$D_\mu\langle\Phi\rangle = -\left[\frac{ig}{2}\begin{pmatrix}W^3_\mu & W^1_\mu - iW^2_\mu\\ W^1_\mu + iW^2_\mu & -W^3_\mu\end{pmatrix} + \frac{ig'}{2}B_\mu\right]\frac{1}{\sqrt{2}}\begin{pmatrix}0\\ v\end{pmatrix} \tag{2.1.20}$$

[2] local gauge invariance is a basic requirement of a renormalizable gauge theory

the choice of the VEV ground state and the parametrisation of the mixing of the gauge fields lead to the mass terms:

$$(D_\mu\langle\Phi\rangle)^\dagger(D_\mu\langle\Phi\rangle) = \frac{1}{4}v^2g^2W_\mu^+W^{-\mu} + \frac{1}{4}v^2(g^2+g'^2)Z_\mu^0Z^{0\mu}. \tag{2.1.21}$$

In (2.1.21) there are now terms that go quadratically in the fields and can therefor be interpreted as mass terms. As there is no term for the photon field A_μ the photon stays massless. With the specific choice of the VEV the resulting terms are locally gauge invariant under the symmetry group $U(1)_{em}$. The corresponding generator for this gauge group is the charge Q. Further the masses of the gauge bosons can be directly read off of (2.1.21). These result in:

$$M_W^2 = \frac{1}{4}v^2g^2, \qquad M_Z^2 = \frac{1}{4}v^2(g^2+g'^2), \qquad M_\gamma^2 = 0. \tag{2.1.22}$$

With (2.1.12) this concludes in a mass ratio of the gauge bosons $W^\pm$ and Z^0 at tree level that is directly related to the value of the weak mixing angle:

$$\frac{M_W}{M_Z} = \cos\theta_W. \tag{2.1.23}$$

Also the mass terms for the fermions are not gauge invariant under local gauge transformation on their own. A coupling of the Higgs-doublet to the fermions is needed to introduce gauge invariant fermion mass terms. The last term of (2.1.5) describes the so called Yukawa-couplings:

$$\mathcal{L}_{Yukawa} = -Y_d^{ij}\bar{L}^i\Phi R_d^j - Y_u^{ij}\bar{L}^i(\imath\tau_2\Phi^\dagger)R_u^j + h.c.. \tag{2.1.24}$$

Here it has to be noted that $L^{i,j}$ describes the left-handed fermion doublet while $R_f^{i,j}$ represents the right-handed fermion singlet for the fermions of type i and j respectively. With this the summing also has to be performed with respect to all $f \in \{u, d\}$, *up*- and *down*-type of fermion states. Therefor Y_f is the respective *up*- and *down*-type Yukawa-coupling and τ_2 is the second Pauli-matrix.

The Higgs-boson was recently discovered by the ATLAS [19, 21] and CMS [20, 22] experiment at the Large-Hadron-Collider in mid 2012. It is found to be at a mass of about 125 GeV and looks to be compatible with the predictions of the Standard Model. Additionally the Nobel Prize in Physics 2013 was awarded to Peter Higgs and Franşois Englert "for the theoretical discovery of a mechanism that contributes to our understanding of the origin of mass of subatomic particles, and which recently was confirmed through the discovery of the predicted fundamental particle, by the ATLAS and CMS experiments at CERNs Large Hadron Collider" [23].

2.2. Hadron collider phenomenology

At hadron colliders mostly protons or anti-protons are brought to collision at distinct interaction points. In contrast to the collision of electrons, which are fundamental particles, at higher collision energies the hadrons are not interacting with one another as a whole. The scattering processes are relative to the constituents of the hadrons called partons. For this reason in hadron collisions not the full center of mass energy of the hadrons s is available for the hard scattering processes, but the center of mass energy of the colliding partons $\hat{s}$.

In 1970 the idea was developed by Drell and Yan [35] to apply the parton model of deep inelastic scattering to specific hadron-hadron interactions. This is shown in Fig. 2.1. The initial process was

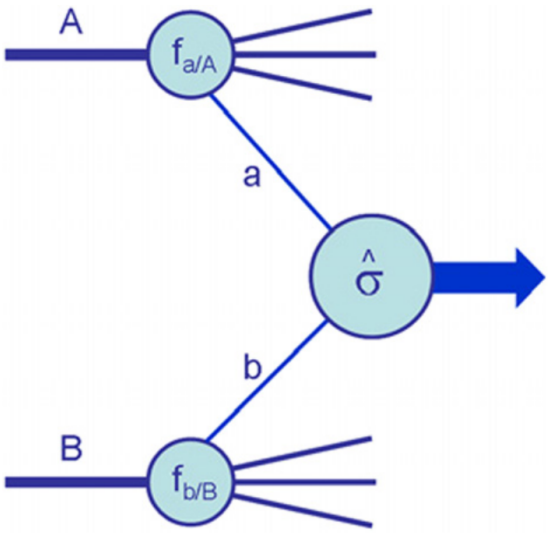

Figure 2.1.: Figure of a hard scatter process. The incoming hadrons are labeled with A and B, the scattering partons are labeled with a and b. The momentum fractions $x_{a,b}$ are described by the PDFs $f_{a,b/A,B}(x_{a,b}, Q^2)$.[34]

the production of a massive lepton pair from quark-anti-quark annihilation. It was postulated that the hadronic cross section $\sigma(AB \to \ell\bar{\ell} + X)$ can be described by weighting the sub-process $\hat{\sigma}(q\bar{q} \to \ell\bar{\ell})$ with the parton distribution functions (PDF) $f_{q/A}(x_q, Q^2)$. Here the PDF are derived from deep inelastic scattering processes:

$$\sigma_{AB} = \int dx_a dx_b f_{a/A}(x_a, Q^2) f_{b/B}(x_b, Q^2) \hat{\sigma}_{ab\to Y}. \tag{2.2.1}$$

In this "Drell-Yan process" the lepton pair $\ell\bar{\ell}$ corresponds to Y while a, b are the initial quarks $q\bar{q}$. Further $x_{a,b}$ is the momentum fraction of the partons a, b of the respective hadron A, B. The momentum transfer Q^2 that is also present in the PDF corresponds to the momentum scale of the hard process and is related to $M^2_{\ell\bar{\ell}}$.

In the simplest Drell-Yan process the quark-anti-quark pair annihilates to a virtual photon $q\bar{q} \to \gamma^* \to \ell\bar{\ell}$. At higher center of mass energies the production of the heavy gauge bosons $W^\pm$ and Z^0 is possible as well. In this scheme the electroweak gauge bosons could be discovered and directly measured in resonant production by the UA1 and UA2 experiments a CERN in 1983 [7, 8].

The cross section of a lepton pair via a massive photon can be calculated from a fundamental process of quantum electrodynamics (QED) $e^+e^- \to \mu^+\mu^-$ and the derived process $e^+e^- \to q\bar{q}$. It is proportional to the electromagnetic coupling strength, to the fine structure constant α^2 and the square of the charges of the quarks produced in the process. The four momenta of the incoming quarks can be chosen ignoring the transverse components producing a head-on collision with:

$$\mathrm{p}_1^\mu = \frac{\sqrt{s}}{2}(x_1, 0, 0, x_1), \qquad \mathrm{p}_2^\mu = \frac{\sqrt{s}}{2}(x_2, 0, 0, -x_2). \tag{2.2.2}$$

The $x_{1,2}$ are identical to the $x_{a,b}$ in the PDFs above. With this the hadronic and partonic center of mass energies reduce to $\hat{s} = x_1 x_2 \cdot s$. The rapidity of a particle can be expressed by $y = \frac{1}{2}\ln\left(\frac{E+\mathrm{p}_z}{E-\mathrm{p}_z}\right)$, if the

particle is described by a four vector of the type $p^\mu = (E_\mathrm{T}\cosh y, \mathrm{p_T}\sin\varphi, \mathrm{p_T}\cos\varphi, E_\mathrm{T}\sinh y)$. With this the transverse components of E and p are defined by $\mathrm{p_T} = \mathrm{p}\sin\theta$ and $E_\mathrm{T} = \sqrt{\mathrm{p_T}^2 + m^2}$. So for particles for which their mass is negligible with respect to their momentum, these particles can be treated massless and their transverse energy and momentum can be assumed equal. The rapidity is additive under Lorentz-transformation, so for the lepton pairs as in (2.2.2) the rapidity results in $y = \frac{1}{2}\ln(x_1/x_2)$, which leads to the momentum fractions:

$$x_{1,2} = \frac{M}{\sqrt{s}} e^{\pm y}. \tag{2.2.3}$$

Aside from the Drell-Yan process of course there are also other processes that e.g. only consider or are dominated by the strong interaction respectively. This includes e.g. processes that are described by the perturbative strong interaction (pQCD). Here the scattering of the incoming partons can result again in a pair of outgoing partons. These $2 \to 2$ parton processes are a dominant reaction at parton colliders.

Because of the structure of QCD the emitted partons are seeding the formation of hadrons with other partons that are produced by the potential of the color fields between the partons. These hadornised form of the emitted partons is called a jet. It contains collections of hadronic bound states that are boosted in the same direction as the original parton. The hadronisation of the initial partons depends on the radiation of quark-anti-quark pairs and gluons from the potential of the color fields between the partons. Here not all partons that are produced to form the hadrons in the jets have to be emitted collinear with the initial partons. The radiation of "hard" high energetic gluons can form non-collinear jet emissions in the hadronisation step.

2.2.1. Parton Distribution Functions

As introduced above the Parton Distribution Functions (PDF) are used to describe the probabilities to find certain partons of flavor q including gluons with a momentum fraction x of the hadron in a process at the momentum transfer scale Q. Assuming a process at the scale $Q^2 = M^2$ with a center of mass energy of 7 TeV is producing an on shell Z^0-boson at $M_Z = 91\,\mathrm{GeV}$ with a rapidity of $y_Z = 2.5$, the momentum fractions of the two quarks can be expected to have values of about:

$$x_{1,2} = \frac{91\,\mathrm{GeV}}{7\,\mathrm{TeV}} e^{\pm 2.5} = \begin{cases} 0.1584 \\ 0.0011 \end{cases}. \tag{2.2.4}$$

This can also be read off a corresponding diagram as shown in Fig. 2.2. It shows the available kinematic reach of partons produced in processes at a scale of $Q^2 = M^2$ and a center of mass energy of 7 TeV that can be produced by the LHC in conditions of the 2011 data taking.

The PDF that are used in the generation of signal and background events are derived from various measurements of particle collision or fixed target experiments and theoretical constraints. For the use of experimental results from previous measurements the DGLAP equations [32] are used to evolve the measured relations to the phase space of a new experiment e.g. the LHC experiments. This implies that the measurement uncertainties also have to be propagated and the resulting prediction of the given PDF gets the more biased by these uncertainties the more the measurements and the point in the (x, Q^2) plane are apart. Therefor the PDF sets, that are evaluated by various groups, have intrinsic systematic uncertainties that have to be taken into account when performing new measurements.

In particular towards lower values of parton momentum fraction x and higher momentum transfers Q^2 the extrapolation uncertainty is in general larger than the combined level of systematic uncertainties in the

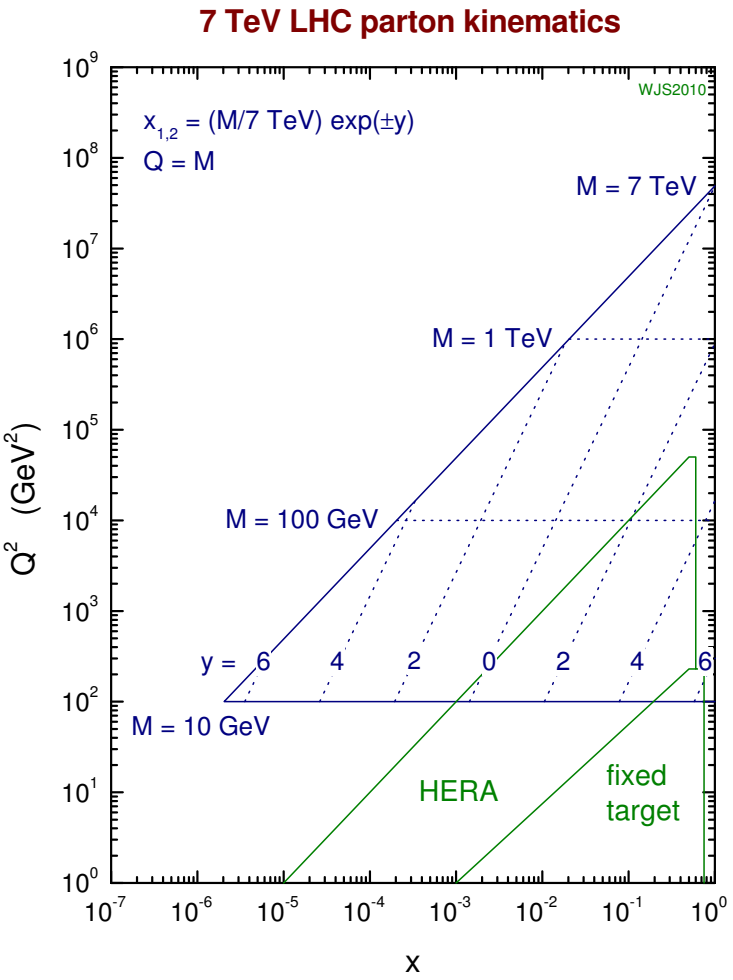

Figure 2.2.: Relation of x, Q^2 and M^2 respectively at the nominal center of mass energies of the LHC of 7 TeV. As comparison the available regions in phase space covered by fixed-target experiments and the HERA-collider are shown [34, 36].

previously tested regime. To provide good coverage of the known measurements the PDF sets of the competing PDF groups are evaluated using a set of input parameters that provide the current starting values of a PDF fit. These input parameters are combined to create a new set of orthogonal parameters, in which the uncertainties of the corresponding PDF are parametrised. The resulting systematic uncertainty on a derived quantity can be estimated by a combination of the variation of individual eigenvectors according to their uncertainties. This recipe is recommended by the *CTEQ* [37] as well as the *MRST/MSTW* [38] PDF groups. PDF sets of both groups are used in this study.

2.3. Measuring $\sin^2\theta_W^{\text{eff}}$ from A_{FB}

The electroweak interaction in the Standard Model is represented by a vector - axial-vector structure. In an electroweak neutral current process like $q\bar{q} \to Z/\gamma^* \to \ell^+\ell^-$, this leads to different couplings of fermions with respect to anti-fermions to the exchange particle. When having a look at the relevant terms of the differential cross section for the parton-level process with respect to the decay angle θ, these terms

can be written, at lowest order, as

$$\frac{\mathrm{d}\sigma}{\mathrm{d}\cos\theta} = \frac{4\pi\alpha^2}{3\hat{s}}\left[\frac{3}{8}\mathcal{A}(1+\cos^2\theta) + \mathcal{B}\cos\theta\right]. \tag{2.3.1}$$

Herein terms appear that are symmetric in θ and contribute to the integrated cross section ($\mathcal{A}$) and others that go with the cosine of the decay angle θ ($\mathcal{B}$), that vanish when calculating the integrated cross section. With these terms an asymmetry with respect to the forward and backward direction of θ can be defined as:

$$A_{FB} \equiv \frac{\int_0^1 \frac{\mathrm{d}\sigma}{\mathrm{d}\cos\theta}\,\mathrm{d}\cos\theta - \int_{-1}^0 \frac{\mathrm{d}\sigma}{\mathrm{d}\cos\theta}\,\mathrm{d}\cos\theta}{\int_{-1}^1 \frac{\mathrm{d}\sigma}{\mathrm{d}\cos\theta}\,\mathrm{d}\cos\theta} = \frac{\sigma_F - \sigma_B}{\sigma_F + \sigma_B} = \frac{\mathcal{B}}{\mathcal{A}}. \tag{2.3.2}$$

The terms $\mathcal{A}$ and $\mathcal{B}$ that go with the even and odd powers of $\cos\theta$ in (2.3.1) and (2.3.2) are containing the coupling strengths of the electromagnetic and weak force as well as the charges of the related fermions. They act as a form factor of the interaction. $\mathcal{A}$ and $\mathcal{B}$ are related to the electroweak coupling constants and can be written as:

$$\mathcal{A} = Q_l^2 Q_q^2 + 2Q_l Q_q\, g_V^q g_V^l\, \mathrm{Re}\left(\chi(s)\right) + \left(\left(g_V^l\right)^2 + \left(g_A^l\right)^2\right)\left(\left(g_V^q\right)^2 + \left(g_A^q\right)^2\right)|\chi(s)|^2 \tag{2.3.3}$$

$$\mathcal{B} = \frac{3}{2}\, g_A^q g_A^l\, \left(Q_l Q_q\, \mathrm{Re}\left(\chi(s)\right) + 2 g_V^q g_V^l\, |\chi(s)|^2\right) \tag{2.3.4}$$

with

$$\chi(s) = \frac{1}{\sin^2\theta_W \cos^2\theta_W}\,\frac{s}{s - m_Z^2 + \imath\Gamma_Z m_Z}. \tag{2.3.5}$$

Here $Q_{l,q}$ are the charges of the leptons and quarks, while $g_{V,A}^{l,q}$ represent the vector and axial-vector couplings of leptons and quarks, respectively.

2.3.1. Collins-Soper-Reference-Frame

In hadron collisions the reference axis in the definition of the angle θ has to be chosen properly. Here the fact that the incoming particles can carry transverse momenta has to be taken into account with the definition of the reference system. Fig. 2.3 shows aside from the ideal scenario also the cases where one of the incoming quarks in the parton collision carries a transverse momentum component and introduces the constellation in the Collins-Soper Reference-Frame (CS frame). In the approach evaluated by Collins and Soper [39] the event is boosted to a frame in which the transverse momentum components of the partons are symmetrized and balanced out.

Additional to the transverse momentum ambiguity, that is solved by using the CS frame, in the beam setup producing symmetrical proton-proton collisions, the knowledge of the direction of the incoming quark and anti-quark is remaining unknown. By taking a look at the PDF, the probability to coincide the direction of the incoming quark with the boson momentum direction is larger with rising absolute boson rapidity. This is a result of the constellation of high momentum fraction of a valence-quark from one proton with a corresponding sea-anti-quark from the other proton involved in the collision. Because of this, the sign of the decay angle in the CS frame is chosen to be corrected by the sign of the longitudinal momentum component $\mathrm{p_z}\,(\ell^+\ell^-)$ of the dilepton system.

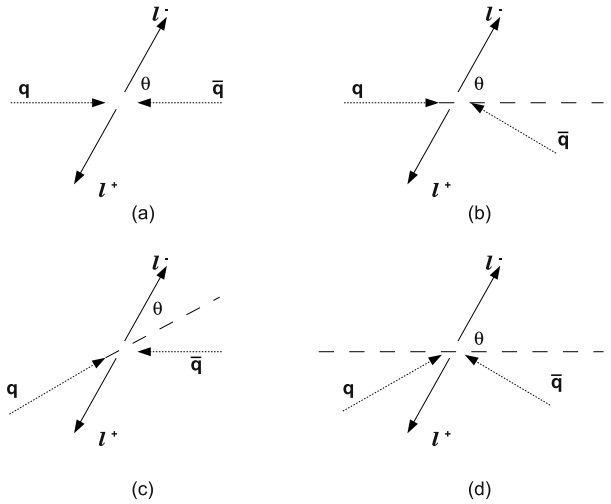

Figure 2.3.: The Collins-Soper reference frame. When the incoming partons do not have any transverse momentum, as shown in (a), the angle of the resulting lepton can be uniquely defined. On the other hand, an ambiguity exists in the definition in the case where one of the partons has non-zero transverse momentum, as in (b) and (c). The Collins-Soper reference frame (d) resolves the ambiguity by choosing an axis that is symmetric with respect to the two incoming partons. The figure is provided to the analysis [28] by Andrea Di Simone (private communication).

The calculation of $\cos\theta^*_{CS}$ in the Collins-Soper reference frame is defined on the lepton four-vectors only:

$$\cos\theta^*_{CS} = \frac{\mathrm{p_z}\left(\ell^+\ell^-\right)}{\left|\mathrm{p_z}\left(\ell^+\ell^-\right)\right|} \frac{2\left(\mathrm{p}_1^+\mathrm{p}_2^- - \mathrm{p}_1^-\mathrm{p}_2^+\right)}{m\left(\ell^+\ell^-\right)\sqrt{m\left(\ell^+\ell^-\right)^2 + \mathrm{p_T}\left(\ell^+\ell^-\right)^2}} \tag{2.3.6}$$

with

$$\mathrm{p}_i^\pm = \frac{1}{\sqrt{2}}\left(E_i \pm \mathrm{p}_{z,i}\right) \tag{2.3.7}$$

Here the four-momentum components are chosen to be calculated from the lepton ($i = 0$) and the anti-lepton ($i = 1$) respectively to correctly construct the distribution of $\cos\theta^*_{CS}$. The events with $\cos\theta^*_{CS} > 0$ are defined as forward (F), while those with $\cos\theta^*_{CS} < 0$ are called backward (B). Considering this, the asymmetry is defined to be:

$$A_{FB} = \frac{N_{\cos\theta^*_{CS}\geq 0} - N_{\cos\theta^*_{CS}<0}}{N_{\cos\theta^*_{CS}\geq 0} + N_{\cos\theta^*_{CS}<0}} = \frac{N_F - N_B}{N_F + N_B} \tag{2.3.8}$$

analogue to the generic definition in (2.3.2).

2.3.2. Previous measurements of $\sin^2\theta_W^{\text{eff}}$

From the spectra of A_{FB} with respect to other kinematic observables such as the invariant boson mass different Standard Model parameters can de extracted. One important parameter of these is the weak mixing angle $\sin^2\theta_W$. At tree level calculations it is expressed by the ratio of the vector and axial-vector

couplings of the fermions f in the electroweak interaction $g^f_{A/V,tree}$. Depending on the scale of the tree level process the set of fermions f can be limited:

$$\frac{g^f_{V,tree}}{g^f_{A,tree}} = 1 - 4|Q_f| \sin^2 \theta_W. \tag{2.3.9}$$

Here Q_f is the charge of the respective fermions taken into account. At tree level this can alternatively be expressed by the ratio of the W and Z-boson masses. When taking into account corrections to the propagation of the electroweak bosons that is introduced by so called loop diagrams to e.g. the Z-boson propagator, this relation has to be modified. The corrections introduced in the loop calculations [40, 41] result in:

$$\frac{g^f_V}{g^f_A} = 1 - 4|Q_f| \sin^2 \theta^{\text{eff}}_W. \tag{2.3.10}$$

The extraction of $\sin^2 \theta^{\text{eff}}_W$ can be performed at different energy scales (Q^2) but most frequently the results at the Z-boson resonance are quoted for reference. The most precise results from previous measurements have been obtained by the experiments at LEP and SLC [17]. The combination of their results yield an average value of $\sin^2 \theta^{\text{eff}}_W = 0.23153 \pm 0.00016$. This number is driven by the two measurement channels of the combined analysis of the forward backward asymmetry in b-quark final states ($A^{0,b}_{FB}$) at the LEP experiments ($\sin^2 \theta^{\text{eff}}_W = 0.23221 \pm 0.00029$) and the calculation of the *leptonic* left right asymmetry (A_l) at the SLD experiment ($\sin^2 \theta^{\text{eff}}_W = 0.23098 \pm 0.00026$). These results differ by $\sim 3\,\sigma$ from one another. Also each of these two measurements has pulls of $\sim 2\,\sigma$ from the world average [32] ($\sin^2 \theta^{\text{eff}}_W = 0.23146 \pm 0.00012$) that is dominated in precision by the two results above.

The measurement and comparison of $\sin^2 \theta^{\text{eff}}_W$ among different channels and experiments is further one more complication as the values of $\sin^2 \theta^{\text{eff}}_W$ depend on the type of fermion involved in the measured signal process. Especially the different strength of the higher order QCD corrections result in different values of the effective mixing angle for quark vertices with respect to the angle for lepton vertices:

$$\sin^2\theta^{u}_{\text{eff}} = \sin^2\theta^{\ell}_{\text{eff}} - 0.0001 \tag{2.3.11}$$
$$\sin^2\theta^{d}_{\text{eff}} = \sin^2\theta^{\ell}_{\text{eff}} - 0.0002 \tag{2.3.12}$$
$$\sin^2\theta^{b}_{\text{eff}} = \sin^2\theta^{\ell}_{\text{eff}} - 0.0014 \tag{2.3.13}$$

In events obtained in current parton colliders the influence of the events from b-quarks is small on the production side, as these events only contribute a small fraction to the events in the respective selection channels. So the contribution of $\sin^2\theta^{b}_{\text{eff}}$, that differs most from $\sin^2\theta^{\ell}_{\text{eff}}$ will only affect the combined $\sin^2 \theta^{\text{eff}}_W$ by a very low amount on the order of 10^{-5}, which is sub-dominant to the difference in processes with u- and d-quarks on the parton side.

The latest results from hadron colliders are obtained by the CDF and DØ experiments at Tevatron [24, 25, 26, 27] and the measurement by the CMS [42, 43] collaboration at the LHC. At CDF and DØ the decays of $Z \to ee$ events in $\text{p}\bar{\text{p}}$ collisions were studied, while CMS is using $Z \to \mu\mu$ decays from pp collisions. The public results of the mentioned experiments are summarised in Sec. 10.4.1 in comparison to the results of this study.

In addition the weak mixing angle can also be extracted at other scales μ away from the Z resonance. Here it has to be taken into account that the value of the effective weak mixing angle is depending on the scale. Due to loop corrections to the propagator and the vertices, $\sin^2 \theta^{\text{eff}}_W$ is showing a running behavior

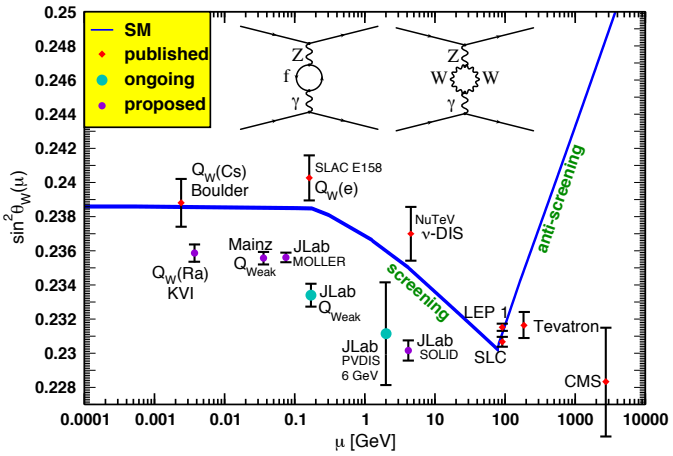

Figure 2.4.: Dependency of the weak mixing angle on the scale μ [44]. The expected running predicts a minimum at $\mu = m_W$ and shows discontinuities in the spectrum at different thresholds in the renormalisation scheme used. The size of the uncertainties in the theoretical prediction is indicated by the line width. As the measurements labeled with Tevatron and CMS are effectively also performed in the Z resonance, they were displaced horizontally for clarity. Ongoing and proposed measurements are further vertically displaced but show the prospected values of μ and the expected precision. Taken from [45].

depending on μ. In Fig. 2.4 the above mentioned results from LEP and SLD, as well as the measurements on the Z resonance by the Tevatron experiments and CMS are shown. Additionally a selection of running and upcoming experiments is included. The results at low μ are estimated from neutrino-iron scattering [46], low energy electron proton scattering (SLAC E158 [47]) and atomic-parity violation (APV [48]). At these scales the current results are not yet compatible in precision to the Z resonance measurements and are depending on the precision of different non-trivial theoretical uncertainties included. Because of this, further measurements are proposed to improve the experimental precision in the determination of the running weak mixing angle at scales lower than m_Z. For example there are experiments planned to measure the weak charge of radium nuclei or the proton. One of these is planned at the MESA facility at the Johannes Gutenberg-Universität Mainz, using low energetic electron beams scattering on proton targets at a scale of $\mu = 0.0022\,\text{GeV}^2$.

The measurement of the weak mixing angle has further relations to other physics observables. Through the virtual corrections to the propagator and vertices, more or less strong sensitivities to e.g. the masses of the top quark, the W boson and the Higgs boson are implied. When the results of the most precise individual measurements at the Z resonance and at lower scale μ are used to derive the related value of the Higgs mass, it can be shown that the measured resonance found compatible with a SM Higgs boson matches well with the world average in $\sin^2\theta_W^{\text{eff}}$ but with neither of the current high-precision results at the Z resonance. Fig. 2.5 is giving an impression of the impact of the mentioned results on the allowed mass of the Higgs-boson. The most precise channels of the LEP and SLC results, and the extractions from the APV as well as the current (SLAC E158) and future (MOLLER [49]) results in polarized Møller scattering experiments are included in this figure.

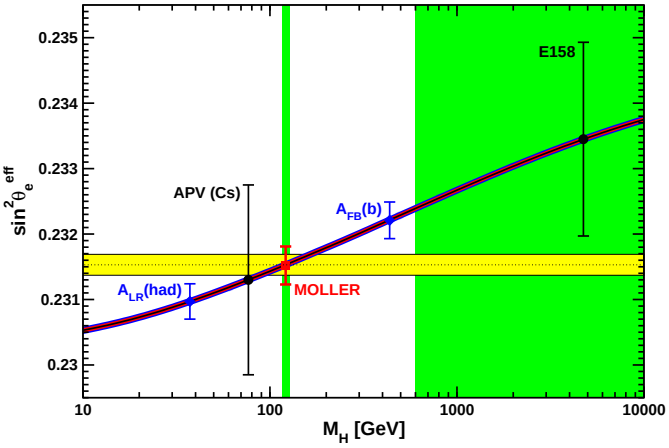

Figure 2.5.: Implied impact of most precise $\sin^2 \theta_W^{\text{eff}}$ measurements on m_H. The results shown include the most precise channels of the LEP and SLC measurements, the result from APV [48] as well as current (SLAC E158 [47]) and future (MOLLER [49]) polarized Møller scattering experiments. The yellow band denotes the current world average ot the $\sin^2 \theta_W^{\text{eff}}$ measurements and the green areas show the yet non-excluded regions for the Higgs boson mass. The prospected point for the MOLLER experiment is set to the directly observed resonance that is compatible to a SM Higgs. Its uncertainty is set to the prospected experimental uncertainty of the measurement. Taken from [45].

3. Description of the Experiment

In this section the experimental setup used in this thesis is described. This setup consists of the ATLAS-Experiment located in an underground cavern at an interaction point of the Large Hadron Collider at the CERN main site near Geneva - Switzerland. The Experiment has been taking collision data in different conditions from December 2009 until early 2013. In this study only the data taking period of the year 2011 is discussed.

In the following sections 3.1 and 3.2 the accelerator and collider as well as the experiment and its main data collection components are discussed. There the components of the ATLAS detector are introduced, including the tracking system and the calorimeter sections which are essential to this thesis. Further the basics of the muon tracking system and the structure of the trigger and read out components are introduced.

3.1. The Large Hadron Collider

The Large Hadron Collider (LHC) - located at the CERN[1] site near Geneva - Switzerland - is a particle synchrotron that is giving access to the currently highest collision energies at high interaction rates between protons or heavy ions such as lead or gold.

The collider is situated in a 27 km long ring tunnel that was built for the previous collider LEP[2] and lies between 50 m and 150 m below the surface. As displayed in Fig. 3.1 the LHC houses four main experiment in four caverns distributed around the ring: ATLAS [19], ALICE [50], CMS [20] and LHCb [51]. The ATLAS and CMS experiments are both designed as multi purpose detectors. They are located at opposite sides of the ring to run in the same collision mode. The ALICE and LHCb experiments are located in caverns closer to the CERN site and not at opposing positions with respect to the tunnel. ALICE is specialised on the measurement of heavy ion collisions where as LHCb is prominently measuring B-meson decays and is the only experiment not being built as a "4π" detector but only covering a small solid angle along the beam axis at one side of the interaction point.

The LHC magnet segments installed in the tunnel are designed to focus and bend beams of charged particles. Between the magnets, cavities housing electric fields are installed to provide particle acceleration to very high energies in the two beams. The particle beams are not filled continuously but are stored in groups of so called bunches. As achieving high beam intensities is one of the goals of the LHC, large particle packages are used. The number of particles in a bunch can not be increased when it is already filled into the beams of the LHC, so it is necessary to use dedicated accelerators to collect and accumulate the needed amount of particles and store them, to fill these big bunches into the collider. A set of dedicated pre-accelerators is used to match these criteria. This accelerator chain is also reused from other previously installed accelerators on the CERN site such as the full accelerator chain of the Super Proton

[1] **C**onseil **E**uropeénne de **R**echerche **N**ucléaire, european council for nuclear research, a center for studies in high energy physics near Geneva on both sides of the border of Switzerland and France

[2] LEP: **L**arge **E**lectron **P**ositron Collider

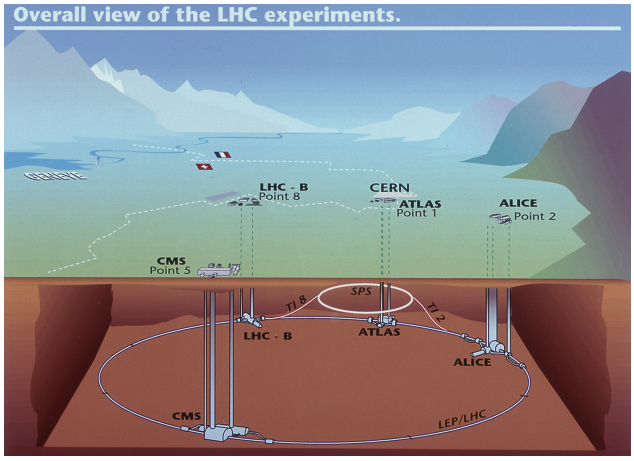

Figure 3.1.: This figure shows the locations of the four main experiments (ALICE, ATLAS, CMS and LHCb) at the LHC. The experiments are located between 50 m and 150 m underground in huge caverns that have been excavated to house the detectors. The SPS, the final link in the pre-acceleration chain, and its connection tunnels to the LHC are also shown.

Synchrotron (SPS), which is collecting and accelerating the bunches of particles up to its design capabilities to inject them as beam segments into the two LHC beam lines.

The LHC design collision rate of 40 MHz and nominal collision energies of 14 TeV have not been reached though, but it is already the most powerful machine of its kind. The nominal luminosity is designed to be of the order of $10^{34}\,\mathrm{cm}^{-2}\mathrm{s}^{-1}$. Currently an instantaneous luminosity of up to $8 \cdot 10^{33}\,\mathrm{cm}^{-2}\mathrm{s}^{-1}$ at rates of up to 20 MHz and center of mass energies of 8 TeV have been reached in the 2012 data taking period. In some machine development runs also the nominal collision rate of 40 MHz at beam energies of 4 TeV each have been studied but no collisions were recorded.

Due to the number of particles in the bunches it is expected that in nominal collision mode on average up to 25 collisions of beam particles are occurring each bunch crossing in the high intensity experiments ATLAS and CMS. The time that is needed by decay particles to pass the ATLAS detector from the interaction point outwards already covers different bunch crossings. In the 40 MHz setup, decay particles of up to four bunch crossings are expected to be simultaneously present in different parts of the detectors. Therefor very high quality criteria have to be applied, considering the timing of the read out and storage systems.

3.2. The ATLAS Experiment

The ATLAS[3] experiment is the largest of the four main experiments at the LHC. It is designed as a multi purpose detector and built with a shell-like structure of particle identification components. Including all components the detector has a length of 44 m, an outer diameter of 25 m and weighs about 7000 t. Most of the components of ATLAS are built and arranged in barrel-like central sections and disk-like end-cap sections to cover the available detection volume from the center outwards. This can be seen in Fig. 3.2. Particles that are created in the hard collisions at or close to the nominal interaction point inside the

[3] ATLAS stands for **a** **t**oroidal **L**HC **a**pparatu**s**

beam pipe and their decay products can pass the following components of the detector, if their energy and momentum is large enough:

- directly around the beam pipe the tracking system, called inner detector (ID), is used to measure the interaction with charged particles and reconstruct the tracks from the point of creation towards the detector surface. It also reconstructs the interaction vertices the tracks originate from.
- the solenoidal magnet is filling the volume of the inner detector with a constant magnetic field.
- the electromagnetic (em) calorimeters are designed to contain a large fraction of energy deposited by electrons, positrons and photons and are segmented fine enough to distinguish the shape of the energy depositions between hadrons and electromagnetic showers.
- the hadronic calorimeters are designed to measure the energy of particles leaving the em calorimeters and to contain as much of the showers as possible.
- the muon system is a tracking system on the outside of the detector. It is built outside of the calorimeters and is designed to resolve the track points of muons passing the detector from the inside out.
- additional supporting structures are brought in place to mount the previously mentioned components on and to feed the cables for voltage supply and data read out as well as the pipes delivering the cooling liquids to the components inside of ATLAS.

In the following sections the coordinate system inside ATLAS, the different sub-detectors and the trigger and data acquisition system are presented in more detail.

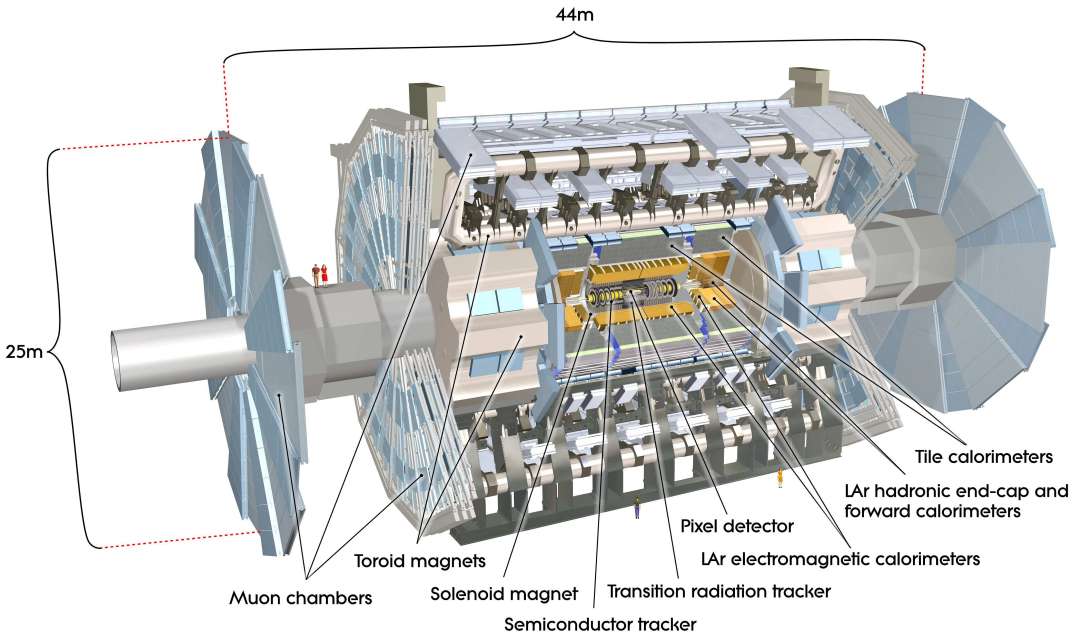

Figure 3.2.: Cut-away view of the ATLAS detector and its shell like structure [19]

3.2.1. Particles in Matter

The particles produced in the hard interactions at particle colliders have to be detected and identified alongside the measurement of their kinematic properties like energy and momentum, as well as their

position in the detector. The basic components of particle detection are given by their interaction with the matter the detectors are built of. Usually there are caverns to measure the tracks of charged particles as well as calorimetric caverns to stop the particles and measure their energy.

To distinguish different particles by their interaction with the detector components it is important to note which fundamental interaction the respective particles are taking part in: Photons, electrons and muons take part in the electromagnetic but not in the strong interaction, so the discussion of the different structures of energy loss is started with these particles. The main interaction of muons with a detector is due to the ionisation of the detector material. Because of this the muons transfer small amounts of their energy to the electron shells of the atoms they pass and separate the electrons from their nuclei. Is the respective part of the detector prepared to register such ionisation processes, a set of so called hits can be combined to construct tracks that follow the trajectory of the high energetic muons. When the respective parts of the detectors are embedded in magnetic fields to bend the trajectories of charged particles, the curvature of the trajectories can be used to determine the charges and momenta of the particles. The fact that high energetic muons are mostly behaving like minimal ionizing particles is described by the Bethe-Bloch equation [32]. It parametrizes the energy loss or stopping power of "moderately relativistic charged particles other than electrons [that] lose energy in matter primarily by ionization and atomic excitation" [32]:

$$-\frac{dE}{dx} = Kz^2\frac{Z}{A}\frac{1}{\beta^2}\left[\frac{1}{2}\ln\frac{2m_e c^2\beta^2\gamma^2 T_{\max}}{I^2} - \beta^2 - \frac{\delta(\beta\gamma)}{2}\right] \tag{3.1}$$

The Bethe-Bloch equation depends mainly on the relativistic velocity β of the particles and the atomic number of the absorber over its mass $\frac{Z}{A}$.

With a lower probability it is possible for the muons to radiate off bremsstrahlungs photons. This happens when the muons perform coulomb interaction with the nuclei of the detector matter. In rare cases it can happen that the photon from the bremsstrahlung is carrying a large fraction of the initial muon momentum. This is referred to as a catastrophic bremsstrahlung event. The radiated photons are able to ionise other nuclei nearby. When the radiated photons are high energetic enough, the photons can produce electron positron pairs and deposit an electromagnetic shower in the detector material.

The showers of photons and electrons are almost identical. The main mechanism in the propagation of an electromagnetic cascade is the combination of bremsstrahlung and electron-pair-production. Starting with an electron in the initial state, a photon is radiated off, carrying a sizable fraction of the electron momentum. The energy of the photon is high enough to produce an electron pair and the remaining electrons are introducing further bremsstrahlung. After a few cycles the electrons and photons are low energetic enough to be caught by the detector material. This way the electromagnetic shower is built up. Starting from an initial photon, the only difference with respect to the electron induced electromagnetic shower is, that the photon has to split into an electron pair first. With this two largely overlapping showers are build, which contain the energy of the photon.

If the initial photons are converted to a pair of electrons very early in their respective way though the detector in a region of low local material density, they can result in pairs of electrons that are depositing their energy in electromagnetic showers without any overlap. These electrons then have a common vertex as origin of their trajectories, that is displaced from the original vertex of the hard interaction and marks the point of the photon conversion.

The signatures of τ leptons depend due to the very short lifetime of the τs in the detector on the respective decay products. The tauons can decay in the previously discussed electrons or muons by emitting two additional neutrinos that also carry away energy. The branching ratio to electrons and muons is about 18% each which leaves about 64% of the tauons to decay into light mesons. These hadronic particles

additionally take part in the strong interaction which also influences the way hadronic signatures are showing up in the detector material.

As the strong interaction opens another degree of freedom for these particles to interact with the nuclei of the detector material the shape of the hadronic showers differs from electromagnetic energy depositions. In general, the showers of hadronic energy depositions is broader and passes further into the calorimetric caverns. This is a result of the feature that the hadrons usually do now split up in pair cascades like photons and electrons, but loose energy due to ionisation, bremsstrahlung, the decay of the constituents of the shower and capture of light particles in the detector material. These showers usually are not further built or seeded with single particles, but contain due to the nature of the strong interaction a variety of particles of different types from the beginning. These bundles of particles that originate from the same process are called jets as they are used to consist of a set of particles that carry a similar boost. Even photons and leptons can be contained in such jets. They are usually originating from mesons that are decaying within the jet to other hadrons and leptons.

3.2.2. Coordinates in ATLAS

The coordinate system in ATLAS is a modified spherical coordinate system aligned along beam axis. The Cartesian axes are aligned in a way that the x axis is pointing towards the center of the LHC ring, the y axis is pointing upwards and therefore the z axis is aligned in counter clock wise direction along the beam pipe of the collider. In the $x-y$ plane an azimuthal angle φ is defined so that its zero position is set to the positive direction of the x axis. The range φ is running in can be defined differently, either from $0-2\pi$ or from $(-\pi)-\pi$ where the range of $0-\pi$ is always part of the upper hemisphere of the detector. In this thesis the latter choice was taken. Finally the third component of this coordinate system is defined not to be the polar angle θ but a related physics observable - the pseudo rapidity η. These two quantities are related by:

$$\eta = -\ln\left(\tan\frac{\theta}{2}\right), \tag{3.2}$$

where η is for massless particles identical to the rapidity $y = \frac{1}{2}\ln\left(\frac{E+p_z}{E-p_z}\right)$ of a particle in a boosted Lorentz frame. Here E is the energy and p_z the z component of the 4-momentum of a particle.

Tracks can be measured by the ATLAS tracking system up to $|\eta| = 2.5$, muon momenta up to $|\eta| = 2.7$ and electromagnetic and hadronic energy depositions can be collected up to $|\eta| = 4.9$, respectively.

3.2.3. The Inner-Detector and solenoid magnet system

The innermost detector section of the ATLAS detector, as shown in Fig. 3.3, is the tracking system called inner detector (ID), as denoted in Sec. 3.2. It measures the interaction of charged particles with the active components of its sub-detectors and constructs tracks out of the measured space points. It is surrounded by a set of superconducting coils producing a homogeneous magnetic field of 2 T. The coils are located in a distance of about 120 cm with respect to the beam axis, close to the outer perimeter of the inner detector.

The ID is built out of three sub-detectors. In its center closest to the interaction region a three layered semi conductor detector with read out cells in a pixel pattern is located. The next layer consists of a second multi layered semi conductor detector that is built with double layers of bar-like strip cells that are tilted with respect to each other in a small stereo angle. The third and outermost component of

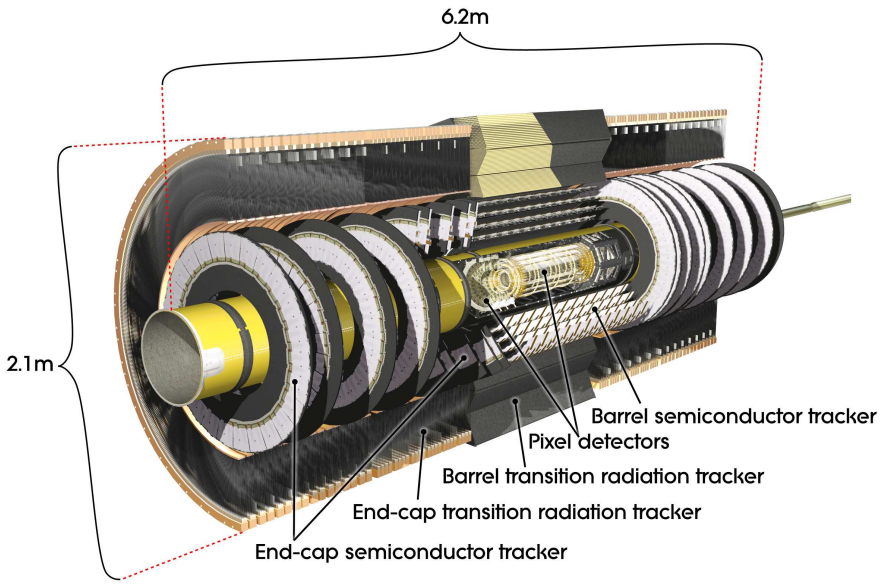

Figure 3.3.: Cut-away view of the inner detector and its components. [19]

the ID is the Transition Radiation Tracker (TRT) that is built of gas filled straw drift tubes to measure transition radiation of transiting decay products. All three sub-detectors are divided in a barrel and two end-cap sections covering the open ends of the barrel. The Pixel detector and the Semi Conductor Tracker (SCT) called second component of the ID cover a pseudo rapidity range of $|\eta| < 2.5$, the TRT covers $|\eta| < 2.0$.

The information of the ID is made available to the trigger system, but because of a strong time constraint ($\Delta t < 2.5\,\mu s$) it is currently not used at the first level. To pass the ID and reach the calorimeters particles have to have at least 0.5 GeV of transverse momentum.

The Pixel detector contains three layers of pixel modules mounted in distances between 5 and 12 cm to the beam axis in the barrel section. The length of the barrel is about 80 cm. To cover a rapidity range of up to $|\eta| < 2.5$, and to provide at least three space points per track, the end-caps on each side of the barrel are constructed of three disks each at distances of about 50 to 65 cm from the nominal interaction point. The mounted modules cover radii between 9 and 15 cm. The intrinsic position resolution is as good as $10\,\mu m \cdot 115\,\mu m$ in the $(R - \varphi)$ plane and z respectively R for the barrel and end-cap sections. The whole pixel system has about 80.4 million read out channels.

The SCT consists of a barrel section with a length of 1.5 m and is equipped with four layers of modules at radii between 30 and 51 cm from the beam axis. In the end-caps nine disks per side are installed, covering different ranges in pseudo rapidity. On these disks up to three rows of modules are mounted, depending on the available radius of the related disk. The modules mounted on the SCT consist in contrast to the pixel modules always of two semi conductor plates with strip patterns as read out cells which are tilted by a fixed angle of 40 mrad. With this setup also the SCT modules can deliver space points if both plates in a module have registered hits in cells that intersect. The intrinsic resolution is about $17\,\mu m \cdot 580\,\mu m$ in the $(R - \varphi)$ and z or R planes, respectively, for the barrel and disk modules. The SCT has about 6.3 million read out channels.

The TRT uses 4 mm narrow straw drift tubes to measure the transition radiation, particles passing the TRT are producing on the surface of the tubes. The transition radiation is emitted when charged particles are passing inhomogeneous layers of material with varying di-electric properties. The intensity of the emitted radiation is directly proportional to the Lorentz-factor $\gamma = \frac{E}{m}$ and is therefore proportional to the energy to mass ratio of a transiting particle. Because of this the signals of e.g. electrons can be distinguished from light hadrons like pions with comparable energies. The radiated photons are energetic enough to ionize the gas inside the tubes and due to the high voltage applied to the tubes surface of 1.5 kV, secondary electrons are accelerated. The avalanche process works as in a Geiger counter, yielding a signal that can be interpreted to identify the distance of the initial particle to the tubes central wire by the signal length and the integrated signal to discriminate the particle type. Typically, tracks contain about 25 - 35 hits in the TRT, depending on the number of tubes the particles are passing and the angle they transit the dielectric foils. This setup guaranties a very good resolution in φ but as the central wire of the tubes in the TRT barrel is only read out in two segments that are separated at about $\eta = 0$, the η resolution at central rapidities is poor. In the TRT end-caps the straws are aligned radially and arranged in wheels. The tube length is 37 cm. With the slightly more limited rapidity coverage of an individual tube, the position of the hits in η can in principle also be used to measure the rapidity of the passing particle, but it doesn't add much to the precision of the track fit. The TRT has about 350,000 read out channels. The intrinsic accuracy of a tube is about 130 μm in (R − φ).

3.2.4. ATLAS Calorimetry

The ATLAS calorimeter system is composed of three main sections, the electromagnetic calorimeters the hadronic calorimeters and the forward calorimeters in the end-caps. The electromagnetic sections are separated into the barrel section and the outer wheel and inner wheel of the end-cap section. The central structure of the electromagnetic calorimeters is called EM-Barrel. The components installed at the front face of the end-cap calorimeter are called ElectroMagnetic End-cap Calorimeter (EMEC) outer-wheel and inner-wheel. These EM calorimeters cover ranges in the pseudo rapidity $|\eta|$ up to 1.475, 2.5 and 3.2, respectively. The hadronic calorimeters consist of the barrel calorimeters, the extended barrel calorimeters, all built in a tile architecture, but covering different ranges in the rapidity and the Hadronic End-cap Calorimeters (HEC) using different geometry and materials as the barrel sections. These hadronic calorimeters cover ranges in the pseudo rapidity $|\eta|$ up to 1.0, 1.7 and 3.2, respectively. The Forward Calorimeters (FCal), that are not separated between specialized electromagnetic and hadronic read out compartments, are covering the outermost range in pseudo rapidity up to $|\eta| = 4.9$.

All calorimeters are built as sampling calorimeters with alternating active and passive materials, but in slightly different ways. The active material in the EM calorimeters, the HEC and the FCal components is liquid Argon (LAr). As passive material copper, tungsten and lead are used. The signal read out is achieved by measuring the ionisating current in cells inserted in the active material. The tile calorimeters use iron as passive and scintillating plastic tiles as active materials and are connected through optical fibers to Photo Multiplier Tubes (PMT). The position and orientation of the above listed components of the ATLAS calorimeter system are shown in Fig. 3.4.

3.2.4.1. ElectroMagnetic Calorimeters

The EM Calorimeters in ATLAS are built in sampling architecture with LAr as detection medium. To keep the argon in liquid phase, the calorimeters have to be cooled down to about 80 K and housed in

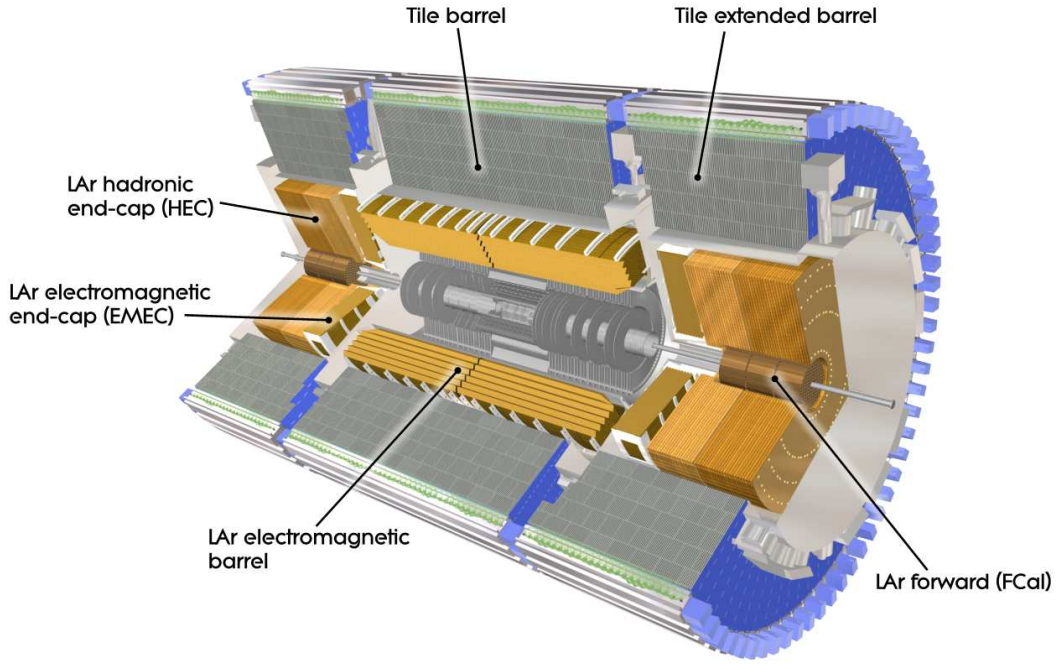

Figure 3.4.: Cut-away view of the ATLAS calorimeters and their components. [19]

cryostats. Three cryostats are installed to provide a cooled down environment for the barrel and the two end-cap EM calorimeters. In the barrel-cryostat also the superconducting coils of the solenoid magnet system are installed and kept at operation temperature. As cooling medium liquid nitrogen is used that has a lower boiling point as the argon used in the calorimeters.

The layers of passive and active materials of the EM calorimeters are ordered in an accordion geometry. In the barrel the wave structure is aligned parallel to the beam axis, so that particles originating from the interaction point have to pass through the layers of active and passive material in a large angle. This geometry eases the structuring of the sampling, as for growing radii in the accordion the amplitude and angle of the folded layers can be adjusted to fill out the calorimeter volume without introducing artificial gaps. Additionally the thickness of active and passive sampling layers can arranged to stay constant. In the end-caps the accordion geometry is aligned perpendicular to the beam axis and the layers of active and passive material are ordered in slices going from the beam axis outwards. In the EMEC wheels the individual absorber layers are installed projective towards the beam pipe. These absorbers are shaped with increasing folding angle and amplitude for larger radii. This setup is shown in Fig. 3.5

As mentioned before, the LAr layer in the accordion composition of active and passive material has a constant size. It is kept at 2.1 mm distance between neighbouring absorber plates by honeycomb spacers. On both sides of the gaps conductive copper layers are inserted and insulated from the absorbers by polyamide sheets. These layers are set to high voltage (HV) of 1.0 kV to 2.5 kV in different sections along η. Inside a section of constant HV this introduces a constant drift potential for the energy measurement. Between them the read out electrodes are held in place by the already mentioned spacers. These read out electrons are segmented in η and R to model the calorimeter cells. In Fig. 3.6 the electrodes layer for EM-barrel and end-caps are shown. Along φ the different read out signals are connected inside the signal summing boards to achieve the required cell segmentation. Typically the segmentation in R shows

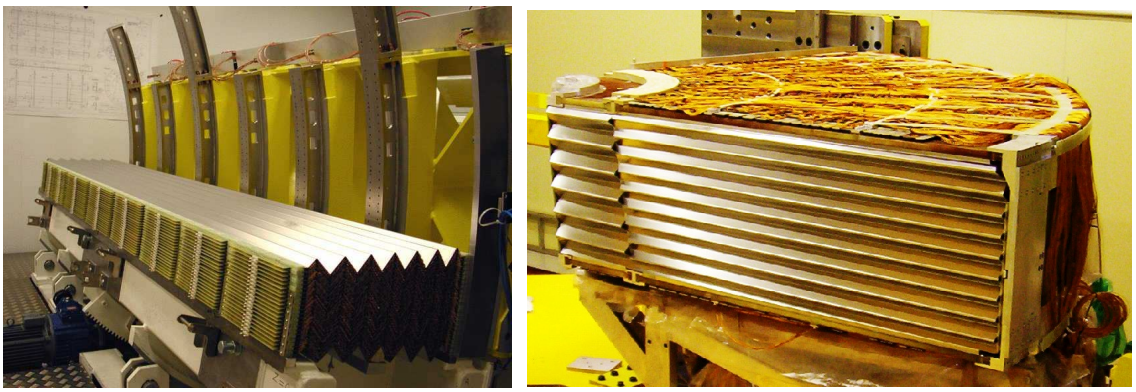

(a) (b)

Figure 3.5.: Sections of the EM barrel a) and EMEC b) modules are shown while assembly. Note the different amplitudes and folding angles in the absorbers at different radii. In b) also the changed geometry at about $|\eta| \approx 2.5$. [19]

three samplings. Only in the EMEC inner-wheel above $|\eta| = 2.5$ and in the transition regions between the barrel and the end-caps, the fist sampling is combined with the second. The first sampling is meant to discriminate isolated energy depositions of single photons from pion decays like $\pi^0 \to \gamma\gamma$. This is one dominating background in e.g. the search for decays of $H \to \gamma\gamma$. Therefore the first calorimeter layer is segmented in narrow stripes in η that are extended in φ. In the second sampling the electromagnetic showers deposit their largest amount of energy. This central sampling is segmented symmetrically in η and φ. The typical radiation length after the second sampling is kept constant along η, so that the third sampling can be used to measure the energy loss and longitudinal leakage into the hadronic calorimeter sections.

The EM-Barrel In the barrel-EM-calorimeter a range in pseudo rapidity of $|\eta| < 1.475$ is covered. The granularity of the barrel calorimeter in η and φ has an almost constant pattern that only differs at the high $|\eta|$ edges in the transition region of barrel and end-caps. The granularity of the EM-Barrel calorimeter is summarized in Tab. 3.1.

The absorbers in the barrel are built of lead plates covered with 0.2 mm thin stainless-steel sheets. The thickness of the composite absorbers are 1.53 mm for $|\eta| < 0.8$ and 1.13 mm for $|\eta| > 0.8$. To keep the overall variation in the amount of material in front of the particles passing the calorimeter small along η, this change of geometry is introduced. The typical thickness of the detector after the EM calorimeters varies along η from 25 to 40 in units of the radiation length X_0. The thickness after the second sampling is kept almost constant across η at about 25 X_0. The high voltage potential between the electrodes is held at 2 kV.

Even before the first sampling of the EM-barrel calorimeter a layer of modules of 11 mm thick LAr cells are installed as a presampler system. This presampler is installed on the outside of the solenoid magnets in the barrel cryostat and is used to estimate the energy of particles before entering the sampling calorimeters. The modules of this subsystem have a size of 0.2×0.2 in $\eta \times \varphi$ and cover a range in pseudo rapidity up to $|\eta| = 1.52$. Therefore at the ends of the presampler the modules only cover 0.12×0.2 in $\eta \times \varphi$. The granularity in the cells of the presampler is 0.025×0.1 in $\eta \times \varphi$ along the full coverage. The high voltage potential between the electrodes is also set to 2 kV.

	Barrel		End-Cap	
	Number of layers and $\|\eta\|$ coverage			
Presampler	1	$\|\eta\| < 1.52$	1	$1.5 < \|\eta\| < 1.8$
Calorimeter	3	$\|\eta\| < 1.35$	2	$1.375 < \|\eta\| < 1.5$
	2	$1.35 < \|\eta\| < 1.475$	3	$1.5 < \|\eta\| < 2.5$
			2	$2.5 < \|\eta\| < 3.2$
	Granularity versus $\|\eta\|$ $\Delta\eta \times \Delta\phi$			
Presampler	0.025×0.1	$\|\eta\| < 1.52$	0.025×0.1	$1.5 < \|\eta\| < 1.8$
Calorimeter	$0.025/8 \times 0.1$	$\|\eta\| < 1.40$	0.050×0.1	$1.375 < \|\eta\| < 1.425$
1st layer	0.025×0.025	$1.40 < \|\eta\| < 1.475$	0.025×0.1	$1.425 < \|\eta\| < 1.5$
			$0.025/8 \times 0.1$	$1.5 < \|\eta\| < 1.8$
			$0.025/6 \times 0.1$	$1.8 < \|\eta\| < 2.0$
			$0.025/4 \times 0.1$	$2.0 < \|\eta\| < 2.4$
			0.025×0.1	$2.4 < \|\eta\| < 2.5$
Calorimeter	0.025×0.025	$\|\eta\| < 1.40$	0.050×0.025	$1.375 < \|\eta\| < 1.425$
2nd layer	0.075×0.025	$1.40 < \|\eta\| < 1.475$	0.025×0.025	$1.425 < \|\eta\| < 2.5$
			0.1×0.1	$2.5 < \|\eta\| < 3.2$
Calorimeter	0.050×0.025	$\|\eta\| < 1.35$	0.050×0.025	$1.5 < \|\eta\| < 2.5$
3rd layer			0.1×0.1	$2.5 < \|\eta\| < 3.2$

Table 3.1.: Granularity and layer structure of the ATLAS EM calorimeter. [19]

	(Extended-) Barrel		End-Cap			
	hadronic calorimeter				Forward calorimeter	
	Number of layers and $\|\eta\|$ coverage					
Calorimeter	3	$\|\eta\| < 1.0$	4	$1.5 < \|\eta\| < 3.2$	3	$3.10 < \|\eta\| < 4.90$
	3	$0.8 < \|\eta\| < 1.7$				
	Granularity versus $\|\eta\|$					
	$\Delta\eta \times \Delta\phi$				$\Delta x \times \Delta y$ (cm)	
Calorimeter	0.1×0.1	$\|\eta\| < 1.0$	0.1×0.1	$1.5 < \|\eta\| < 2.5$	~four times finer	$3.10 < \|\eta\| < 3.15$
1st layer	0.1×0.1	$0.8 < \|\eta\| < 1.7$	0.2×0.2	$2.5 < \|\eta\| < 3.2$	3.0×2.6	$3.15 < \|\eta\| < 4.30$
					~four times finer	$4.30 < \|\eta\| < 4.83$
Calorimeter	0.1×0.1	$\|\eta\| < 1.0$	0.1×0.1	$1.5 < \|\eta\| < 2.5$	~four times finer	$3.20 < \|\eta\| < 3.24$
2nd layer	0.1×0.1	$0.8 < \|\eta\| < 1.7$	0.2×0.2	$2.5 < \|\eta\| < 3.2$	3.3×4.2	$3.24 < \|\eta\| < 4.50$
					~four times finer	$4.50 < \|\eta\| < 4.81$
Calorimeter	0.2×0.2	$\|\eta\| < 1.0$	0.1×0.1	$1.5 < \|\eta\| < 2.5$	~four times finer	$3.29 < \|\eta\| < 3.32$
3rd layer	0.2×0.2	$0.8 < \|\eta\| < 1.7$	0.2×0.2	$2.5 < \|\eta\| < 3.2$	5.4×4.7	$3.32 < \|\eta\| < 4.60$
					~four times finer	$4.60 < \|\eta\| < 4.75$
Calorimeter			0.1×0.1	$1.5 < \|\eta\| < 2.5$		
4th layer			0.2×0.2	$2.5 < \|\eta\| < 3.2$		

Table 3.2.: Granularity and layer structure of the ATLAS hadronic and forward calorimeter. [19]

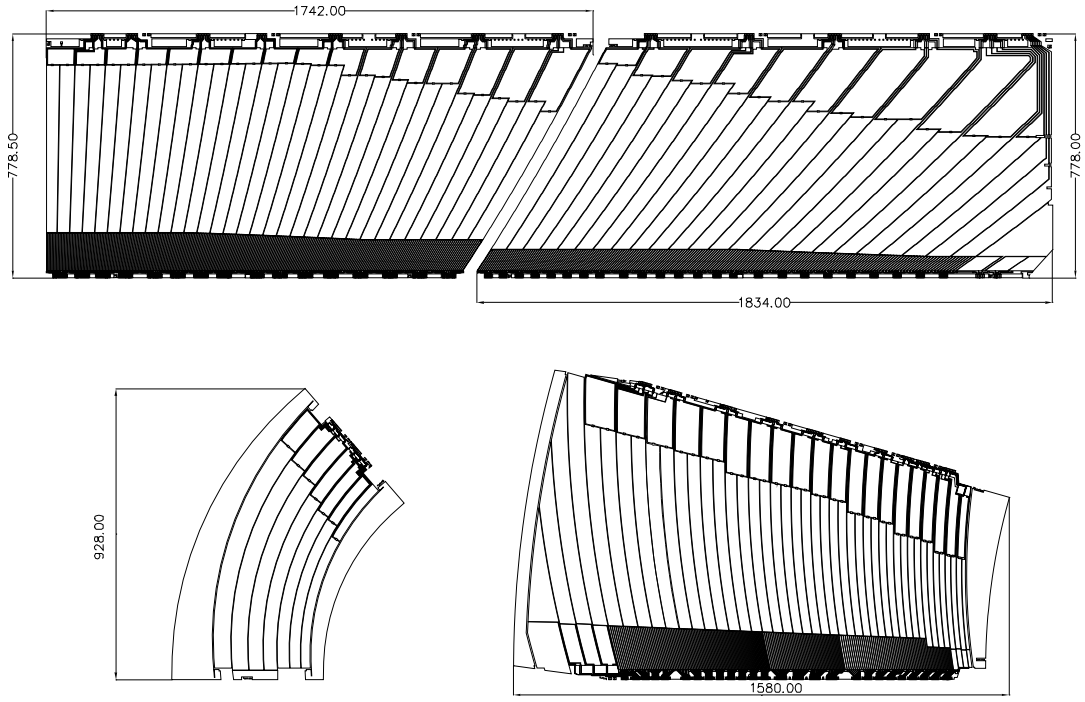

Figure 3.6.: This figure shows the layout of the read out electrodes for the four different EM calorimeter components. In the top row the electrodes of the two barrel absorber configurations are shown, left for the range $0 < |\eta| < 0.8$ for the slightly thicker absorber and right for the range $0.8 < |\eta| < 1.475$ for the thinner absorber setup. In the bottom row the read out layers of the EMEC inner (left) and outer (right) wheels are shown. The granularity and the segmentation in depth of two and three samplings, respectively for different η positions, is also visible. All figures are on the same scale and show the electrodes before folding into the accordion structure. [19]

The EM-End-Cap Outer-wheel In the EMEC outer-wheel the sampling design is very similar to the barrel section. Except for the edges close to the transition regions there are three samplings installed, also providing a fine strip layer in the first, the bulk energy measurement in the second and leakage correction in the third sampling. The coverage of the outer-wheels of the EMEC ranges from 1.375 to about 2.5 in $|\eta|$. Also close to the EMEC wheels there are presampler modules installed, covering $1.5 < |\eta| < 1.8$ with a granularity of $0.025\times \sim 0.1$ in $\eta \times \varphi$ which is the same as in the barrel. In the EMEC the thickness of the lead-stainless-steel absorbers is increased to 1.7 mm. The granularity of the second and third sampling is the same as in the barrel. As the size of cells in the first sampling along the disk radius R is decreasing for growing values of $|\eta|$, at certain points the cells get to narrow and are reordered. The details of the granularity are listed in Tab. 3.1. Additional to the varying segmentation in the first sampling also the HV in the EMEC is adapted and decreased for smaller radii and larger values of $|\eta|$. This is necessary as the LAr gap varies along R and $|\eta|$, respectively from 2.8 mm to only 0.9 mm between read out and HV electrodes. This is done to keep the average drift time in the LAr cells about constant.

The EM-End-Cap Inner-wheel The EMEC inner-wheel covers a rapidity range of $2.5 < |\eta| < 3.2$ and is integrated with the EMEC outer-wheel into a single structure. A picture of a slice of the whole EMEC is shown in Fig. 3.5(b). The construction and alignment is very similar to the EMEC outer-wheel, only

the details of the sampling, the granularity, the used absorber thickness and the high voltage differ in the inner-wheel. To build this component as radiation-hard as possible, the absorber thickness is increased further to 2.2 mm and the first fine segmented strip layer is omitted. This means that the signals of the cells inside the inner-wheel do not have to be read out at the front of the calorimeter anymore on the one hand, but it restricts the sampling to two layers only on the other. Sampling 2 again collects the bulk of energy deposited in the calorimeter cells and sampling 3 corrects for leakage and longitudinal losses. The granularity is now reduced to cells of 0.1×0.1 in $\eta \times \varphi$ for both samplings. The thickness of the material behind the first sampling of the inner-wheel is kept to corresponds to the values of about $25\,X_0$, as it was designed to be in the more central EM calorimeter sections. Similar to the outer-wheel, the LAr gap varies for different radii from 3.1 mm to 1.8 mm. Therefore the HV setup is also adjusted and two ranges are defined.

As already discussed in Sec. 3.2.3 the tracking system only covers a pseudo rapidity range below $|\eta| = 2.5$, so the inner-wheel is not having a complementary detector component for particle reconstruction and identification. This has implications on the particle identification and energy calibration as discussed in Sec. 5.3 and 7.

3.2.4.2. Hadronic Calorimeters

The hadronic calorimeters are separated in six sections, the barrel and extended-barrel tile calorimeters and the Hadronic End-Cap calorimeter (HEC) on each side of the detector.

The Tile Barrel and Tile Extended-Barrel are built from alternating stainless-steel and scintillating plastic tiles, which are oriented perpendicular to the beam axis. The sections are read out in three layers, as it is done for the EM barrel and end-cap calorimeters, but the signal is fed by optical fibers to PMTs that are located on the outer perimeter of the tile barrel and extended-barrel. These Calorimeters have a radial depth of about $7.4\,\lambda$ (hadronic interaction length) at low rapidities and up to about $10\,\lambda$ at the high end. The granularity is about 0.1×0.1 for the first two samplings and 0.2×0.1 for the third sampling, respectively in $\eta \times \varphi$. The coverage of these calorimeters is about $|\eta| < 1.0$ for the tile barrel and $0.8 < |\eta| < 1.7$ for the tile extended-barrel calorimeters.

The Hadronic End-Cap The Hadronic End-Cap calorimeter (HEC) are using copper and LAr as passive and active materials and are located in the end-cap cryostats as the HEC covers a similar range in $|\eta|$ as the EMEC. The modules are built in two wheels per end-cap and are segmented in four sections in depth each. The wheels are constructed in 32 wedge shaped segments that build a disk of about 4 m in diameter. These disks are installed directly behind the EMEC wheels. The first HEC wheel consists in depth of 24 copper absorber plates that are 25 mm thick and an additional front plate of half that thickness. The rear wheel is stacked of 16 copper absorber plates of 50 mm depth and an additional front plate also of half the depth similar to the front wheel. The gaps between the copper plates are 8.5 mm wide and contain three electrode layers each. The central electrode is used to read out the signal whereas the outer electrodes are positioned at half the distance between the read out layer and the copper plate. The distances are kept constant by insulating honeycomb spacer sheets. The HEC modules are held together by seven stainless-steel rods per module that also hold spacers in place to keep the electrodes and copper absorbers in place. The HEC covers a rapidity range of $1.5 < |\eta| < 3.2$ and has a cell granularity of 0.1×0.1 below $|\eta| = 2.5$ and 0.2×0.2 for $|\eta| > 2.5$ in $\eta \times \varphi$ respectively. The cells are combined semi-projectively to the nominal beam interaction region. This can be seen in Fig. 3.7. The typical amount of material particles "see", when traveling through the detector and passing the HEC, is about $10 - 12\lambda$.

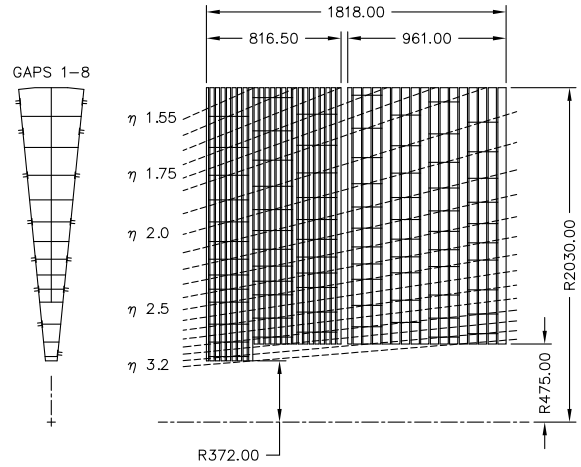

Figure 3.7.: Granularity and read out cell alignment in a wedge of the HEC. [19]

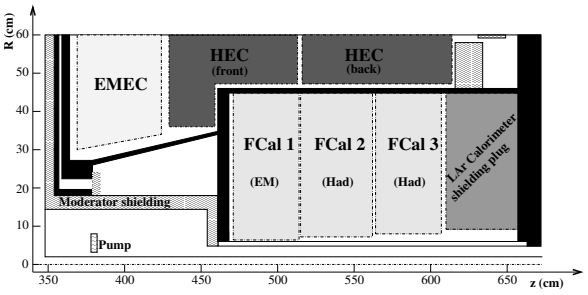

Figure 3.8.: Positioning of the end-cap and forward calorimeters. [19]

This is enough to maximize the amount of energy which jets from proton-proton collisions at a center of mass energy of 14 TeV deposit inside the calorimeters.

3.2.4.3. Forward Calorimeters

The Forward Calorimeters (FCal) are also using LAr as active medium and are segmented in three components in depth. The main passive material is made of copper or tungsten, depending on the segment. As this detector is located very close to the beam axis it has to be built as radiation-hard, heat resistive and robust as possible. Therefore, the intrinsic granularity has to be made coarser and more stable as in the more central calorimeters. The design of the read out cells in all segments is based on rods surrounded by a thin layer of LAr. These rods are ordered in hexagonal matrices and housed in copper or tungsten to let the transiting particles shower up. This setup is shown in Fig. 3.9 for read out electrodes of FCal1 close to the beam axis. To further prevent parts of the showers from leaking outside of the FCal a shielding plug made of a copper-alloy is installed after FCal3. This prevents remaining shower decay products from reaching upstream detector parts like the end-caps of the muon system.

To build a well defined LAr gap around the signal rod, the outer wall of the active cell is a copper tube with the length of the rod. The gap between rod and tube is held constant by a fiber twisted around the rod. In the first segment FCal1 the absorber matrix is drilled out of copper plates and the signal read out rods are inserted into this matrix. In the second and third segment FCal2 and 3 the supporting absorber matrix is constructed of copper front and end plates that hold the signal rods in place while the gaps between the rods are filled up by tungsten slugs. This setup is shown in Fig. 3.10. In FCal2 and FCal3 the rods are made of tungsten as well. This lets the FCal be very radiation-hard on the one hand and act very homogeneously on the shower development on the other. As summarised in Tab. 3.3 the LAr gap varies from 0.27 mm to 0.51 mm in the three modules. This introduces drift times for the signal charges, that are collected in the LAr volumes, of about 60 ns, because the HV is also adapted to range from 250 V to 500 V in the respective modules.

In the FCal the read out electrodes are not used as individual signal lines, but are ganged together in groups of four, six and nine for the modules FCal1, FCal2 and FCal3 respectively, to build signal lines.

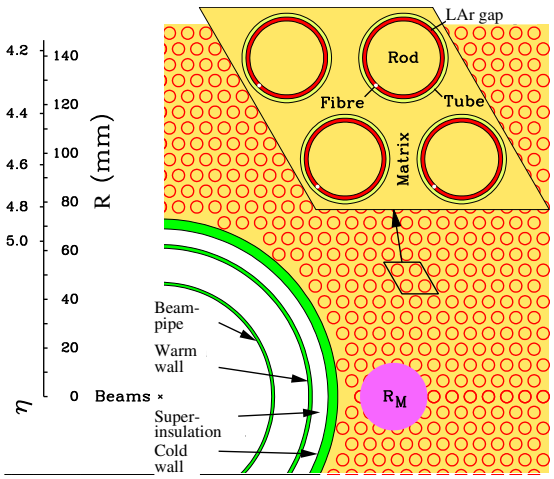

Figure 3.9.: Electrode structure of FCal1 with the matrix of copper plates and the copper tubes and rods with the LAr gap for the electrodes. The Moliére radius, R_M, is represented by the solid disk. [19]

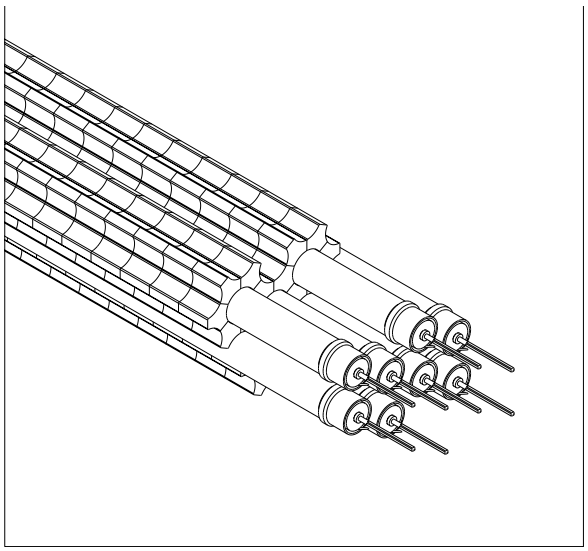

Figure 3.10.: View of the FCal hadronic module absorber matrix, including a set of tungsten rods and copper tubes surrounded by 1 cm long tungsten slugs. [19]

	FCal1	FCal2	FCal3
Function	electromagnetic	hadronic	hadronic
Mass of module (kg)	2119	3826	3695
Main absorber material	copper	tungsten	tungsten
LAr gap width (mm)	0.269	0.376	0.508
High voltage [V]	200	375	500
Radiation length (X_0)	27.6	91.3	89.2
Absorption length (λ)	2.66	3.68	3.60
Number of electrodes	12260	10200	8224
Number of read out channels	1008	500	254

Table 3.3.: Table of parameters for the three FCal modules. [19]

Depending on the position at the inner or outer edges or in the bulk of the FCal modules, these signal lines are then grouped together again by the signal summing boards that are installed on the back of the HEC. This procedure explains the difference in the number of electrodes and read out channels that can be looked up in Tab. 3.3. The granularity in $\eta \times \varphi$ is not as well defined as in the other calorimeters as the structure of the read out channels is not aligned along η and φ. It can be estimated to be approximately 0.2×0.2 in $\eta \times \varphi$ but varies along η and in the modules FCal1-3. The actual granularity in the FCal is listed in Tab. 3.2.

3.2.5. Muon Detectors and toroid magnet system

The muon system builds the outer shell of the ATLAS detector and fills the largest volume in the experiment. It consists of different detector components installed between the air coils of the large toroid magnet systems. The toroid system is built of a set eight barrel toroid coils and two end-cap toroids that are also built of eight coils each. The field strength reaches up to 4 T in the coils but varies due to

the geometry between 0.2 T and 2.5 T in the barrel and 0.2 T and 3.5 T in the region dominated by the end-cap toroids. The effective field strength to bend the muons passing this region is in the order of 0.5 T to 1.0 T.

The detector modules in the muon system contain a set of precision chambers, the Muon Drift Tubes (MDT) that cover a rapidity range of $|\eta| < 2.7$ and the Cathode Strip Chambers (CSC) that cover the range of $2.0 < |\eta| < 2.7$. The MDT modules are located on the outer perimeter of the muon system and can measure particle rates up to 200 Hz/cm^2. The CSC modules are able to cope with higher interaction rates and can therefore be installed closer to the beam pipe. The other two muon systems that are used for momentum determination as well as for the trigger system are called Resistive Plate Chambers (RPC) and Thin Gap Chambers (TGC) and have a relatively fast response. The RPC modules are located in the barrel whereas the TGC modules are installed in the end-cap sections and cover in combination a range of $|\eta| < 2.4$ in rapidity.

3.2.6. Trigger and DAQ

The ATLAS trigger system is built up in a three-step scheme. It consists of a first fast layer that is implemented in hardware boards and two decision taking layers that analyse different levels of detail of the remaining events on a dedicated software farm. These stages are called “Level 1”, “Level 2” and “Event Filter”. In design conditions about 23 simultaneous interactions are on average produced per crossing of proton-proton bunches in the ATLAS interaction region. Multiplying this number with the nominal bunch-crossing-rate of 40 MHz gives an average interaction rate of about 1 GHz. The trigger system has to be able to reduce the event rate from 40 MHz to below 300 Hz. This is the rate that corresponds to the typical amount of information per event that can be written to storage tapes. The patterns upon which the trigger levels save or discard events and event topologies have to be designed to reduce the rate of very frequent events in order to reserve bandwidth for events that occur a lot less often.

The Level 1 trigger stage (L1) is built of two independent systems, the L1Calo named calorimeter based trigger and the L1Mu called trigger, based on the previously introduced information of the fast components in the muon system. These components reduce the event rate by about a factor 500 to ≤ 75 kHz where each decision has to be taken in at most 2.5 µs. Because of this time constraint the L1Calo trigger uses the calorimeter information in a reduced granularity. Two different processing modules are producing dedicated inputs to define trigger decisions for em-like and jet-like energy depositions. These components are called the Cluster Processor Module (CPM) and the Jet Energy sum Module (JEM). A cluster is defined as an energy deposition in the EM sections of the calorimeter system in a rapidity range below $|\eta| = 2.5$, which is what the CPM is using as input. The JEM is looking for coarser energy depositions in all calorimeter regions up to $|\eta| = 3.2$ and measures the total energy sum and the missing transverse energy in the calorimeter up to $|\eta| = 4.9$ including all calorimeter components. Because of the low granularity and the fact that the objects handled by the trigger processors cover all calorimeter layers at the same time the objects at L1Calo are called trigger towers. When an event is accepted by L1 a so called region-of-interest (ROI) is defined and passed on to the second trigger stage L2. This ROI is checked by L2 in full detector granularity.

The two software based trigger stages L2 and Event Filter (EF) are summarized as High Level Triggers (HLT) and have information of all detector components available. Additional to the calorimeter and muon information the HLT also have preliminary tracking information to be able to define objects like electron and photon or muon candidates and perform reconstruction algorithms that are close to the ones used in the offline selection at the post production stage. The L2 trigger is restricted to only process these

information in the ROIs the L1 triggers have found whereas the EF builds the full event and is therefore able to also discriminate events by more complex event topologies containing different multiplicities and thresholds of different candidate objects. This variety includes the use of levels of identification selections that are very close to the ones produced at the full data reconstruction algorithms in the offline data processing stream.

Some trigger signatures are estimated to be contributing too high load to be directly passed to the next trigger level or to tape after the EF. To cope with the limited bandwidth of the trigger system and the limited data processing rates at the different stages of the trigger system, so called prescales are introduced. These prescales are set up to reduce the number of selected events corresponding to a trigger by an adaptable factor. This means that for very frequent signatures like loosely identified low energetic electrons for example only every n-th event is firing a corresponding trigger accept.

All Information of an event has to be held in storage buffers while the trigger decisions are pending. Here the dimension of the buffering system is setting constraints on the time the triggers are allowed to use for their calculations.

The buffering system of the L1 triggers has a fixed size to store the detector information of a certain number of interactions. These buffers are overwritten after 2.5 µs, which sets the limit for the L1Accept signal to be fired. After the L1Accept, the event information is moved to the HLT computing farm for further processing, on which both HLT systems are run. The event information can be written to the data storage system, after a positive EF trigger decision is taken.

When the event is finally on tape, the raw detector signals can be accessed by the resources of the event-post-processing. A full physics object reconstruction, as well as preliminary calibrations are performed firstly on randomly selected events in a so called “express stream”. On these events data quality criteria are checked and the final calibrations are derived. These calibrations can be applied on the full data set to perform the reconstruction of the physics object in the events. The calibrated data sets are stored in file formats of varying level of detail. Some of them include almost all information of the analogue read out of different detector components and are meant for detailed calibration and performance studies. To save space on the large storage systems, these files are only kept for a few weeks. The broad amount of the stored samples is only containing different sets of derived physics objects, as well as data quality conditions. The third level of the derived physics data sets, the so called D3PDs, are the basis of the studies described in this thesis.

4. Event samples from data and Monte Carlo simulation

In this chapter the data event samples as well as the used Monte Carlo sets are introduced. Sec. 4.1 introduces the conditions as well as some important features of the periods in 2011 data taking. The discussion of the simulation setup used in ATLAS is covered in Sec. 4.2. Here some details of the basic concepts of Monte Carlo event generation are introduced and exemplary implementations in commonly used simulation programs are discussed. In Sec. 4.3 the Monte Carlo samples used in this thesis are introduced in more detail.

4.1. Events from data

The sample of data events, further only referred to as data, is taken with the ATLAS detector in the data recording setup used in the 2011 proton-proton run. The proton beams in the LHC were accelerated up to an energy per proton of 3.5 TeV to generate collisions at a center of mass energy of $\sqrt{s} = 7$ TeV. The beams had a distance in collision time of 50 ns. They were substructured in long chains of packages of protons, the so called bunches, which were grouped in bunch trains. The integrated luminosity delivered to the experiment exceeded 5.8 fb^{-1}. About 5.25 fb^{-1} of integrate luminosity got recorded by ATLAS. The data taking was more or less continuous, but as the LHC and the experiments are unique prototypes of their kind, there were several shorter breaks used for machine development and control measurements of the accelerator properties. Together with the understanding of the machine, the instantaneous luminosity was raised from up to $2.1 \cdot 10^{-32}\text{cm}^{-2}\text{s}^{-1}$, as achieved in the 2010 data taking period, to up to $3.7 \cdot 10^{-33}\text{cm}^{-2}\text{s}^{-1}$. The beams were provided by the collider in "fills", which were used by ATLAS to record data in "runs" of mostly continuous machine conditions. These runs consist of "lumi-blocks", which are short intervals of about two minutes in recording time. The data taking runs were on the larger scale grouped to periods that correspond to similar conditions. These periods range from A to M in the 2011 data taking. The periods A and C were not meant for the typical pp analyses. Period A was set up without nominal magnetic fields for alignment measurements and period C had a center-of-mass energy of 2.76 TeV, which corresponds to the energy per nucleon achieved in the *Pb-Pb* collisions, recorded at the end of the 2010 data taking. The periods B and D to M were set up for pp analyses at $\sqrt{s} = 7$ TeV for the bulk of the physics and performance analyses. This is also the range of recorded events, the analyses and studies referred to in this thesis are based on.

The above mentioned periods differ due to the rising instantaneous luminosity, but also issues and repairs of different detector components characterize them. The mentioned repairs refer to the exchange of the front-end electronic boards (FEB), that had failures during the periods E through H and were replaced where necessary in the break between period H and I. The amount of data recorded before the incident only comprises less than 4% of all events recorded in 2011. The amount of data, in which this issue was present, corresponds to about 20%. The region that is affected the most is located in one half-barrel at about $0 < \eta \lesssim 1.45$ corresponding to one slice in the read out in ϕ at about $-0.8 \lesssim \phi \lesssim -0.6$. Here 4 FEBs were malfunctioning, that are responsible for the signal handling of the second layer of the EM

periods	fraction of data	fraction in simulation	conditions of FEB	trigger menu
B-D	3.7%	3.3%	All FEB good	v2
E-H	20.2%	17.8%	6 FEB dead (4 × layer 2, 2 × layer 3)	v2
I-K	25.0%	24.2%	2 FEB dead (2 × layer 3)	v2
L-M	51.1%	54.4%	2 FEB dead (2 × layer 3)	v3

Table 4.1.: This table lists the data taking blocks that and their fractions in the default GRL on data as well as the fraction in the simulation samples these block correspond to. Additionally the details about the FEB and trigger menu conditions are listed.

calorimeter. These boards were replaced in the technical stop between period H and I. Further there were two FEBs handling the signals for the third EM calorimeter layer that were affected: as these boards were not classified to be a big problem for physics analyses, the faulty pieces of hardware were not replaced before the end of the 2011 data taking.

The amount of data this analysis is using was filtered to contain events only if at least one trigger using information on electrons or photons was fired. This is the "egamma stream", in which the amount of pure multijet events is already reduced. It is named after the eGamma Performance Group that defines and controls the properties and performance of electrons and photons in the experiment. Next to the egamma stream there are also streams for muon triggers and jet- and missing E_{T} triggers available. The electron definitions and identification requirements were adapted in the transition from period K to L to cope with the increasing pile-up conditions. The available triggers are listed in trigger menus. These menus for the respective periods before and after this transition are named v2 and v3. This is mentioned in Tab. 4.1, together with the amounts of data and MC, collected in the various period blocks, and the respective conditions of the FEBs.

Based on these preselections on fundamental data taking, stability conditions were collected and stored in a dedicated ATLAS data base. These conditions contain the status of e.g. high voltage supplies, beam pick-up monitors or other quality conditions in e.g. the tracking system. The granularity the information is stored in is based on the lumi-blocks introduced earlier in this section. For different needs in the individual analyses sets of condition patterns can be configured to define an event preselection based on the information stored in the data base. The results of these configurations are stored in so called "Good-Run-Lists" (GRL) in which a list of lumi-blocks for each run that fulfil the chosen requirements are listed. The GRL used in this thesis is defined by egamma to be usable for analyses using central and forward electrons. As there are further requirements introduced that reduce the amount of data usable for the analyses, the luminosity that is effectively used is reduced to 4.84 fb^{-1}.

4.2. Simulation

To describe the distribution of measurable quantities in high energy physics experiments the recorded data is usually compared to the simulation of all known contributing processes constructed by event generators. Such simulated samples in general consist of three production steps. First there is the event generation step, where various processes are generated on the basis of theoretical calculations. The random element in the event generation is provided by pseudo random seeded algorithms. Because of this feature of random generation, the generators and the samples, that are produced, are usually referred to as Monte Carlo (MC). The event generation consists of the production of the hard interaction process and the corrections to this event by including radiation effects. Important radiation effects in

any process are the final state radiation (FSR) effects. In the initial collisions at hadron-, or parton-colliders, such as the LHC, the initial state radiation (ISR) has to be taken into account as well. The ISR processes dominating at the LHC are radiations of partons and the formation of jets, as introduced in Sec. 3.2.1. To accurately model these processes, production diagrams of higher order with respect to the strong coupling α_s have to be considered by the event generator. These partons are forming jets, that are decaying in the detector in addition to the hard process. The hadron remnants, that are remaining from the initial protons, are emitted in small angles to the accelerator beams. These corrections due to the ISR emissions do not only affect the partons from the hadron remnants, but also interact with the partons in the hard scattering. Due to the fact that the partons introduced in the ISR cascades do not only carry longitudinal momentum but give rise to transverse boosts of the hard process, the p_T scale of the hard interaction is determined and adjusted by the precision of calculating the ISR. In the FSR also strong interactions take place, but since this analysis concentrates on electron final states, the FSR is dominated by electromagnetic and weak interactions to the final state particles. Especially the higher order corrections due to QED radiative effects to the electrons and the properties of the photons in the FSR are to be tuned.

In many analyses, LO multi purpose MC generators like PYTHIA [52] or HERWIG [53] are used to build the hard process. They can also be used to model the showering of jets in ISR and FSR. For dedicated samples of simulated events, the results from these generators can be interfaced with other Monte Carlo programs. These generators are specialised either on the electromagnetic FSR treatment like PHOTOS [54], or they are used to generate the hard process in higher order in α_s, as it can be done with PowHeg [55] or MC@NLO [56].

In the second step the final state particles and particle jets of the generated events are propagated through a detailed simulation of the detector. The detector simulation is usually constructed using the GEANT4 [57] simulation tools. With this program all components that are installed in the detector can be simulated. The program then provides the most probable distribution of e.g. material interaction and energy deposition for the simulated events. The detector response for the simulated events are built from the amount of energy deposition in active detector regions as well as the multiplicity of interaction of charged particles in scintillation or silicon semiconductor detectors.

Finally, on top of the simulated detector response, the usual reconstruction of particles and the construction of control distributions can be performed. This is done in the same way as on recorded sets of data.

4.2.1. Event generation

The generation of events by Monte Carlo programs is based on the use of pseudo random numbers as introduced above. One classification of the programs, that are used to simulate the raw events, is the order in perturbation theory, which the generators are capable of respecting in their calculation. Currently in use are the multi-purpose generators of the PYTHIA and HERWIG groups. These generators are both available in well tuned versions such as PYHTIA6 and HERWIG, that are used within this analysis. Additionally there are newer setups, that are evaluated to implement more advanced calculations named PYTHIA8 and HERWIG++. In particular these two groups use different schemes to parametrise the formation of jets from partons. There is the string fragmentation method used by the PYTHIA group and the angular correlation method used by the HERWIG authors. The two methods differ in the ordering of the parton hierarchy in the formation of hadrons. The generators of both groups are treating their matrix element calculations only in leading order. The heuristic parametrisations in both setups are very

effective in modeling the formation of jets. Therefore they are in use as generator for the high statistics signal process even in precision measurements.

To improve the description of the FSR in most setups, the PHOTOS MC is used to model the multiple photon emission and QED interference. PHOTOS is commonly used among various combinations of event generators and signal processes. It can be interfaced with PYTHIA and HERWIG but also to NLO generators such as PowHeg. It is shown in [54] to improve the behaviour of electromagnetic showers when used to model e.g. in decays of $Z \rightarrow ee$.

In contrast to the two mentioned multi purpose event simulation programs the MC@NLO [56] and ALPGEN [58] generators are more specialised. These MC are only configured to generate a short list of processes. ALPGEN for instance is a leading order matrix-element generator, that is specialised on the production of multi-parton processes in hadronic collisions. Explicitly interesting for this analysis are the implemented channels of W-boson production in association with n-jets. ALPGEN is currently able to produce up to six hard jets from additional partons in association with a matrix-element hard process containing one electroweak vector gauge boson. In this analysis a previous version of the software is used and 0-5-jet-events are studied. The MC@NLO generator on the other hand is producing vector gauge bosons, heavy quark pairs and also single t-quark processes in NLO precision. Its calculations are interfaced with parton showers routines, performed by multi purpose generators like HERWIG and PYTHIA or with specialized multi-parton-process generators like JIMMY [59]. It can be interfaced to the HERWIG MC and used to refine the multi-parton radiation that are predicted in the hard process.

To properly model the probability of a specific combination of incoming partons, that take part in the event, parton distribution functions (PDF) have to be considered by the event generator. These PDF are used to weight the generated events according to the probability of the drawn combination of partons according to their momentum fractions $x_{1,2}$ and the scale Q^2 of the hard process. In this analysis PDF sets from two groups are used. From the CTEQ [37] collaboration the PDF sets *CTEQ6L1* [60] and *CT10* are used. From the MRST/MSTW group the PDF sets *MRSTLO*** [38] and *MSTW2008LO* were evaluated. Out of this list the *CT10* PDF is designed for NLO generated events, while the others are intended to be used with LO generators. The *MRSTLO*** or *MRSTMCal* PDF is a special choice in this respect as it is built for LO matrix-element generators but is modified to use the strong coupling constant "α_s at NLO and a specific prescription of the QCD coupling evolution and violation of the momentum sum rule" [38]. Especially in the production of Z-bosons it was shown to best reproduce the behavior of various distributions like the di-lepton transverse momenta p_T and rapidity with a LO matrix-element generator, compared to a choice of NLO matrix-element generator and NLO PDF.

Additional to the use of a modified LO PDF set and especially in case of the use of a LO PDF, k-factors are applied to modify the resulting LO or LOmod cross section. These k-factors correspond to the ratio of the cross sections obtained in specialised higher order cross section generators. Here the ratios consist of the cross sections derived in NLO or NNLO with the proper choice of a corresponding PDF set and those cross sections obtained from the same generator, corresponding to the order and PDF used in the event generation process. Usually these k-factors are used as global scales, but they can also depend on the mass and p_T of the hard interaction, if this is supported by the generator.

In the event generation process, also the range of kinematic variables can be restricted. Depending on the analysis requirements it can be necessary to introduce these restrictions in addition to the selection of the processes considered in the matrix-elements and the allowed decay products. This is e.g. the case for the invariant mass range of Z-bosons in the PYTHIA event generation setup.

In addition to the preselection inside the event generator setup, there is the possibility to filter out events after the event generation. With this the events are not passed to the detector simulation, which saves computing resources. This step is e.g. performed if the generator is not capable of the filtering or if an appropriate filter structure is too complex to be applied by the event generator.

Finally in Tab. 4.2 the event generators and their order in calculation are summarized. Here also the used signal and background Monte Carlo processes are listed with the corresponding PDF set, the estimated generator cross section σ_{gen}, k-factors, filter efficiencies ϵ_{gen}, effective cross sections σ_{eff} and sample luminosity equivalents.

4.2.2. Detector simulation

After simulating the physics processes, these samples have to be made comparable to measured data. Therefore not only the conditions of the particle collider like the center of mass energy have to be adjusted, but also the full detector has to be modeled. For the detector simulation the GEANT4 [57] program is used. With this all those hardware components of the detector are simulated, which are exposed to the particles generated by the event generators and in the actual measured collisions in data, respectively. In this simulation a very high level of detail has to be put on the correct orientation and dimensions as well as the density of the structures present in the experiment. This lets the detector simulation get as close to the actual construction as possible. Once all the details of the installed components of the experiment are implemented in the simulation, the parts of the detector are parametrised, that are actively used in the signal read out. In this second step of detector simulation the response of the detector to transiting and showering particle cascades is implemented. The implementation takes into account fine tuning of the response patterns towards the results of the previously mentioned test beam measurements. This lets the detector simulation and the simulated response get as close to a real measurement as possible. To study the accuracy of the default simulation, special setups of the detector layout with slightly distorted geometry are also prepared. With Monte Carlo samples using these special conditions, the systematical impact of mis-modeling of the detector can be evaluated.

Additional to the modelling of the full detector response it is possible to “outsource” some very time consuming parts of calculation of the detector response to transiting particles and showers to other tools. There are e.g. different approaches to provide the corresponding signals of the detector read out by using signal response parametrisations. In there not the full detail of every material transition and radiation is modeled, but instead there are effective response patterns defined to achieve very close agreement with respect to the full exercise. One example is the fast processing approach of the ATLFAST [61] detector description. In this setup simplified detector maps with effective material description are used. Another approach is to calculate large libraries of possible outputs of particle shower simulations. These shower libraries are used in the frozen shower package [62]. In this setup the detector response for a certain particle in a specified detector region is not simulated every time with the whole mechanism. Instead a corresponding shower from the library is used in place. This also speeds up the online calculation time for the processing of these samples, as the filling of the library has to be precomputed and can be reused for various signal signatures. Only the size of the patterns that are available in this data base has to be large compared to the number of showers actually looked up by the processing. Otherwise repeatedly appearing artifacts can occur in the event selection on data sets using such a shower library.

Process	Generator (Order)	PDF set	σ_{gen} [nb]	k-factor	ϵ_{gen}	σ_{eff} [nb]	$\int L\,\mathrm{d}t\,[\text{fb}^{-1}]$
$Z \to ee$	PYTHIA (LO)	*MRSTMCal*	0.8346	1.15	1	0.9431	(9.69) 40.9
$t\bar{t}$	MC@NLO (NLO)	*CT10*	0.146	1.131	0.543	0.090	167.6
WW	HERWIG (LO)	*MRSTMCal*	0.0310	1.48	0.389	0.0178	142.3
WZ	HERWIG (LO)	*MRSTMCal*	0.0115	1.60	0.310	0.0057	167.6
ZZ	HERWIG (LO)	*MRSTMCal*	0.0046	1.30	0.213	0.0013	196.7
$W \to e\nu$	ALPGEN (LO)	CTEQ6L1	8.7508	1.195	1	10.460	0.4 - 8.3
$W \to \tau\nu$	ALPGEN (LO)	CTEQ6L1	8.7508	1.195	1	10.460	0.3 - 8.3
$Z \to \tau\tau$	PYTHIA (LO)	*MRSTMCal*	0.833	1	1	0.833	0.59

Table 4.2.: List of generators and event sample properties of the considered signal and background processes for the analysis. The range shown for the integrated luminosity in the W samples is explained in Sec. 4.3.4 and 4.3.5.
The integrated luminosity of each sample is calculated by $\int L\,\mathrm{d}t = \frac{\sum \text{event weights}}{\sigma_{\text{gen}} \cdot \text{k} \cdot \epsilon_{\text{gen}}}$ where ϵ_{gen} is the efficiency of the generator-level event filtering.

4.2.3. Treatment of Pile-up

To treat the amount of additional simultaneous interactions in the simulation, dedicated processes are generated that cover different aspects of the additional low energetic collisions [61]. On top of the signal events also events that are categorized as minimum bias, cavern background, beam gas and halo events are simulated. These additional sources are generated in large libraries and are randomly combined and overlaid with the signal event. The detector response, that is simulated after the overlay, therefore takes into account the additional contributions and creates simulated detector signatures, which are in very good agreement to the response in data.

4.3. Monte Carlo samples considered in this Thesis

In this section the Monte Carlo samples are introduced. The description of the event generator, as well as the order in QCD that is taken into account and the chosen PDF set are mentioned. Further the cross section and the corresponding luminosity equivalent of the MC samples is given.

The samples are listed in Tab. 4.2, together with their luminosity equivalents. The integrated luminosity of each sample is calculated by

$$\int L\,\mathrm{d}t = \frac{\sum \text{event weights}}{\sigma_{\text{gen}} \cdot \text{k} \cdot \epsilon_{\text{gen}}}$$

where ϵ_{gen} is the efficiency of the generator-level event filtering. As some generators produce events with weights different from one, the sum of event weights is used rather than the number of events in the sample.

As mentioned in Sec. 4.1, the data taking is grouped in periods of varying conditions of the detector status. Further it was introduced, that for a fraction of the data issues were present to the EM-barrel calorimeters. To create Monte Carlo compatible with these conditions, the samples were divided in four subsets. These sets correspond to the four main conditions before the failure of the FEBs, the runs that are affected by the mentioned issue and two sets that correspond to about 75 % of the data taking after fixing the related hardware issues. The last two collections differ in the list of triggers that were

used in data during the corresponding periods. To construct this setup, four data runs from the different periods were chosen to define the properties for the MC sets. In Tab. 4.1 the data taking blocks are summarised. Also the fractions in the default GRL on data are listed, as well as the corresponding fractions in the simulation samples. Additionally, the details about the FEB and trigger menu conditions are displayed.

The contribution of the samples to the signal selection in this analysis, which are listed here, can originate from different sources. Events out of the chosen Monte Carlo background samples, that are passing the generation requirements, either contain at least two, one or no real electrons. This makes them behave like different groups of events, that contribute differently to the signal selections described below in Sec. 6. Events that have two real electrons are able to directly pass these respective signal selections, if the electrons kinematic conditions coincide with the acceptance criteria of the analysis channels. When combining one real electron with a light jet or two light jets with one another, the contributions can be categorized as "lepton plus jet" (ℓ+jet) or "multijet" events. These combinations of decay products behave somewhat differently than the combination of two real electrons, that have passed the signal selection in the respective di-electron analysis. In the two-electron-scenario both objects are expected to pass the respective signal selection with a rather high efficiency. These contributions are expected to behave like any combinatorial contribution of a pair of real electrons in data, as long as they are not emitted by the same parent object. In the combinations of ℓ+jet or multijet pairs, the objects originating from jets have to pass the signal selection "by accident", as the selection was defined to explicitly sort these combinations from jet-like objects out. To estimate the contribution of these subsets of the Monte Carlo inputs, one has to define special methods to recover enough events in specialised "background enriched" selections. With these selections it is possible to study the rates of fake events passing the respective signal selections. This is described in detail in Sec. 8. The contributions from real electron pairs, that can be estimated with these background Monte Carlo samples, will be summarised later as "electroweak Monte Carlo contributions", while the contributions from pairs of real and fake electron candidate objects are combined together with the multijet predictions to the respective jet-like selection of combinatorial events.

The electron pair contributions from these background samples then builds a combinatorial background, that is located in a phase space at central rapidities. It is usually uniformly distributed in ϕ. The dependencies in invariant mass and p_T tend to fall of in the tails with a power law behavior. At the Z/γ^* resonance of the respective invariant mass spectra the distributions usually are flat and don't show resonant structures. This is of course not the case if the respective background sample contains e.g. a pair of electrons that originates from a Z-boson. This can happen in the Diboson Monte Carlo in the ZZ and WZ samples. Also in W-decays and $Z \to \tau\tau$ there is a correlation between the electron candidates that results in resonant structures.

4.3.1. $Z/\gamma^* \to ee$ Monte Carlo

The signal Monte Carlo in this analysis is generated with the PYTHIA event generator that is able to produce event predictions for the hard interaction in leading order (LO). It uses a parton shower mechanism that is capable of describing the fragmentation and hadronisation of partons by heuristic schemes to a very good degree. With this it models the amount of initial state radiation (ISR) that occures on the level of strong interactions in parton collisions. The final state radiation (FSR), that is dominated by electromagnetic effects in the chosen decay channel, is taken care of by the PHOTOS [54] event generator, that is by default interfaced with PYTHIA in the ATLAS setup. To further cope with the fact that PYTHIA only produces predictions with LO matrix-elements, a PDF was chosen that is trying to modify the resulting distributions of a LO generator to represent the shape of a proper NLO setup.

This set of parton distribution functions is provided by the MRST collaboration in their *MRSTMCal* PDF set.

The signal process, that is produced by the above mentioned combination of generators and PDF, is $pp \to Z/\gamma^* \to ee$. Here the allowed range for the invariant mass of the gauge boson is defined to be above a lower bound of 60 GeV. The resulting LO cross section is 0.8346 nb, given the mentioned LO modified PDF of this signal process. These features are summarised in Tab. 4.2 together with other Monte Carlo processes, that were investigated as contributions to the combinatorial background in the analyses discussed hereafter. To further describe the differences in the LO to NNLO behaviour of the signal process, k-factors were calculated depending on the invariant mass of the Z-boson. These scales increase the cross section by on average about 15.4% to 0.969 nb. The sample contains about 40 million events and corresponds to an integrated luminosity of about 40.9 fb^{-1}, taking into account the LO cross section and the k-factors.

4.3.2. $t\bar{t}$ Monte Carlo

The $t\bar{t}$ MC is generated with the MC@NLO event generator that produces events according to NLO matrix-elements. For the generation of the events the *CT10* PDF set of the CTEQ collaboration is used. The generator is set up to produce a sample of pure $t\bar{t}$ events that corresponds to a production cross section of 0.146 nb. After the processing a set of event filters are applied. These filters preselect events that contain leptons in the prompt W-bosons, which are radiated off the top quarks. The filter efficiency is 54.3% for the events in the official sample. So finally an effective cross section of 0.09 nb is applicable for the events in this sample. With the roughly 15 million events in the sample the data set corresponds to a luminosity of about 168 fb^{-1}. The real electrons in this background sample are produced by the decay of the W-bosons in the decay chain of the t quarks. As the filter applied at generation requires at least one lepton to be in the decay products of the two W-bosons, there are a number of channels with semi-leptonic signature containing one lepton (e, μ, τ) together with one jet or two leptons (ee, $e\mu$, $e\tau$, $\mu\mu$, $\mu\tau$ or $\tau\tau$). The τs also have a chance to decay into electrons, muons and jets, so there are three groups of decay combinations available again. The events can again be grouped in one contribution with two real electrons, either directly from the W or with intermediate τ decays. Additionally there are the ℓ+jet contribution, where the jet can originate from the other W-boson, a τ decay or just one of the b quarks, that is radiated off the initial pair of t quarks. Finally there are various combinations of multijet signatures not containing a real electron in the generation of the hard process and its direct decay products.

4.3.3. Diboson Monte Carlo

The Diboson Monte Carlo samples consist of the production of pairs of electroweak gauge bosons. Here the production of WW, WZ and ZZ are taken into account. The samples are generated with the HERWIG Monte Carlo using the already mentioned *MRSTMCal* PDF. This is done to improve the description of the LO generator to be more comparable with NLO results that should be closer to data. The cross sections of the three processed channels range from 4.6 pb for the ZZ sample to 11.5 pb in the WZ sample to about 31 pb in the WW sample in leading order. Going from this level to NLO the k-factors for these samples that are used as global cross section factors range from 1.30 (ZZ) to 1.44 (WW) and 1.60 in the WZ sample. Additionally there are lepton filters applied in the generation of these samples that range from about 21% to 39%. Because also the higher order corrected cross sections for these processes and the filter efficiencies, that are very low, the 0.25 million events in the ZZ sample and the other 1 million

extra partons	σ_{gen} [nb]	k-factor	σ_{eff} [nb]	events in $W \to e\nu$	$\int L\,\mathrm{d}t\,[\mathrm{fb}^{-1}]$ $W \to e\nu$	events in $W \to \tau\nu$	$\int L\,\mathrm{d}t\,[\mathrm{fb}^{-1}]$ $W \to \tau\nu$
0	6.93	1.195	8.287	3388883	0.409	2608260	0.315
1	1.305	1.195	1.560	2499645	1.602	1409172	0.903
2	0.378	1.195	0.452	3768632	8.338	3489922	7.725
3	0.102	1.196	0.1218	1008947	8.284	1009925	8.284
4	0.0257	1.195	0.0307	250000	8.143	249991	8.135
5	0.0070	~1.2	0.0084	69999	8.333	64998	7.729

Table 4.3.: Detailed Monte Carlo sample information for $W \to e\nu$ + jets and $W \to \tau\nu$ + jets events generated with APLGEN Monte Carlo as described in Sec. 4.3.4 and Sec. 4.3.5. The approximately same conditions are present for the $W \to e\nu$ and $W \to \tau\nu$ sample except for the slightly smaller statistics in $W \to \tau\nu$.

events in the WZ and WW samples each are representing a luminosity equivalent of around 140 to about 200 fb^{-1}.

In the generator configuration semi-leptonic decays are required which means that at least one electron muon or tau has to be present as a decay product of the vector boson pair. This further means that only in every third event an electron has to be present. On the other hand the contributions from events that are not containing any electron in the hard process are included if at least one other charged lepton is present. The diboson events that decay into quark pairs only are thus not included in the sample and have to be estimated by data driven multijet techniques.

4.3.4. $W \to e\nu$ Monte Carlo

The $W \to e\nu$ Monte Carlo sample consists of several inputs. The process is generated with ALPGEN at leading order but the sample is separated in subsets containing a fixed number of hard partons radiated off the hard process. The sets are ranging from 0 to 5 partons forming jets next to the produced W-boson, which decays into an electron and a neutrino. In this sample the leading order PDF CTEQ6L1 is used which is not trying to modify the parameters for the strong interaction as it is done in the *MRSTMCal* approach. Instead in this setup the cross sections for the individual parton multiplicities are defined accordingly to match the occurrence in data to best knowledge. The production cross section in the six samples varies on this behalf. The first and last sample differ in their cross section by three orders of magnitude. The details on all production cross sections, the applied k-factors, numbers of events available in the samples and the resulting luminosity equivalents are listed in Tab. 4.3. Although the Monte Carlo is already binned in the mentioned condition of extra partons, the statistics is not sufficient to describe the invariant mass spectrum above a threshold of about 300 GeV in the current di-electron selection. To overcome this the remaining ℓ+jets and multijet contributions that originate from $W \to e\nu$ events have to be estimated by the respective multijet method in this mass range on data.

4.3.5. $W \to \tau\nu$ Monte Carlo

The $W \to \tau\nu$ Monte Carlo sample also consists of several inputs as described above in Sec. 4.3.4 for $W \to e\nu$. The samples for the $W \to \tau\nu$ + jets process contain 56% (1-jet) to 100%(3- and 4-jets) of the statistics of the samples in the $W \to e\nu$ + jets Monte Carlo. Therefore the luminosity equivalent of these samples ranges from 0.3 to 8.3 fb^{-1} with respect to 0.4 to 8.3 fb^{-1} in the $W \to e\nu$ sample. Although the

Monte Carlo is already binned in the mentioned condition of extra partons, the statistics is not sufficient to describe the invariant mass spectrum even earlier than the threshold of about 300 GeV seen in the $W \to e\nu$ samples. To overcome this the remaining ℓ+jets and multijet contributions that originate from $W \to e\nu$ events have to be estimated by the respective multijet method on data. This is especially in the $W \to \tau\nu$ Monte Carlo the case because the produced τ leptons only decay by a rate of ~18% to electrons.

4.3.6. $Z \to \tau\tau$ Monte Carlo

The $Z \to \tau\tau$ process is generated almost identical to the $Z \to ee$ signal process discussed in Sec. 4.3.1. Here also the PYTHIA Monte Carlo was used interfaced with PHOTOS for the FSR photon handling. The PDF is again *MRSTMCal*, estimating partly the NLO contributions to the cross section and line shape. Further the signal cross section a generator level with the modified LO PDF is at 0.833 nb and no event filter is applied. Differently to the $Z \to ee$ sample the $Z \to \tau\tau$ process is not scaled by a k-factor to NLO or equivalent cross section. The sample is generated with 0.5 million events only which corresponds to a luminosity of only 0.59 fb^{-1}. This leads to poorer statistics in the tails of the available phase space. As the expected event rate is low anyway the small number of events in this sample mostly contributes as a slightly enhanced statistical uncertainty of the sum of background processes. Electrons of course appear in the decay of the τ leptons, while fake contributions to the selection can either originate from the τs or jets in the remaining activity in the event.

5. Electrons in ATLAS

In this chapter generic features of particle reconstruction in ATLAS are introduced. On this basis the necessary electron candidate definitions are collected. The electrons are interacting with the detector by ionisation of read out cells in the tracking systems. Further they leave electromagnetic showers in the EM components of the calorimeter system. Due to the overlap with the signals of photons as well as light hadrons the official selection criteria of the eGamma performance group [63, 64] are discussed. This group defines and optimizes the selections to distinguish electron and photon signals from jets and light meson decays. Further the calibration of the electron and photon energy response in data and Monte Carlo as well as the monitoring of the raw measured data are provided by the analysts working with the eGamma group.

In [63] the electron performance of the 2010 data taking is evaluated while the internal ATLAS reference [64] introduces the changes that were invented during the first data periods of 2011.

5.1. Particle Reconstruction

In the particle reconstruction the raw information from the detector components have to be interpreted in terms of signatures that different particles leave behind in the detector materials. These signatures are built from two main classes of detector responses that can be defined as tracks from charged particles and energy depositions. Particle tracks are constructed from aligned hits in the ID and Muon tracking systems while energy clusters are built from calorimeter cells responding to particle showers. For this purpose dedicated reconstruction algorithms are implemented to construct these objects.

Only a general impression of the particle reconstruction in relevant detector sections is given here. A full list of the available reconstruction algorithms is given in [19].

5.1.1. Tracking and Vertex Reconstruction

To reconstruct tracks in the ID the hits found in Pixel detector and SCT are defined as 3-dimensional space points. From these hits track segments of two aligned hits in the Pixel detector are selected. Starting with these seed tracks further hits in adjacent outer layers are successively added to the proto tracks. Each time another space point is added the tracks are refitted by a parametrized track function judging the probability the combination of hits is originating from an actual particle passing the detector. After taking all layers of the silicon detectors into account the tracks are expanded for hits in the straw tubes of the TRT and refitted again.

When all possible tracks are defined they are extrapolated to the interaction region inside the beam pipe to find the interaction points the particles were originating from. For this purpose tracks that have a minimum distance of approach are used to construct vertices. These vertices that build the common origin of multiple tracks are in the last step taken into account for a final refitting of the tracks. The final

set of tracks is now extrapolated outside of the volume of the ID, to define the most probable points of entering the calorimeters.

5.1.2. Cluster Reconstruction

Here only a general impression of the concept of cluster reconstruction is given, as the definition of electrons in ATLAS is introduced in more detail below.

To define a set of cluster candidates the list of calorimeter cells has to be preselected for cluster seeds. These proto clusters are usually cells with local energy maxima or local maxima in the signal-to-noise ratio of the cells read-out energy. Around these seeds, a cluster can be defined by selecting a fixed size window that is optimized to maximize the energy of the contained electrons (Sliding Window Cluster). Alternatively neighbouring cells which exceed certain signal-to-noise thresholds can be clustered around the seed cells (TopoCluster). Both schemes are used to define candidates for electrons and photons in different regions of the calorimeters. Additionally there are algorithms that cluster calorimeter cells by the ordering of their distance and p_T relations. These classes of reconstruction algorithms are used e.g. to define jets.

The sliding window cluster algorithm is performing a variety of precomputed analysis classifications. It provides the measurement of the cluster energies in various window sizes ranging from 3×3 to 7×7 cells corresponding to the usual cell dimensions in the second layer of the EM calorimeters. It further provides different combinations of shower shape properties for the identification of electrons and photons. The topological clustering algorithm also provides he cluster energies and is defined upon a set of cluster moments, to perform shower shape categorisation.

5.2. Reconstruction of Electrons in ATLAS

The central electron acceptance is defined by the reach of the trigger and tracking systems. Up to a pseudo rapidity of $|\eta| \lesssim 2.5$ tracks are measured and energy depositions are taken into account by the trigger algorithms that look for electrons. Due to the lack of tracking information corresponding to the remaining calorimeter coverage of $2.5 < |\eta| < 4.9$, electrons depositing energy in the forward regions of both end-cap regions cannot be asked for their charges. This implies that there is no further distinction of electrons and photons as well, because the form of the energy depositions in the calorimeters of these particles is basically indistinguishable for application purposes. Also the rate of jets that decay into the forward region is higher than in central. The information which algorithm is used to reconstruct the electron object is stored in a variable called electron author.

5.2.1. Central Electrons

The electron reconstruction algorithm for the "standard electron author" in the central detector acceptance is seeded by the sliding window cluster algorithm. The energy depositions in a window of 3×5 cells in the second layer of the EM calorimeters have to exceed 2.5 GeV. Further the position of the seed cluster is required to match to a track candidate within a distance in $\Delta\eta \times \Delta\phi$ of less than 0.05×0.10[1].

[1] If more than one track candidate is found, the one that matches the cluster position best is chosen. Otherwise the cluster is rejected from the list of electron candidates. Tracks with more silicon hits are preferred

The momentum of the track has to match the energy in the cluster as well. This is checked by the requirement of $E_T/p_T < 10$, which is fulfilled by about 93% of real electrons with a transverse momentum above 17 GeV. The default definition of the size of an electron cluster is 3×7 (5×5) cells of the second layer in the barrel (end-caps) of the calorimeter. The energy of the electron candidate is evaluated accordingly.

The energy of an electron candidate takes into account contributions of four sources: energy estimated for the losses in material in front of the EM calorimeter, the energy measured inside the cluster which is to be corrected for the energy responses in the different samplings, the energy estimated due to lateral losses outside the cluster but within the EM calorimeter samplings and the longitudinal energy losses due to overlap of the shower into the hadronic calorimeter sections. The direction properties of the electron candidates (η, ϕ) are taken from the associated track measurements. Here the tracks have to have at least four hits in the silicon modules to ensure a base line track quality.

5.2.2. Forward Electrons

In contrast to the clustering in the central region, the forward electron energy depositions are reconstructed with a topological clustering algorithm producing TopoClusters [65]. Here the clusters do not have a fixed size but instead the corrections with respect to the out-of-cluster energy depositions are easier to handle. The clustering algorithm is topologically taking into account all cells around a seed cell that is used to start the clustering. The adjacent cells do not have to be located in the same sampling but just have to be neighbours to the proto cluster.

Cells that are to be clustered by this algorithm are sorted by their signal-to-noise ratio. The seed cell of a cluster is found in an "ideally empty" event by selecting the cell with the highest of three clustering thresholds in the signal-to-noise ratio - the *seed* threshold t_{seed}. Each of these cells in the current event is filled into a list and used to define proto clusters. For each proto cluster a list of adjacent cells is built. Cells that exceed the next threshold $t_{neighbour}$ are added to the corresponding proto cluster. The final step adds cells to the current *neighbour* proto clusters if they exceed the third threshold t_{cell}. This step is not iterated over the full list of cells that fulfill the third threshold requirement, but only once for the outer most shell of cells of these clusters. Every time a cell is to be added to more than one neighbouring proto clusters, the two clusters are merged.

The thresholds of signal-to-noise ratios are chosen to be $4/2/0$ for $t_{seed}/t_{neighbour}/t_{cell}$. The value of $t_{cell} = 0$ means, that if there are cells left around the proto cluster after adding the *neighbour*ing cells, all of them are added to build a full shell. In contrast to the sliding window algorithm used in the central region the TopoCluster algorithm is running on all calorimeter cells in the selected detector acceptance. This means that not only the cells of the EMEC-IW and the first layer of the FCal are used but all cells also from the HEC and the other two FCal read-out compartments. The energy measurement takes into account the calibrated cell energies but does not perform a selection on the positive part of the energy response or the absolute cell energies as it is possible in some variations of the TopoCluster algorithm. This way the energy variations induced by electronics and pile-up noise are expected to cancel out more efficiently with respect to dedicated event-by-event noise corrections. Further the signal-to-noise ratios used in the clustering are applied on frequently updated noise maps to take into account the most recent level of activity in the detector.

To use a cluster found by the clustering algorithm as an electron candidate only a minimal transverse energy cut of $E_T > 5$ GeV has to be passed. With this of course the efficiency of real electrons is rather high but in the same respect the purity is rather low taking into account the large hadronic activity when going higher in pseudorapidity and closer to the beam line.

5.3. Identification

The identification requirements (*EM-id*) in both the central and forward regions are divided into sets of three selections that are called *loose*, *medium* and *tight*. The respective selections and the corresponding requirements are chosen to be inclusive with respect to one another. This way the *medium* and *tight* selections always include the requirements of the *loose* selections. Correspondingly the *medium EM-id* is included in the *tight EM-id*.

The full list of variables that are used in the identification selections is shown in Tab. 5.1 and Tab. 5.2 for central and forward electrons respectively.

5.3.1. Central Electrons

The central electron identification is based on quality criteria that are applied on the information of the associated tracks the clusters and the respective matching between tracks and clusters. It is structured in a detector geometry driven binning in 10 bins in cluster-$|\eta|$ and a statistics driven range of 11 bins of E_{T} (from 5 GeV to 80 GeV). The requirements are chosen to provide a good separation between the (isolated) signal electrons and fake electron contributions from hadrons in background processes. Further non-isolated electrons from semi-leptonic decays and electrons from photon conversions can be separated as well.

During the 2011 data taking, the identification requirements of the central electrons were reevaluated which leads to two sets of identification selections. The old sets *loose*, *medium* and *tight* were used in the first half of the 2011 data taking in the trigger conditions and were replaced by the set of improved selections called *loose*++, *medium*++ and *tight*++. The "++" *EM-id* selections are the ones used in the analysis but the older sets have to be used as well as they are a feature of the trigger selections.

Loose identification requirements:

The requirements used in the *loose*++ selection contain conditions on the energy leakage into the hadronic compartments, and lateral leakage restrictions on the first and second EM calorimeter layer. Further minimal tracking requirements have to be fulfilled for the *loose*++ identification and a maximal deviation of the track and cluster position in the first sampling is added to the list of conditions.

The requirements on the track information as well as the information on the first calorimeter layer are added with respect to the earlier definition of the *loose* identification criteria. This way the rejection of hadronic contributions is improved while the signal efficiency can be kept at a high level. This leads to the situation that the electron *loose* definition of the old *EM-id* set is almost identical to the requirement of the photons and at least includes the photon quality level. Taken this into account the old *loose* photon triggers can easily be used for *loose* electrons as well.

Medium identification requirements:

In the *medium*++ *EM-id* the requirements on the track and track matching to the cluster are increased. There has to be a hit in the first layer of the Pixel detector - the b-layer - for values of $|\eta| < 2.01$ or at least one hit in the Pixel system for the remaining tracking coverage. Additionally the maximal

Category	Description	Variable
	loose++	
Acceptance	$\|\eta\| < 2.47$	
Hadronic leakage	Ratio of E_T in the first layer of the hadronic calorimeter ($\|\eta\| < 0.8$ and $\|\eta\| > 1.37$) or E_T in whole hadronic calorimeter ($\|\eta\| > 0.8$ and $\|\eta\| < 1.37$) to E_T of the EM cluster	$R_{had,1}$, R_{had}
Middle layer of the EM	Ratio of energies in 3×7 cells over 7×7 cells	R_η
	Lateral width of the shower	$w_{\eta 2}$
Front layer of the EM	Total shower width	w_{stot}
	Ratio of the energy difference associated with the largest and second largest energy deposits in the cluster over their sum	E_{ratio}
Track quality and track-cluster matching	Number of hits in the pixel detector (≥ 1)	
	Number of hits in the pixel and SCT detectors (≥ 7)	
	$\Delta\eta$ between the cluster position in the first layer and the extrapolated track (< 0.015)	$\Delta\eta_1$
	***medium++* (includes *loose++*)**	
Track quality and track-cluster matching	Number of hits in the b-layer > 0 for $\|\eta\| < 2.01$	
	Number of pixel hits > 1 for $\|\eta\| > 2.01$	
	Transverse impact parameter < 5 mm	d_0
	Tighter $\|\Delta\eta_1\|$ cut (< 0.005)	
TRT	Loose cut on TRT high-threshold fraction	
	***tight++* (includes *medium++*)**	
Track quality and track-cluster matching	Tighter transverse impact parameter cut ($\|d_0\| < 1$ mm)	
	Asymmetric cut on $\Delta\phi$ between the cluster position in the middle layer and the extrapolated track	$\Delta\phi$
	Ratio of the cluster energy to the track momentum	E/p
TRT	Total number of hits in the TRT	
	Tighter cut on the TRT high-threshold fraction	
Conversions	Electron candidates matching to reconstructed photon conversions are rejected	

Table 5.1.: Selections and variables used in the *loose++*, *medium++* and *tight++* electron identification criteria in the central region of the detector ($|\eta| < 2.47$). Taken from [64].

Category	Description	Variable
Acceptance	$2.5 < \|\eta\| < 4.9$	
Shower depth	Distance of the shower barycenter from the calorimeter front face measured along the shower axis	λ_{center}
Maximum cell energy	Fraction of cluster energy in the most energetic cell	f_{max}
Longitudinal second moment	Second moment of the distance of each cell to the shower center in the longitudinal direction (λ_i)	$\langle\lambda^2\rangle$
Transverse second moment	Second moment of the distance of each cell to the shower center in the transverse direction (r_i)	$\langle r^2\rangle$
Normalized lateral moment	lat_2 and lat_{max} are second moment of r_i for different r_i settings per cell	$\frac{lat_2}{lat_2+lat_{max}}$
Normalized longitudinal moment	$long_2$ and $long_{max}$ are the second moment of λ_i for different λ_i settings per cell	$\frac{long_2}{long_2+long_{max}}$

Table 5.2.: Variables used to identify electrons in the forward region of the detector ($2.5 < |\eta| < 4.9$). Taken from [64].

deviation in the extrapolated track position and the energy barycenter in the first calorimeter layer is reduced again by a factor three and loose requirements are introduced on the information from the TRT (where available). In the older medium requirements neither the TRT nor the conditions of the b-layer are included. Instead most of the additional requirements in *loose++* with respect to *loose* are defined at this level.

Tight identification requirements:

The remaining available requirements that are defined in the eGamma list of identification conditions are used to build the *tight++ EM-id*. It includes a stronger restriction of the impact parameter of the electron track and the cluster energy to track momentum ratio. Further tighter conditions are set on TRT hits as well as a veto on electrons from photon conversion is requested.

Additional identification requirements:

There are other quality requirements that can be applied to central electrons on top of the "++" ID selections. It has been shown though that conditions of properties like isolation are behaving analysis dependent and that these can not be recommended in a generalised way with respect to the globally defined sets of *EM-id* selections above. Therefore it is left to the analysis groups to agree on isolation based conditions and check their performance in data and MC.

5.3.2. Forward Electrons

In the forward region only a reduced set of variables is available. These variables are defined as cluster moments[2] of degree n, which are listed in Tab. 5.2. As mentioned above also here three quality levels are

[2]Cluster moments of degree n are defined as

$$\langle x^n\rangle = \frac{1}{E_{\text{norm}}} \times \sum_i E_i x_i^n,$$

where $E_{\text{norm}} = \sum_i E_i$ and i is the index of the cells in the cluster.

defined. These three reference sets are also required to be inclusive but in contrast to the central electron identification all sets use all variables. To define the three quality levels inclusive to one another in the correct order, the cuts on the individual variables are required to be inclusive as well. The *EM-id* levels are further not binned in the transverse energy, but due to the high influence of the hadronic contributions that strongly depend on the level of pile-up in the event, the *EM-id* criteria are binned in 10 bins in $|\eta|$ and four bins in N_{PV}. The binning in pseudorapidity is chosen to provide six bins in the EMEC-IW in $2.50 < |\eta| < 3.16$ and three bins in the FCal at $3.35 < |\eta| < 4.90$. The tenth bin is covering the transition region between the two calorimeters that is currently less well understood and calibrated. The binning in N_{PV} takes into account the number of primary vertices that are reconstructed in the event. Therefor it allows to adapt the selection cuts to provide a flat signal efficiency curve also with respect to the pile-up conditions. The signal efficiency in the three selections drops from about 90% in the *forward-loose* set to 80% and 70% in the *forward-medium* and *forward-tight* set. The rejection power on the other hand increases by about a factor two to three from *forward-loose* to *forward-tight*.

5.4. Trigger

In the trigger system the signal candidates of electron signatures have to pass three layers of trigger architecture in ATLAS. The candidates are seeded by calorimeter trigger towers of the CPM as defined in Sec. 3.2.6, that covers a range up to $|\eta| = 2.5$ by the L1Calo calorimeter trigger. The selected ROIs in the respective events are passed on to the second trigger stage (L2) that performs a full electron reconstruction inside the given ROI but uses a simplified tracking algorithm to match the time constraints in the event buffering system. After a positive decision, the L2Accept is fed to the EventFilter for a trigger decision on the fully reconstructed event. Because the L2 and EF triggers are implemented on the same computing farm, also here the simplified tracking algorithm is used. In the HLT, at least with respect to the L1 system, the remaining reconstruction of the electron candidates and the identification algorithms are identical to the offline definitions described above. As mentioned in the identification section of the central electrons there are two collections of *EM-id* requirements defined that are used at different periods of the data taking. In the periods listed in Tab. 4.1 indicating the trigger menu v2 the older electron identifications were used in the single electron triggers. The trigger menu v3 only contains electron triggers in the HLT that use the updated set of ++ *EM-id*s. With respect to that, one specific trigger based on two loosely identified photons with at least 20 GeV of E_{T} is kept in both trigger menus. This trigger signature was kept in the menu and did not get prescaled to allow the analysis groups trying to discover the Higgs boson keep their base line trigger setup for the $H \rightarrow \gamma\gamma$ channel.

In the region of forward electrons no trigger is installed specifically for electrons. In principle the jet triggers are possible trigger signatures but they are not recommended due to prescales and low fraction of electron signals in the respective streams. Therefore all events considered in this study use either single electron or di-photon triggers depending on the analysis channel.

6. Baseline event selection

In the following paragraphs, corrections and preselections to the data taking and the baseline event selection criteria of this analysis on the Forward-Backward-Asymmetry are discussed. In Sec. 6.1 the correction and preselection topics are introduced while the mentioned criteria are defined in Sec. 6.2. The selection is applied to data and all contributing Monte Carlo samples. For the estimate on the contribution of multijet events entering the signal selection from data, dedicated routines are introduced in Sec. 8.2. Finally a comparison of the corrected data and MC selections is shown in Sec. 8.3.

The selection is split into two separately studied channels where one of them is requiring the events to contain two well measured electrons that are reconstructed in the central region. This channel is referred to as CC. The other channel is trying to expand the reach in di-electron rapidity covered by the selected events with the inclusion of forward electrons. Here it is chosen to use one central and one forward electron and use adequately different trigger and identification requirements to also keep a well defined signal selection that has a manageable level of background it. This channel is further referred to as CF.

The general structure and several selection requirements are the same as the cuts used in the energy calibration study discussed in Sec. 7.1.1. To study the selections defined for these channels first the selection requirements are listed and described. Then there is a study performed on events where the reconstructed electrons are matched to the true electrons the Z/γ^* boson in the signal Monte Carlo is decaying to. After that the selection is performed on the reconstructed electrons in data and the full set of events of the signal MC.

6.1. Corrections and Preselections to Data and Monte Carlo

To assure that all known problems in data taking as well as differences in the conditions of the Monte Carlo setup with respect to the measured conditions in data are taken into account, a list of corrections and preselections that can be applied are discussed in this section. There are preselections available for the cleaning of the data sets, and corrections that act as scale correction factors on the Monte Carlo.

6.1.1. Preselections on data

The recorded data sets are containing events which include issues of the data quality as introduced in Sec. 4.1. These issues include the readiness of different components that are mandatory for the data taking as well as data quality criteria of various physics objects. Also specific regions of the detector that show flaws in their response are flagged in this respect.

- Good Runs List:

  The GRL is meant to contain a list of events, or more precisely at ranges of luminosity block numbers, in which the detector components have been working within a specific level of data collection conditions. As discussed in Sec. 4.1 the GRL used in the analysis is only applied on data. For some analyses it is tolerable that detector components, they don't gather information from, are not working under nominal conditions while for others these features are non tolerable. GRLs are built to respect these requirements and provide lists of data segments that were taken with all respective requirements fulfilled. Depending on the GRL chosen by the individual analysis, the available number of events and therefore the luminosity of the remaining data set is determined.

- Object quality criteria:

  The criteria concerning the object quality are also a preselection which has to be applied on the basis of single electrons. It is related to the failure of the FEB electronics as introduced in Sec. 4.1. On the other hand this correction is identical for data and simulation. There are further no scale factors applied to improve the matching of data and MC. More precisely the corrections that are applied are already taken into account in the pile-up reweighting, where the four chunks of data taking are weighted in the Monte Carlo according to their occurrence in data.

6.1.2. Corrections applied on event properties

The corrections discussed below are a collection of recommendations of different performance groups within the ATLAS experiment. All these corrections are either officially asked for or at least recommended to be usable in the physics and performance analyses.

- k-factors:

  The k-factors already mentioned in Sec. 4.3, can either be defined as global scales to the cross section or they can be calculated depending on some properties of the events. Here e.g. the invariant mass of a generated gauge boson in the hard process can be the kinematic dependency the k-factor is evaluated in. This is e.g. the case for the PYTHIA $Z/\gamma^* \rightarrow ee$ sample.

- Pile-Up:

  As discussed in Sec. 4.1 and Sec. 4.2.3 the conditions of the Monte Carlo samples do not match to data in the distribution of simultaneous interactions. Additionally the weighting of the four chunks of data taking is to be corrected as well. These corrections are determined upon the distribution of simultaneous interactions simulated in the MC as well as measured by the beam monitoring systems in data. To accurately apply the correction on the Monte Carlo, the pile-up reweighting tool has to be initialised with these distributions. It is built to scale the events in simulation on-the-fly towards the measured distributions in data.

- Vertex Position Reweighting:

  The distribution of interaction vertices in z-direction along the beam axis is simulated wider in the available Monte Carlo samples as it is recorded in data. The gaussian distribution of the interaction points can therefore relatively easy be reweighted to the distribution in data.

- Boson p_T Reweighting:

  Finally there has been the need to compare the distribution of p_T of the Z-boson between the current version of the samples provided by the ATLAS collaboration and the samples defined for the 2010 data taking. It was found that with different generator tuning parameters the 2010 p_T^Z distributions were fitting the same distribution in 2010 data events as well as in 2011 data events better than the 2011 Monte Carlo tunes. Out of the two simulation samples scale factors were derived in p_T^Z as well as $m_{\ell\ell}$ to reweight the 2011 samples to better match data in the 2011 data sets. The same correction is available for analyses with W-boson decays as the signal process.

6.1.3. Corrections on electron properties

The corrections discussed below are applied on the basis of single electrons and are recommended by the eGamma group. These corrections are taking into account the official sets of parameters, that are recommended to be applied in all analyses using electrons.

- Electron Energy Scale and Resolution:

  This calibration is meant to shift the measured data energy response by a calibration factor towards the values obtained from the signal Monte Carlo after detector simulation, particle reconstruction and identification. These calibrations are explicitly not meant to calibrate energy scale and resolutions to values known at generator level. They are meant to inter-calibrate the response in data to the full detector simulation. The calibration is taking into account a reference identification selection that is recommended to consistently study the systematic variations to this calibration. Parameters similar to the energy scale are determined for the resolution of the data and Monte Carlo samples. The correction factors are used to broaden the resolution of reconstructed and identified simulation events to achieve the resolution obtained in data using the same selection requirements.

  The parameters used in this analysis are recommended by the egamma group. The calibration of the energy scale and resolution parameters are taken from the official recommendations. The set of parameters to correct the forward electron energies had to be re-derived for this thesis. So these parameters and the definition of the calibration mechanism is explained in detail in Sec. 7. The extracted calibration constants and results from systematic variations were included back into the previously mentioned set of official recommendations for the 2011 data and Monte Carlo corrections.

- Selection Efficiencies and Scale Factors:

  The selection efficiencies for the electron reconstruction, the trigger response, as well as the various identification requirements of the official *EM-id*s have been intensively studied for data and Monte Carlo on central as well as on forward electrons in the 2011 samples. These efficiencies have been compared in bins of $|\eta_e|$ and p_T^e or $|\eta_e|$ and N_{PV} respectively. The scale factors are build two-dimensional in these respective quantities and are applied on the selected events in the simulated samples to recreate the performance in data to best knowledge.

6.2. Definition of selection requirements

The following event selection criteria or cuts are used on the CC and CF electron pairs to give a baseline data set for the analyses discussed in the following sections. The set of corrections and preselections introduced in Sec. 6.1 is fully taken into account at this point.

Cut	short name	description
1.	official GRL on data and pile-up reweighting on MC	data11_7TeV.periodAllYear_DetStatus-v36-pro10_CoolRunQuery-00-04-08_Eg_forward.xml
2.	vertex cut LAr error cleaning	suppression of cosmic muon events cleaning for intolerable conditions of LAr calorimeters (high voltage issues, noisy channels)
3.	Trigger CC Trigger CF	lowest unprescaled di-em-object trigger using 2 loosely identified photon candidates (EF_2g20_loose) lowest unprescaled single em-object trigger using 1 medium identified electron candidate per period (EF_e20_medium (B-H), EF_e22_medium (I-K), EF_e22vh_medium1 (L-M))
4.	≥ 2 electrons	after this cut the pair based selections are performed
5.	electron author cut	central electrons: 1 or 3 (standard eGamma electron algorithm) forward electrons: 8 (eGamma forward electron algorithm)
6.	pseudo rapidity acceptance and cleaning	central: $\lvert\eta_e\rvert < 2.47$ forward: $2.5 < \lvert\eta_e\rvert < 4.9$ veto of transition regions: $1.37 < \lvert\eta_e\rvert < 1.52$ and $3.16 < \lvert\eta_e\rvert < 3.35$
7.	electron momentum	$p_T^e > 25$ GeV to be above trigger thresholds
8.	object quality cleaning	cleaning cuts on electron around the affected regions of the FEB defects
9.	channel *EM-id* selections	CC: *medium++* and opposite electron charge CF: *tight++* for central, and *forward-medium* for the forward electron as well as central electron isolation (*IsoPtVtxCorrected*)

This list consists of criteria are to be applied on event by event basis like the points 1 to 4. From cut 5 to 9 the selections are applied on an electron pair basis for each event. The criteria are applied sequentially and events are discarded if either an event based requirement is failed or if no pair of electrons fulfills the requirement of a given pair based selection cut.

1. The first cut is to clean the event list in data in terms of good data quality requirements. The term GRL refers to a Good Runs List as defined in Sec. 4.1 that lists sub-passages in the non-continuous data recording where the experiment was in good conditions. It is defined upon a list of quality constraints that were checked during data taking. Out of this list of sub-system conditions, it can be chosen whether a potential issue within a sub system is being treated as a tolerable or intolerable issue to the analyses using the particular GRL. If a sub-system is flagged with an intolerable defect, the related period of time the flag is up would be removed from the corresponding GRL. An issue can be treated as tolerable, if the analyses e.g. are not taking any information out of the affected sub-system into account. Even the quality of the LAr system and the calorimeters, that is essential to the measurement of electrons and photons, are in some specific flags only checked for LumiBlocks with intolerable deficits while tolerable issues are not removed by the GRL. This

selection is based on the use of the additional requirements of the LAr error veto, that is required to be checked in the event based selection of the analyses.

2. In selection cut two the mentioned additional event-by-event quality flag is checked to show nominal conditions in the LAr system of the calorimeters. This requirement was promoted from the configuration of the GRL to the analysis to recover LumiBlocks that only had very few events with issues in the LAr system. This way larger sequences of events could be recovered for the analyses. Additionally in this cut the event is also required to have a well defined vertex of tracks reconstructed that needs to have a minimal track multiplicity. This requirement is a generic event cleaning requirement to reduce the contributions of high energetic cosmic muons in the event selection.

3. The triggers chosen in these analyses are supposed to be unprescaled. This means that every event that fires a trigger has to be written out. The trigger requirement for the CC channel is based on a pair of loosely identified photons that exceed a minimum transverse energy of 20 GeV in the Event-Filter of the high level trigger system. In the CF channel only one electron candidate is in the acceptance of the EM triggers so a more restrictive single electron trigger is chosen. Here the triggered electron has to exceed a minimum transverse energy of 20 to 22 GeV and a corresponding medium flavored *EM-id*, depending on the data taking period. The triggers are seeded by L1Calo trigger items where $E_{\mathrm{T}}^{\mathrm{trigger}}$ exceeds thresholds of 14 GeV for the 20 GeV HLT items and 16 GeV for the 22 GeV HLT items. The L2 items have the same requirements as the respective EF items.

4. The fourth cut requires to have at least two electron like objects to be reconstructed in the event. This is only supposed to provide that the following selections can be applied on pairs of electrons.

5. In the fifth cut the electron candidates are checked for the reconstruction algorithm they are found with. The corresponding algorithm is called the electron author. For the CC channel both electrons have to be "central". This means that both electron candidates have to be processed by the standard eGamma reconstruction algorithm. In the CF channel one electron also has to be found by the central author while the other electron in the pair has to be processed by the author providing the EM object reconstruction in the forward calorimeters. Details on the electron authors are introduced in Sec. 5.2.

6. The next selection requirement restricts the detector acceptance in η_e. With these cuts it is ensured that the shower of the electron candidates are well contained in the calorimeters with respect to the boundaries in η_e. This is necessary to have properly defined electron shower shapes for the *EM-id*. Here the electron candidates are required to be within $|\eta_e| < 2.47$ in case of a central electron and within $2.5 < |\eta_e| < 4.9$ in case of a forward electron. Further the transition regions at $1.37 < |\eta_e| < 1.52$ and $3.16 < |\eta_e| < 3.35$ are excluded from the selection.

7. Selection requirement seven is asking for a minimum transverse energy of the electron candidates. This cut is introduced at $\mathrm{p_T} > 25$ GeV slightly above the trigger threshold. The difference between trigger and selection threshold is introduced to assure that the trigger efficiency is already on its plateau. Independent of the fact that the trigger only accounts for central electrons, all electrons have to fulfill the same selection threshold. This is introduced to have good control of the electron identification that suffers from larger background contributions due to jet like objects in the detector at lower transverse momenta.

8. The object quality check is rejecting electrons that are located too close to defunct calorimeter cells. The issues are mostly related to the regions with faulty FEBs in the EM-barrel region as introduced above.

9. As last cut in this selection the identification requirements are applied. In the CC channel both electrons have to pass the *medium++ EM-id*. Additionally the electrons have to have opposite charges. In the CF channel the central electron has to fulfill the *tight++ EM-id* and needs to be isolated to suppress more background candidates from jet fakes. The forward electron has to be at least *forward-medium*. Because there is no charge measurement in the forward region, the opposite charge cut has to be omitted. Details on the definitions of the different *EM-id*s can be found in Sec. 5.3.1 and Sec. 5.3.2.

		Data		
Cut Number	**Cut**	**Number of Events** [10^6]	**Rel. selection rate [%]**	**Abs. selection rate [%]**
1	Good Run List	86.072	100.0	100.0
2	tracks at vertex	85.812	99.7	99.7
3	trigger	4.858	5.66	5.64
4	2 electrons	4.858	100.0	5.64
5	author	4.807	99.0	5.59
6	$\|\eta\|$ (and crack)	4.463	92.8	5.19
7	p_T	2.637	59.1	3.06
8	OQ	2.610	99.0	3.03
9	*medium++*	1.255	48.1	1.46
	opposite charge	1.229	97.9	1.43

Table 6.1.: Number of events in data, surviving the cuts for the electron CC analysis. The cuts are described in more detail in Sec. 6.2.

		Data		
Cut Number	**Cut**	**Number of Events** [10^6]	**Rel. selection rate [%]**	**Abs. selection rate [%]**
1	Good Run List	86.072	100.0	100.0
2	tracks at vertex	85.812	99.7	99.7
3	trigger	37.689	43.9	43.8
4	2 electrons	37.689	100.0	43.8
5	author	29.055	77.1	33.8
6	$\|\eta\|$	27.885	96.0	32.4
7	p_T	4.371	15.7	5.08
8	OQ	4.337	99.2	5.04
9	*EM-id*	0.359	8.28	0.42

Table 6.2.: Number of events in data, surviving the cuts for the CF electron analysis. The requirement *EM-id* refers to the combination of *tight++* w/ calorimeter based isolation in the central region, and *forward-medium* in the forward region. The cuts are described in more detail in Sec. 6.2

Tab. 6.1 to Tab. 6.4 list the cut-flows for the event selection on reconstructed properties of the data and signal Monte Carlo. After the GRL requirement he integrated luminosity of data contains about $4.8\,\text{fb}^{-1}$.

The samples these requirements are applied on are the recorded data and the signal as well as the back-

Monte Carlo Signal				
Cut Number	**Cut**	**Number of Events [10^6]**	**Rel. selection rate [%]**	**Abs. selection rate [%]**
	all events	39.940	—	—
2	tracks at vertex	39.935	100.0	100.0
3	trigger	17.117	42.9	42.9
4	2 electrons	16.961	99.1	42.5
5	author	16.719	98.6	41.9
6	$\|\eta\|$ (and crack)	15.787	94.4	39.5
7	p_T	13.340	84.5	33.4
8	OQ	13.208	99.0	33.1
9	*medium++*	10.296	78.0	25.8
	opposite charge	10.074	97.8	25.2

Table 6.3.: Number of events which pass the selection in the Monte Carlo signal sample in the electron CC analysis. The cuts are described in more details in Sec. 6.2.

Monte Carlo Signal				
Cut Number	**Cut**	**Number of Events [10^6]**	**Rel. selection rate [%]**	**Abs. selection rate [%]**
	all events	39.940	—	—
2	tracks at vertex	39.935	100.0	100.0
3	trigger	27.687	69.3	69.3
4	2 electrons	27.115	97.9	67.9
5	author	17.480	64.5	43.8
6	$\|\eta\|$ (and crack)	17.097	97.8	42.8
7	p_T	4.073	23.8	10.2
8	OQ	4.050	99.4	10.1
9	*EM-id*	2.449	60.5	6.1
	isolation	2.442	99.7	6.1

Table 6.4.: Number of events which pass the selection in the Monte Carlo signal sample in the electron CF analysis. The requirement *EM-id* refers to the combination of *tight++* w/ calorimeter based isolation in the central region, and *forward-medium* in the forward region. The cuts are described in more detail in Sec. 6.2

ground Monte Carlo sets as defined in Tab. 4.2. The background MCs consist of samples with contributions from two or more real electrons, like Diboson samples or dileptonic $t\bar{t}$ events. Also there are contributions from processes that contain one real electron and at least one jet that passes the electron identification and fakes a signal. There are e.g. the production of $W \to e\nu$, $W \to \tau\nu$ or $Z \to \tau\tau$, where real electrons and jets are produced. These samples are discussed in detail in Sec. 8.1. As last contribution there are the events from pure multijet processed. The events where misidentified jets fake the electron identification can not sufficiently be produced in simulation and have to be estimated from data. There are different ways to treat the fake contributions from jets which have implications on the set of Monte Carlo backgrounds taken into account. These methods are discussed in Sec. 8.2 separately for the CC and CF channel.

6.3. Selection efficiency study on signal Monte Carlo events within phase space restrictions

When studying the signal yield of the selection it is a good idea to not compare the selection on the full set of signal events but to restrict the phase space of the signal sample to the events that are expected to be accessible in the respective channel selections. With this it is common to preselect the events the analysis is performed on by requiring the additional cuts on generator level. Here the acceptance of the selection channel can be defined on the truth electron pair. This pair is built from the pair of electrons that originates from the hard process on generator level. By building the ratio of events in which the truth electron pair passes a phase space selection close to the one applied on reconstruction level over all events in the sample, the channel acceptance can be obtained. The two channels studied in this analysis have acceptances of 45.4% in the CC channel and 15.9% in the CF channel.

To further study the impact of the selection on the restricted phase space it is common to perform a matching of the reconstructed electron candidates to the true electrons. With this all selection cuts that are defined on reconstructed quantities can be evaluated for the pair of true electrons. With the number of events passing the sequential selection requirements signal selection efficiencies can be obtained.

In this study no matching is performed. Instead only the acceptance criteria are applied in the selection. The respective selection efficiencies are therefore no accurate measure for the probability of a generated electron pair to pass the full selection. It is the rate of events that have a generated electron pair in the appropriate phase space to also fulfill the selection criteria after reconstruction and identification of the related objects.

Monte Carlo Signal					
Cut Number	**Cut**	**Number of Events [10^6]**	**Rel. efficiency [%]**	**Abs. eff. w.r.t. acceptance [%]**	**Abs. efficiency w.r.t. all [%]**
	all events	39.940	—	—	—
	acceptance passed	18.133	45.4	100.0	45.4
2	tracks at vertex	18.132	100.0	100.0	45.4
3	trigger	15.748	86.9	86.8	39.4
4	2 electrons	15.607	99.1	86.1	39.1
5	author	15.394	98.6	84.9	38.5
6	$\|\eta\|$ (and crack)	14.506	92.4	80.0	36.3
7	p_T	13.175	90.8	72.7	33.0
8	OQ	13.045	99.0	71.9	32.7
9	*medium++*	10.218	78.3	56.4	25.6
	opposite charge	10.001	97.9	55.2	25.0

Table 6.5.: Number of events which pass the selection in the Monte Carlo signal sample in the electron CC analysis. The cuts are described in more details in Sec. 6.2.

Monte Carlo Signal					
Cut Number	**Cut**	**Number of Events [10^6]**	**Rel. efficiency [%]**	**Abs. eff. w.r.t. acceptance [%]**	**Abs. efficiency w.r.t. all [%]**
	all events	39.940	—	—	—
	acceptance passed	6.334	15.9	100.0	15.9
2	tracks at vertex	6.332	100.0	100.0	15.9
3	trigger	4.850	76.6	76.6	12.1
4	2 electrons	4.825	99.5	76.2	12.1
5	author	4.780	99.1	75.5	12.0
6	$\|\eta\|$ (and crack)	4.572	95.6	72.2	11.4
7	p_T	3.877	84.8	61.2	9.7
8	OQ	3.854	99.4	60.9	9.7
9	*EM-id*	2.455	63.7	38.8	6.1
	isolation	2.448	99.7	38.7	6.1

Table 6.6.: Number of events which pass the selection in the Monte Carlo signal sample in the electron CF analysis. The requirement *EM-id* refers to the combination of *tight++* w/ calorimeter based isolation in the central region, and *forward-medium* in the forward region. The cuts are described in more detail in Sec. 6.2

7. Determination of energy scales on forward electrons

In this section the energy calibration of electron pairs including one forward electron is described. Sec. 7.1 explains the basic setup with the event selection and the background contributions, whereas Sec. 7.2 discusses the underlying theoretical model for the calculation of the scaling constants for data energy scale and Monte Carlo resolution correction. In Sec. 7.3 the evaluation of systematic uncertainties is derived and Sec. 7.4 closes with a summary and the results of this study.

The calorimeters used to measure the energy depositions of electrons as described in Sec. 3.2.4.1 and Sec. 3.2.4.3 are initially calibrated using the energy response from test beam measurements as well as measurements and calibrations in previous data taking runs. These calibrations are derived on other data sets that were collected with partly different conditions. The calibrations from test beam data are derived on prototype segments of the calorimeters that were installed in a generic testing environment. In this setup the test beams used were driven by high energetic electron and pion sources and the calorimeters were moved into the beam to test their performance and to derive the energy calibrations. The calorimeters installed in ATLAS that are used for this study are arranged to cover a specific part of the detector acceptance. The particles reaching these segments, have passed a specific pattern of material in front of the calorimeters, that has not been exactly reproducible in the test beams. Therefor the initial calibration only works as a starting point for a well defined energy measurement.

The calibrations taken from previous data sets collected in collision data in ATLAS on the other hand differ from the current setup e.g. in the instantaneous luminosity, the bunch spacing setup in the collider and the pile-up event distribution. Also the composition of particle content traveling through the detector at given positions in rapidity doesn't need to be the same as in previous estimates. To assure proper calibration to the actual setup, the calibration is derived specifically on the data set that is used in current analyses.

In this sample of measured data, the event selection has to enrich the rate of events that have certain signatures to make a calibration possible. To calibrate the energies of electrons the process of $Z/\gamma^* \rightarrow e^+e^-$, the electroweak exchange particle in the neutral current decaying into two electrons, is used. To discriminate events that originate from background processes with respect to the contributions of this signal process, these electrons have to fulfill identification requirements as described in Sec. 5.3.

The signal MC used here is the same as defined in Sec. 4.3.1, using PYTHIA as event generator.As the energy calibration study is performed earlier in time as the other discussed studies, the available statistics of the signal MC sample only was about 9.1 M events.

The data set corresponds to a data set luminosity of about $11\,\mathrm{fb}^{-1}$ using the LO process cross section.

The data events are the same as used in Sec. 6.2 for the CF channel. The integrated luminosity after the application of the GRL corresponds to about $4.8\,\mathrm{fb}^{-1}$.

The range in electron rapidity investigated in this calibration only contains bins in the forward region. It includes 6 bins in each EMEC, three bins in the FCals each and a defined transition region between the two end cap compartments each, referred to as the crack region. This corresponds to the binning that is chosen in the definition of the identification requirements for the forward electrons. These bins are listed in Tab. 7.1 and are used in the energy resolution correction on Monte Carlo as well as in data energy scale corrections. The binning was chosen to be larger than size of the shower core.

$\|\eta\|$ range	Size ($\Delta\eta$)
[2.50, 2.60]	0.10
[2.60, 2.70]	0.10
[2.70, 2.80]	0.10
[2.80, 2.90]	0.10
[2.90, 3.00]	0.10
[3.00, 3.16]	0.16
(crack) [3.16, 3.35]	0.19
[3.35, 3.60]	0.25
[3.60, 4.00]	0.40
[4.00, 4.90]	0.90

Table 7.1.: Bin definition as a function of η for the forward regions.

This calibration is used to shift the measured data energy response towards the values obtained from the signal Monte Carlo after detector simulation and particle reconstruction. It is taking into account identification requirements that are very close to the ones used in the physics analyses the calibration is needed for. The resolution parameters are also determined on the same data sets and are used to broaden the Monte Carlo resolution of reconstructed and identified simulation events to the distribution obtained in data using the same requirements.

These calibrations explicitly are not meant to calibrate energy scale and resolutions to values known at generator level. They are meant to inter-calibrate the response in data to the full detector simulation.

7.1. Assumptions and basic setup

For this study on the calibration of the energy measurement for electrons in the forward region, events are used that contain a well identified pair of electrons. In these pairs one electron is depositing its energy in the central detector acceptance while the other one is going forward. To only determine scales for the forward electrons, this study relies on the previously calibrated central electrons [63, 64] which is shown to work well within a small band of systematic uncertainties. To take the uncertainty of the energy calibration of the central electrons into account, the derived errors on the calibration parameters are propagated to the uncertainties of the calibration constants in this study. The treatment of the systematic uncertainties is discussed in Sec. 7.3.

7.1.1. Event selection

The event selection performed for this study is based on the selection for the CF channel as described in Sec. 6.2. The only difference with respect to the applied list of requirements is the omission of the isolation requirement on the central electron. This was chosen not to be used, as there is no standardized definition of an isolation in the recommendations of the performance studies done within the eGamma.

Tab. 7.2 and Tab. 7.3 list the cut-flows for the event selection on data and the signal Monte Carlo.

Description	Events
GRL	86.9 M
track at vertex	86.7 M
trigger	38.0 M
2 electrons	38.0 M
author	29.3 M
$\|\eta\|$	28.1 M
p_T	4.41 M
OQ	4.38 M
EM-id	0.372 M

Table 7.2.: Number of events in data, surviving the cuts for the the energy scale study. The requirement *EM-id* refers to the combination of *tight*++ w/ calorimeter based isolation in the central region, and *forward-medium* in the forward region. The cuts are described in more detail in Sec. 6.2

Description	Events
Pile-up	9.14 M
track at vertex	9.14 M
trigger	6.30 M
2 electrons	6.22 M
author	4.00 M
$\|\eta\|$	4.00 M
p_T	0.926 M
OQ	0.921 M
EM-id	0.565 M

Table 7.3.: Number of events which pass the selection in the Monte Carlo signal sample in the the energy scale study. The requirement *EM-id* refers to the combination of *tight*++ w/ calorimeter based isolation in the central region, and *forward-medium* in the forward region. The cuts are described in more detail in Sec. 6.2

7.2. Calibration of forward electron energies

As described in Sec. 7.1 this calibration study is setup to calculate the energy scaling parameters for forward electrons with a rapidity of $2.5 < |\eta_e| < 4.9$ based on a precalibrated central part of the detector acceptance. Therefore the calibration of each bin in forward electron rapidity can be seen as disjoint calibration and no further combinatorial estimate between these bins has to be calculated to derive these scaling parameters.

7.2.1. Data Energy scale

Starting from basic relations of the invariant mass of two measured energy depositions E_1 and E_2 and a given opening angle θ_{12}

$$m = \sqrt{2E_1E_2(1 - \cos(\theta_{12}))}, \tag{7.1}$$

the energies E_1 and E_2 can be identified with the energies of the central and the forward electron respectively. In general the energy scale derived to correct the energy measure in data is defined as

$$E^{meas} = E^{true} \cdot (1 + \alpha_i), \tag{7.2}$$

where α_i is the calibration constant to shift the energy measured in data E^{meas} to the mean value estimated from Monte Carlo E^{true}. All energy and mass values, also the ones denoted by Monte Carlo or *true*, are derived from the reconstructed quantities.

When combining (7.1) and (7.2) one can derive relations for m being a measure of data or MC invariant mass peak position, such that the resulting calibration constant α_i can be extracted:

$$m_{data} = \sqrt{2E_1^{meas}E_2^{meas}(1-\cos(\theta_{12}))}, \tag{7.3}$$

Here the indices 1 and 2 denote the central and forward electron so that $E_1^{meas}|_{data}$ can be set to $E_1^{true}|_{data}$, because the electrons in the central acceptance are already calibrated to best knowledge.

$$m_{data} = \sqrt{2E_1^{true}E_2^{true}(1+\alpha_i)(1-\cos(\theta_{12}))}, \tag{7.4}$$

$$m_{MC} = \sqrt{2E_1^{true}E_2^{true}(1-\cos(\theta_{12}))}, \tag{7.5}$$

$$\frac{m_{data}^2}{m_{MC}^2} = \frac{(1+\alpha_i)}{1}\frac{2E_1^{true}E_2^{true}(1-\cos(\theta_{12}))}{2E_1^{true}E_2^{true}(1-\cos(\theta_{12}))}, \tag{7.6}$$

$$\alpha_i = \frac{m_{data}^2}{m_{MC}^2} - 1. \tag{7.7}$$

The calibration constant α_i results to just be depending on the squares of the peak positions of the reconstructed resonances in Monte Carlo and data.

7.2.2. Monte Carlo Energy Resolution

Next to the calibration of the data energy scale also the resolution in Monte Carlo needs to be calibrated when comparing data to MC. To express the difference of the Monte Carlo resolution to the resolution measured in data, the definition of terms contributing to the resolution in general have to be discussed first.

The resolution of a sampling calorimeter consists of three terms.

$$\left(\frac{\sigma_E}{E}\right)_{MC} = \frac{a}{\sqrt{E}} \oplus \frac{b}{E} \oplus c \tag{7.8}$$

The sampling term a is proportional to $\sqrt{E}$ and has to be well modeled by the simulation. The noise term b used in the simulation is taken from calibration runs, so that any additional resolution correction is assumed to be proportional to the energy.

$$\sigma_{corr} = \sigma_{MC} \oplus c_{data} \cdot E \tag{7.9}$$

In general this constant term is now to be measured in data and MC and calculated for each combination of bins in rapidity of the first and second electron denoted by the indices i and j.

By performing Gaussian error propagation to (7.1) and building partial derivatives as in

$$\frac{\partial m}{\partial E_1} = \frac{1}{2m} \cdot 2E_2(1 - cos\theta) = \frac{1}{2m} \cdot \frac{m^2}{E_1} = \frac{m}{2E_1} = \frac{\sigma_m}{\sigma_{E_1}} \tag{7.10}$$

$$\frac{\partial m}{\partial E_2} = \frac{1}{2m} \cdot 2E_1(1 - cos\theta) = \frac{1}{2m} \cdot \frac{m^2}{E_2} = \frac{m}{2E_2} = \frac{\sigma_m}{\sigma_{E_2}} \tag{7.11}$$

one can identify the uncertainties with the resolution σ_X. With this one can obtain

$$4\left(\frac{\sigma_m}{m}\right)^2 = \left(\frac{\sigma_{E_1}}{E_1}\right)^2 + \left(\frac{\sigma_{E_2}}{E_2}\right)^2. \tag{7.12}$$

When adding an extra constant term $\left(\left(\frac{\sigma_E}{E}\right)^2 \Rightarrow \left(\frac{\sigma_E}{E}\right)^2 + c^2_{data}\right)$ and comparing Data to MC one gets

$$4\left(\frac{\sigma_m}{m}\right)^2_{ij,data} = 4\left(\frac{\sigma_m}{m}\right)^2_{ij,MC} + c_i^2 + c_j^2. \tag{7.13}$$

In the general case where both electrons are to be resolution corrected, this results in

$$c_{ij}^2 = 2\left[\left(\frac{\sigma_m}{m}\right)^2_{ij,data} - \left(\frac{\sigma_m}{m}\right)^2_{ij,MC}\right]. \tag{7.14}$$

In this general case the constant terms can only be directly accessed for electron pairs ij. The combined term for a pair in i and j can then be translated into the individual values for this constant for the two electrons in their corresponding bins with

$$2c_{ij}^2 = c_i^2 + c_j^2. \tag{7.15}$$

In this case a system of equations has to be solved to extract the individual resolution correction constants. This has been done to derive the constant terms for the central electron resolution calibration.

Adapting the above equations to the setup that the scales are to be derived for the forward electrons only, this pair of electrons only consists of one electron that is uncalibrated and the other one that is already fully calibrated. To calculate the constant term in this setup, (7.13) can be reduced to

$$c_j^2 = 4\left[\left(\frac{\sigma_m}{m}\right)^2_{j,data} - \left(\frac{\sigma_m}{m}\right)^2_{j,MC}\right]. \tag{7.16}$$

These calibration constants can further be derived independently for all bins in rapidity of the forward electron, as it is done for the data energy scales.

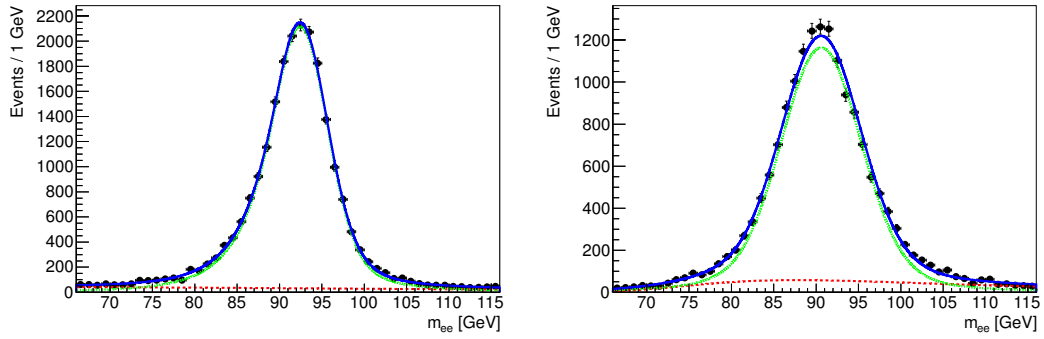

(a) (b)

Figure 7.1.: Examples of fits to the BreitWigner ⊗ CrystalBall in the EMEC region (left) and FCal region (right) on data distributions. The χ^2/ndof of the fit is 1.17 in the EMEC and 1.64 in the FCal.

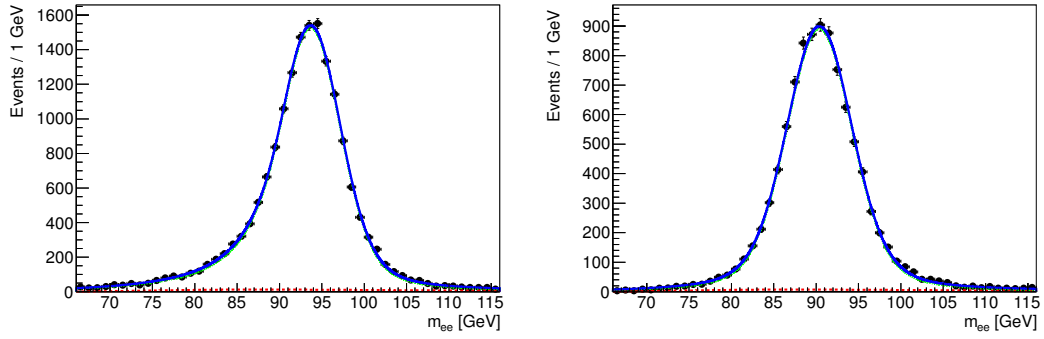

(a) (b)

Figure 7.2.: Examples of fits to the BreitWigner ⊗ CrystalBall in the EMEC region (left) and FCal region (right) on MC distributions. The χ^2/ndof of the fit is 1.48 in the EMEC and 2.71 in the FCal.

7.2.3. Extraction of calibration constants

To gather the calibration constants, analytical fits are used to model the line shape of the invariant mass spectrum in data and Monte Carlo. These fits consist of a signal contribution and a background contribution. The signal has to describe the expected Drell-Yan line shape and the $Z/\gamma^* \rightarrow ee$ resonance whereas the background is estimated to contain the effect of combinatorial pairs of electrons or electron fakes from ℓ+jets or multijet processes for example. The signal line shape is approximated with a convolution of a Crystal Ball function and a Breit Wigner resonance while the background is assumed to follow a Landau distribution. The Crystal Ball function is used to estimate the radiative effect from bremsstrahlung that is a priori undetermined. It is defined to behave like a Gaussian distribution at its most probable value but consist of a power law function towards its low-end tail. To fit these functions to the distributions from data and Monte Carlo the RooFit [66] toolkit is used. RooFit is a package that includes fitting and minimization routines to analytically extract functional parameters of input functions from an input data set.

In these fits the parameters for the width of the Breit Wigner resonance is fixed to the width of the Z

resonance taken from the PDG[1] [32], with a value of $\Gamma_Z = 2.49\,\text{GeV}$. The peak mass parameter of the Crystal Ball function in the convolution for the signal line shape is set to $\bar{x} = 0$. The two parameters taken from the fit are the invariant mass m of the Breit Wigner resonance and the width σ of the gaussian part of the Crystal Ball function.

To extract the values for the data energy scale parameter α_i the fits are run once on data and Monte Carlo using calibrated central electrons as described and raw electron energies from the corresponding forward rapidity bins after the mentioned selection criteria. The energy scale constants derived by applying (7.7) are the nominal results of the data energy calibration.

To derive the calibration parameters of the resolution correction, the new scale parameters α_i are used to calibrate the forward electrons on data. As a next step a second iteration of fits is performed comparing the now calibrated set from data with the same set of uncalibrated forward electrons from Monte Carlo as before. With this combination the calibration constants for the resolution correction c_i are calculated from (7.16). This is necessary, because the resolution correction depends on a proper energy scale calibration.

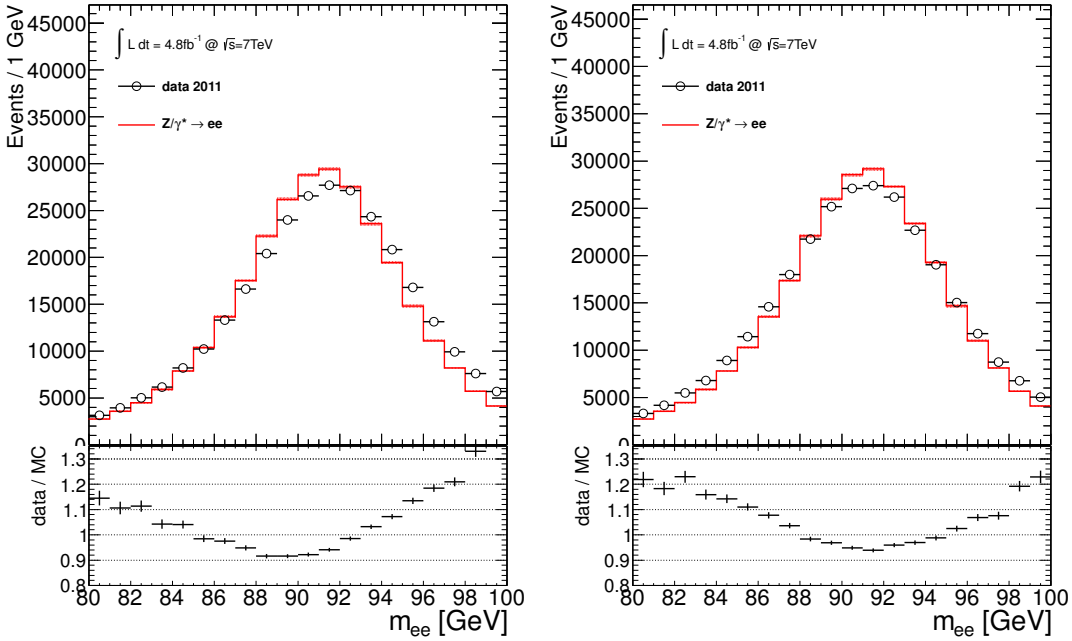

(a) (b)

Figure 7.3.: Invariant mass of di-electron system with no energy scales on the forward electrons on the left and on the right using only the derived energy scales without energy smearing. This demonstrates the need for additional MC energy smearing. The lower figures show data to MC ratio including statistical uncertainties for each corresponding bin.

The derived central values and statistical or fit uncertainties from this study can be found in Fig. 7.5 of Sec. 7.3. An example of the fits performed in RooFit on data can be seen in Fig. 7.1 for the EMEC and FCal regions. The corresponding fits on MC are shown in Fig. 7.2. The compatibility of the kinematic properties of the data and MC samples used in this study and the effect of the calibrations are shown in

[1]The particle data group (PDG) publishes biennial reviews of measurements in particle physics and lists, evaluates and averages measured properties of and limits on constituents of the SM and beyond [32].

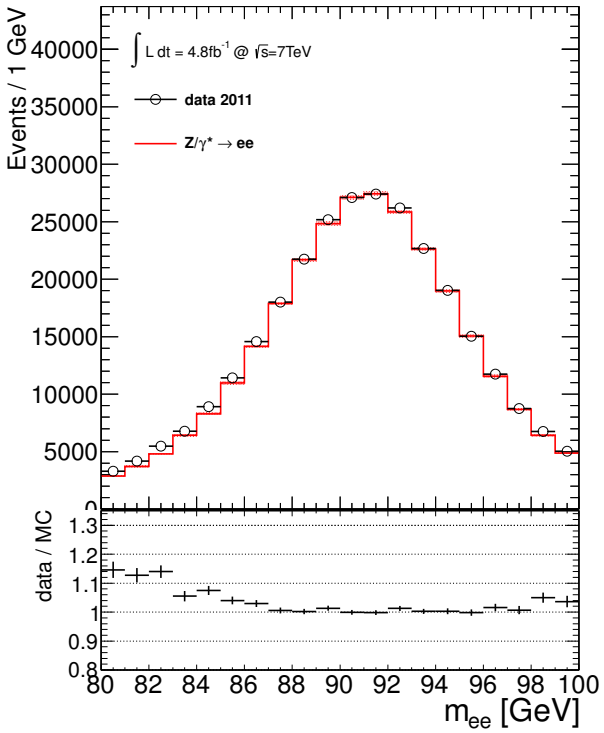

Figure 7.4.: The upper figure gives a data to MC comparison including both smearing on the MC and scaling on the data. The lower figure shows data to MC ratio including statistical uncertainties for each corresponding bin. A good closure can be seen below the resonance and at the high energy tail. The deviation at the low end is a result of the backgrounds no that are not included in the MC histogram.

Fig. 7.3 and Fig. 7.4. These figures show the invariant mass distribution before and after the calibration steps.

7.3. Systematics

For the evaluation of systematic uncertainties on the extracted calibration constants, variations on the fitting procedure as well as the underlying data and Monte Carlo corrections and calibrations are performed.

The variations on the input samples consist of:

- the variations of the fit stability derived from varying the fit range window:
  $(66 < m_{\ell\ell}/\text{GeV} < 116)$ default
  $(75 < m_{\ell\ell}/\text{GeV} < 105)$ smaller
  $(60 < m_{\ell\ell}/\text{GeV} < 130)$ larger

- the variation of the background fit function:
  landau function (in $66 < m_{\ell\ell}/\text{GeV} < 116$) default
  exponential (in $70 < m_{\ell\ell}/\text{GeV} < 130$) variation

- the variations of the central electron energy scale and resolution within all provided uncertainties: The variations of all provided sources of statistic and systematic uncertainties are performed separately and the resulting shifts of the extracted calibration constants are summed quadratically. This isthe recommended procedure for the propagation of the central electron energy calibration uncertainties.

- a subdivided set of conditions of pile-up events parametrized in the number of reconstructed primary vertices N_{PV}:
  low $1 \leq N_{PV} < 5$
  medium $5 \leq N_{PV} < 8$
  high $8 \leq N_{PV}$

- the remaining difference of the closure test is added for resolution correction only

The variations of pile-up, fit stability and the mis-closure on Monte Carlo are bin-by-bin uncorrelated in forward electron rapidity since the input samples are disjoint. The variations of the central electron energy scale and resolution are bin-by-bin correlated as the same variation influences all bins in forward rapidity in a similar manner depending on the kinematic correlations. The overall uncertainties of the extractions are summarized in Fig. 7.5. The details of the resulting calibration constants and their uncertainties are shown in App. C. There Tab. C.1 summarizes the central estimates and the corresponding uncertainties where as the impact of the individual variations can be looked up in the tables Tabs. C.2 and C.3. The largest contributions to the systematic uncertainties of the energy scale constants α_i are introduced in the variation of pile-up conditions. The second largest contributions are the propagated uncertainties of the central electron energy scale. The systematic uncertainties on the resolution constants are not dominated by a single source. The larger contributions are again introduced by the variation in pile-up conditions and central electron resolution uncertainty but also by the closure test.

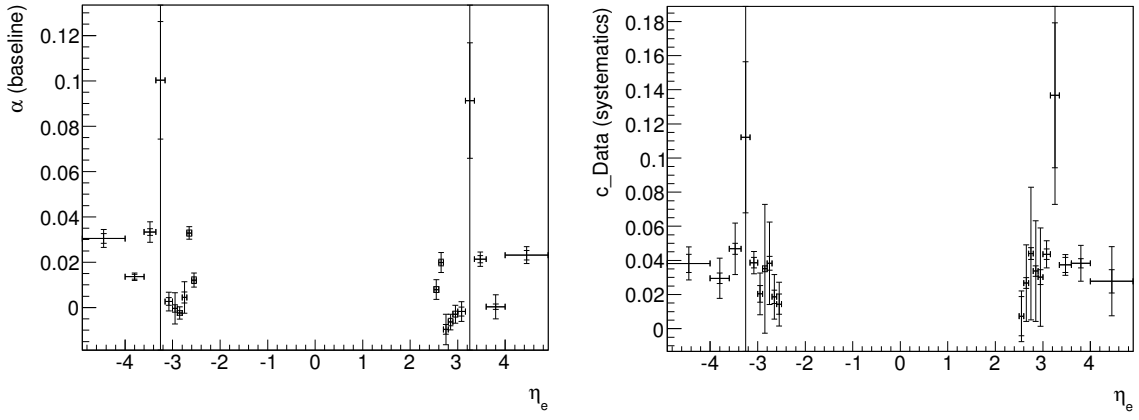

(a) (b)

Figure 7.5.: In the left figure the energy scale parameter α is shown, where as in the right figure the resolution correction parameter is shown. In both distributions the statistical and systematical uncertainties are included. A detailed table of he uncertainties broken up in the contributing sources, is included in App. C.

7.4. Results

In the above section the initial study to derive calibration constants for forward electron energy scales and resolution correction on the 2011 data set has been described. It has been shown, that with the approach of a precalibrated central detector, the calibration constants for forward electron energy corrections can be extracted bin-by-bin uncorrelated in electron rapidity. Further the estimates give a fairly inclusive uncertainty envelope.

As this study is not a continuation of a previous calibration study, the method used to derive the calibration has had its initial tests within this study. The motivation to re-derive the electron energy calibration for forward electrons was given by the need of a properly calibrated energy measurement in the Z-boson forward backward asymmetry measurement which is the main topic of this thesis. Therefore the basic requirements for the calibration study were to derive a stable and reliable set of calibration constants that have a well motivated set of systematic uncertainties taken into account. It was meant to be usable for the only customer analysis at that time. Currently also other analyses make use of this calibration while a derived approach of the chosen calibration setup on the 2012 data set has also been performed.

This calibrations and the methods used within were introduced tested and used for this study, but there has not been time for a detailed reevaluation of possible methodological improvement to this kind of calibration on the same data set yet. On the other hand it has been tested that there are ways to improve the stability of the underlying fit routines that are used in the continuation of this study on the data set of the following year 2012. The detailed comparison of the two studies is not as straight forward as it seems. There are improvements studied to stabilize the fits by varying the input parameters of the fits $O(1000)$ times and choosing the fit with the minimal value of χ^2 for further use in the calculation. Further there are ways to include details of the distortion in the line shape of the invariant-mass distribution due to kinematic acceptance requirements. These kinematic turn-on could be included into the fit functions to gain a better description of data and Monte Carlo by the fits. Also the available statistics has increased by a factor 4 in 2012 with respect to the 2011 data taking and direct improvements in the statistics uncertainties in the fit are expected. As a final gain the variation with respect to the pile-up conditions is not taken into account any more. The fact that the calibration is not used on a subset of the collected data in any analysis allows to neglect these implied systematics.

These points have taken quite a lot of time and testing to be implemented and functional for the 2012 study and are in principle also applicable for the 2011 data set. The expected gain on the resulting "level of trust" in this calibration has to be related to the fact that in the 2012 measurement a different set of Monte Carlo generators has been used and that the resulting systematic uncertainties in terms of the resolution correction are on the same order of magnitude despite the improvements.
Taking a closer look at the variations quoted in Tab. C.1, C.2 and C.3 the band of systematic uncertainties could be slightly reduced by neglecting the contributions of the variation in pile-up conditions and reinterpretation of fits in variations that seem to be off. The coverage of the data - MC differences in the line shape even seems to be satisfactory if the systematics of e.g. the energy smearing are manually reduced. This interpretation on the other hand has not been done as a new study but as a comparison of the application of the official systematic uncertainties and a set of reduced systematics where deviations in the variation inputs from less optimal fits have been replaced by the deviations in mirroring bins in $|\eta|$.

Concluding the above mentioned features and perspectives the described study of the 2011 forward energy calibration gives a competitive picture, taking into account the simplicity and implication of its approach.

8. Background estimates and data - Monte Carlo comparison

In this section important background processes to the measurement of $Z/\gamma^* \rightarrow ee$ are introduced. There are the processes, that can be estimated by a dedicated background Monte Carlo, while other processes can only sufficiently well being estimated by data driven techniques. On the background Monte Carlo samples the event selection defined in Sec. 6.2 can be applied, where as the processes containing fake contributions from misidentified jets have to be estimated from data with specialised methods and selections. The samples containing the MC backgrounds are introduced in Sec. 8.1, while different approaches to describe the contributions from multijet events are defined in Sec. 8.2.

In the last section a comparison of data to all introduced signal and background processes is shown. This comparison includes the corrections to data and Monte Carlo that were defined in Sec. 6.1.

8.1. Background Monte Carlo processes

The background contributions from Monte Carlo samples mainly contain processes that produce electroweak gauge bosons in the hard process or as the imminent decay product of that. These processes are important to study as reducible and irreducible contributions to the background, as they contain electrons in their decay chains. There are the signatures of $t\bar{t}$ events with electrons in the final state of the two W bosons, the t quarks radiate off when decaying into b quarks, before they can hadronise. Then there are processes in which two electroweak gauge bosons are produced, which can decay into final states that contain up to four electrons. And finally there are the processes, where the W bosons can decay into the electron final state. Of course the Z and W boson can also decay into final states with τ leptons. In these processes the τs can on their side decay into electrons or into light hadrons.

The signatures that contain at least two real electrons in their respective decay chains are categorised as irreducible backgrounds, while the processes that contain at most one real electron in their respective decay chains, are categorised as reducible backgrounds as at least one jet has to be mis-identified as a good electron to pass the signal selection.

8.2. Background estimate on multijet events

To estimate the amount of background in the selection on data, that originates from multijet processes, data driven estimates are used. These estimates are required to contain low amount of signal events but an enriched number of background events. The selections rely on the loosening or inversion of certain identification criteria of the original signal selection.

Methods to adapt these special background enriched selections to get a handle on the contamination of backgrounds in the signal selection are e.g. the reverse ID template method and the fake factor or matrix method.

8.2.1. Reverse ID template method

The reverse ID template method uses a selection, that inverts certain identification cuts. This selection is applied on all input MC and is then subtracted from data, using the inverted requirements. This avoids double counting of contributions already taken into account by Monte Carlo background samples.

After subtraction the set of events collected with the inverted selection has to be scaled to match the expected background yield in the default selection on data. This scaling is necessary, because the rate of events passing the inverted selection can be arbitrarily different from the rate of the background events in the signal selection on data, which it is expected to estimate. To assess this scaling factor a fractional fit can be performed using e.g. the invariant mass distribution around the Z/γ^* resonance. Leaving the allowed fraction of the integral of all Monte Carlo and the integral of the multijet template floating in this fit gives the most probable value for this global multijet scale factor. It is expected to result a scale factor for the Monte Carlo only slightly deviating from 1.0 and scale factor for the multijet template reflecting the different selection efficiencies in the signal selection and the orthogonal template selection.

For the CC channel the electron candidate pairs are required to fulfill the full signal selection except the identification requirement. Instead the pairs are required to consist of one electron passing the *loose++* selection but failing the *medium++ EM-id* and the other one to fail a cut on the calorimeter strip requirement of the *loose++* identification [63].

In the CF selection the central electron required is to pass the *medium++* but fail the *tight++ EM-id* without checking the isolation requirement used in the default selection. The forward electron has to pass *forward-loose* and fail *forward-medium EM-id* at the same time. As a variation to estimate systematic differences in the distribution of multijet events especially at higher masses, an additional template with an inverted cut on the central electron isolation requirement is studied. The details of this variation are discussed together with the systematic variations on the backgrounds in Sec. 9.3.3.

8.2.2. Fake factor method

In the CC channel the reverse ID template method is known to underestimate the contribution of multijet background at high invariant masses [67]. Additionally the statistics of the $W \rightarrow e\nu$ background MC is known to only yield reliable precision up to $m_{ee} \approx 300\,\text{GeV}$. As an alternative method that was tested to overcome these issues, a fake factor or matrix method [67] is used. On the other hand this method is not usable in regions with a very high signal contribution and has therefore only been used for events more than 15 GeV above the Z/γ^* resonance in m_{ee} in earlier analyses.

In the fake factor method two types of electron identifications loose (L) and tight (T) are required similar to the reverse ID method. The loose electrons are required to pass *loose++* selection while *medium++* criteria are failed. The tight electrons have to pass *medium++* criteria as in the signal selection. Except for the ID selection criteria in the loose and tight subselections, all requirements from the signal selection are kept.

8.2.2.1. Fake Factor Formalism

The fake factor method or matrix method connects the knowledge about the efficiency of electrons from signal and background control regions. These regions are defined in terms of real and fake electron subsamples. These subsamples have to pass a set of loose (L) and tight (T) *EM-id* selections. The method uses a transition matrix to account for the contribution of real and fake electrons from the control regions to loose and tight electron selections on the full data set. This transition matrix is defined upon the following parameters:
Electron pairs on the full data set are grouped in categories of the combinations N_{xy} with $x, y \in T, L$. Using (8.1) these candidates relate to "true" quantities which are named N_{ab} with $a, b \in R, F$. Here the selections N_{xy} and N_{ab} are comprised by the combinations of x, y and a, b respectively. The selection N_{LL} only contains pairs of electron candidates that are both loose and not tight. This way the corresponding electron pairs selections are disjoint.

$$\begin{pmatrix} N_{TT} \\ N_{TL} \\ N_{LT} \\ N_{LL} \end{pmatrix} = \begin{pmatrix} r_1 r_2 & r_1 f_2 & f_1 r_2 & f_1 f_2 \\ r_1(1-r_2) & r_1(1-f_2) & f_1(1-r_2) & f_1(1-f_2) \\ (1-r_1)r_2 & (1-r_1)r_2 & (1-f_1)r_2 & (1-f_1)f_2 \\ (1-r_1)(1-r_2) & (1-r_1)(1-f_2) & (1-f_1)(1-r_2) & (1-f_1)(1-f_2) \end{pmatrix} \begin{pmatrix} N_{RR} \\ N_{RF} \\ N_{FR} \\ N_{FF} \end{pmatrix} \tag{8.1}$$

The "true" quantities consist of "real" (R) and "fake" (F) electrons. The "real" electrons are determined from signal Monte Carlo, whereas the "fake" electrons are estimated from multijet background enriched selection on data. The fake contributions, that originate from signal like processes are estimated by MC samples. In (8.1), the vector on the right describes the "true" quantities, whereas the vector on the left only contains measurable quantities. The relation shows how to access the "true" contributions, containing pairs of "real" or "fake" electrons, as in N_{RR} or N_{FF}, from the final selection N_{TT}. The coefficients f and r in the matrix describe the probabilities of "fake" and "real" electrons in the "true" selections, that pass the signal-like "tight" requirements, if they are at least reconstructed a "loose" electron candidate.

$$f = \frac{N_{tight}^{fake}}{N_{loose}^{fake}} \qquad r = \frac{N_{tight}^{real}}{N_{loose}^{real}} \tag{8.2}$$

In the definition of these fake rates f and real efficiencies r, the selections $N_{loose}^{real/fake}$ of course also contain the selections of the tight candidates $N_{tight}^{real/fake}$ to build proper efficiencies. After splitting up the contributions of "real" and "fake" pairs to the measurable pairs, which contain two tight electron candidates, the subsets that contain at least one "fake" are:

$$\begin{aligned} N_{TT}^{\ell+jets} &= r_1 f_2 N_{RF} + f_1 r_2 N_{FR} \\ N_{TT}^{multijets} &= f_1 f_2 N_{FF} \\ N_{TT}^{\ell+jets\&multijet} &= r_1 f_2 N_{RF} + f_1 r_2 N_{FR} + f_1 f_2 N_{FF}. \end{aligned} \tag{8.3}$$

By inverting the matrix in (8.1), the "true" quantities N_{ab} can be expressed by the measurable selections N_{xy}.

$$\begin{pmatrix} N_{RR} \\ N_{RF} \\ N_{FR} \\ N_{FF} \end{pmatrix} = \alpha \begin{pmatrix} (f_1-1)(f_2-1) & (f_1-1)f_2 & f_1(f_2-1) & f_1 f_2 \\ (f_1-1)(1-r_2) & (1-f_1)r_2 & f_1(1-r_2) & -f_1 r_2 \\ (r_1-1)(1-f_2) & (1-r_1)f_2 & r_1(1-f_2) & -r_1 f_2 \\ (1-r_1)(1-r_2) & (r_1-1)r_2 & r_1(r_2-1) & r_1 r_2 \end{pmatrix} \begin{pmatrix} N_{TT} \\ N_{TL} \\ N_{LT} \\ N_{LL} \end{pmatrix} \tag{8.4}$$

where

$$\alpha = \frac{1}{(r_1 - f_1)(r_2 - f_2)}. \tag{8.5}$$

When expressing the true terms in (8.3) by the terms in (8.4), the final fake factor selection can be defined:

$$\begin{aligned} N_{TT}^{\ell+jets\&multijets} &= \alpha r_1 f_2[(f_1-1)(1-r_2)N_{TT} + (1-f_1)r_2 N_{TL} + f_1(1-r_2)N_{LT} - f_1 r_2 N_{LL}] \\ &+\alpha f_1 r_2[(r_1-1)(1-f_2)N_{TT} + (1-r_1)f_2 N_{TL} + r_1(1-f_2)N_{LT} - f_1 r_2 N_{LL}] \\ &+\alpha f_1 f_2[(1-r_1)(1-r_2)N_{TT} + (r_1-1)r_2 N_{TL} + r_1(r_2-1)N_{LT} + r_1 r_2 N_{LL}] \\ &= \alpha[r_1 f_2(f_1-1)1-r_2) + f_1 r_2(r_1-1)(1-f_2) + f_1 f_2(1-r_1)(1-r_2)]N_{TT} \\ &+\alpha f_2 r_2[r_1 - f_1) + f_1(1-r_1) + f_1(r_1-1)]N_{TL} \\ &+\alpha f_1 r_1[r_2 - f_2) + f_2(1-r_2) + f_2(r_2-1)]N_{TL} \\ &-\alpha f_1 f_2 r_1 r_2 N_{LL} \end{aligned} \tag{8.6}$$

8.2.2.2. Quality requirements for sub-samples in fake factor method

The identification requirements for real efficiencies fake rates and measurable subsets N_{ab} used as discussed below:
Both tight and loose selection are containing the standard selection used in the analysis except for the *EM-id* requirements. The tight and loose sets consist of:

- tight (T) - standard analysis selection
- loose (L) - pass *loose++* selection but fail *medium++*

To calculate the real efficiencies on signal MC, truth matching is performed with a ΔR requirement between the true and reconstructed electrons of $\Delta R < 0.15$. The corresponding analysis selection is then applied on the matched electrons.

A QCD enriched selection is created to determine the fake rates. This is done by requiring events with same-charged electron pairs, an exclusion window in the invariant mass spectrum around the Z/γ^* resonance of 20 GeV ($|m_{ee} - m_Z| > 20\,\text{GeV}$), and a cut on the missing transverse energy in the event of missing transverse energy $MET < 25\,\text{GeV}$.

The input Monte Carlo are also passed through this selection and any event that passes is subtracted according to their luminosity from the sample collected in data.

8.2.3. Combination of reverse ID template and fake factor methods

To combine the inputs of reverse ID template method and fake factor method the processes that are commonly described by the two methods have to be defined:

- The reverse ID template takes into account
  - QCD multijet events, but
  - no contributions from separately used background MCs. These have to be accounted for by MC correction.
- The fake factor method includes

- QCD multijet backgrounds, as well as
- ℓ + jet events, contained in $W \to e\nu$, semi-electronic events from $t\bar{t}$, Diboson, $W \to \tau\nu$, $Z \to \tau\tau$ Monte Carlo processes.

To generate a common background sample the fake factor method has to be compared to the reverse ID template, stacked with the MC contributions from $W \to e\nu$ and $W \to \tau\nu$, and the semi electronic contributions of $t\bar{t}$, Diboson and $Z \to \tau\tau$ Monte Carlo. When comparing the line shape of the fake factor estimate with the stacked distribution of the reverse ID template and the corresponding Monte Carlo samples in a proper range of the invariant mass, one can derive a scaling factor for the multijet template. In Fig. 8.1 the expected behavior of the two methods is shown: On the one hand at high mass the template method underestimates the prediction of the fake factor method. On the other hand the stack with the reverse ID template behaves as expected at the Z/γ^* mass resonance, while the fake factor method predicts unexpected fluctuations. In the range of $\sim 110 - 200\,\text{GeV}$ both methods estimate a consistent amount of background and also the line shape is consistent. This range is therefore chosen to derive the scale factor for the reverse ID template. The integral of background in the two methods is used to determine this scale factor. This scale is

$$scale^{multijet}_{template} = 0.016328.$$

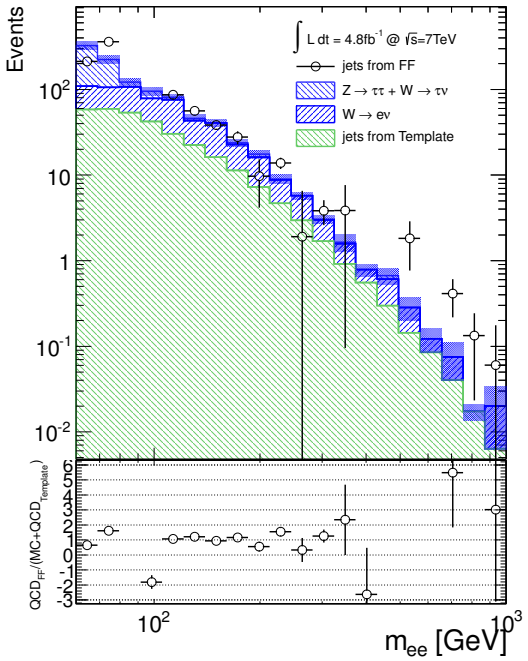

Figure 8.1.: Comparison of reverse ID template stacked with the $W \to e\nu$ and $W \to \tau\nu$, and $Z \to \tau\tau$ Monte Carlo to the fake factor multijet and ℓ+jets estimate. This comparison between the two methods yields flat ratio in about $\sim 110 - 200\,\text{GeV}$ (shown after scaling to the integrals in this range). The semi-electronic contributions of $t\bar{t}$ and the diboson Monte Carlo were estimated to be only a small fraction of these processes and are not displayed but taken into account for the determination of the template scale.

After scaling the reverse ID template, both methods can be used in parallel in their respective region of the invariant mass spectrum. To make the transition between the two estimates easier to propagate to the unfolding and weak mixing angle extraction, the transition is introduced at the mass of 125 GeV, where there is a bin edge in the analysis binning of the A_{FB} spectra.

8.2.4. Summary of multijet Background estimate

The multijet background contamination comprises about 0.1% of the total sample in the CC channel, and about 1.7% in the CF channel. Since it is expected that there is a higher probability for a jet to fake a *forward-medium* electron than a central *medium++* electron, it is not surprising that the multijet background contamination is higher in the CF channel.

8.3. Data-MC comparison

In this section the agreement of data with the set of signal and background Monte Carlo is discussed. In the comparisons all corrections are respected and the statistical and systematical uncertainties of the used samples are propagated.

In the Figures 8.2 - 8.7 data is compared to a stack of all background Monte Carlo, the selected multijet estimate, and the signal MC. Here the background from QCD processes is shown as estimated from the reverse ID template method. In the CC invariant mass plot in Fig. 8.2(a), the reverse ID template is stitched to the fake factor estimate as described in Sec. 8.2.2. Here and in the other CC figures, the scale of the reverse ID template is determined by the fake factor event yield taken from the transition window in invariant mass.

Additionally in Tab. 8.1 a breakdown of the signal and background contribution to the two channels is shown. It is divided in three selected bins at low medium and high invariant masses. The backgrounds are summarised in "Multijet [contributions] from Data Template", taking into account the ℓ+jets events from e.g. W+jets events, while "electroweak" distributions include e.g. $t\bar{t}$ and diboson events.

CC

Mass bin	66-70 GeV	70-250 GeV	>250 GeV
Z/γ^* signal	7800±200	1191000±19000	1450±70
Multijets	230±60	1800±500	20±100
Other backgrounds	115±4	4140±70	210±10
Total expected	8100±300	1197000±19000	1680±120
Data	8281	1198767	1867

CF

Mass bin	66-70 GeV	70-250 GeV	
Z/γ^* signal	1570±110	321000±15000	–
Multijets	800±100	18000±2000	–
Other backgrounds	300±50	7100±400	–
Total expected	2630±150	346000±15000	–
Data	2537	344896	–

Table 8.1.: Observed and expected numbers of events, for each of the two channels (CC and CF) and for three invariant mass bins are given with their total uncertainties for the two background categories (see Sec. 8): multijets, i.e. multijets and W+jets, and other backgrounds, i.e. $t\bar{t}$, dibosons, and $Z \to \tau\tau$.

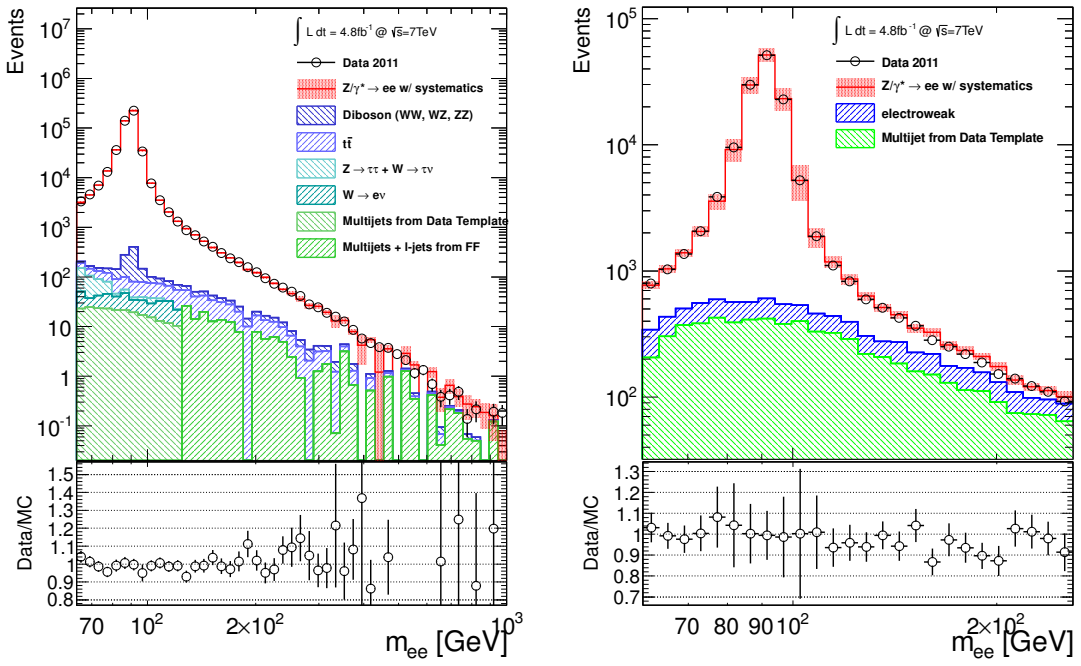

(a) (b)

Figure 8.2.: Invariant mass spectra of the Z/γ^* candidates in the CC (a) and CF (b) channel. Signal MC and backgrounds are shown in colored histograms, data is shown in black open circles. The invariant mass spectrum in the CC (8.2(a)) channel shows the transition (at 125 GeV) between the two different methods for background estimation. Details are given in Sec. 8.2.2. The ratio of data over the summed contributions of signal MC and backgrounds is shown in the lower part of the figures. Statistical and systematical uncertainties are taken into account.

Invariant Mass Distribution

Fig. 8.2 shows the distributions of the invariant mass m_{ee} of the selected electron pairs in logarithmic scale for the x- and y-axes. In the left figure (8.2(a)) the distributions from the CC channel and in the right figure (8.2(b)) the distributions from the CF channel are shown. In the CC channel plot all contributing samples, including the two methods for the multijet estimate, are shown. In the plot for the CF channel only the summed electroweak backgrounds (electroweak) and the multijet estimate (Multijet from Data Template) are included. The other displayed samples are data and the signal Monte Carlo.

The data distributions in both channels show the expected line shape of a rather clean invariant mass resonance with low to medium sized contribution from background processes. In the CC channel the backgrounds are combined as described in Sec. 8.2.3 from the reverse ID template and fake factor method matched at the transition point at 125 GeV. Here the contributions from the reverse ID (Multijet from Data Template) have to be added to the event yields of the $W \to e\nu$, $Z \to \tau\tau$ and $W \to \tau\nu$ samples, to be compared to the multijet and ℓ + jet event yields estimated with the fake factor method (Multijet + ℓ-jets from FF). In this channel the contribution from background processes is low compared to the signal. In the region of the Z/γ^* boson resonance the combined backgrounds are more than two orders of magnitude below the signal. Even at higher masses of about 200 GeV the signal contributes about 10 times more events to the selection as the combined background samples. In the CF channel the signal to

background ratio at the mass resonance is also on the order of 100. Due to the requirements on η_e for the two electrons, the average opening angle between two electron candidates in this channel is larger than in the CC channel. Also due to the higher rate of fake object passing the signal selection at higher values of $|\eta_e|$ and especially in the forward region, the combinatorial contributions, mostly from multijet and ℓ + jet events, are more frequent at higher invariant masses. This leads to the fact that at masses of around 250 GeV the background samples are dominating the invariant mass distribution in the current selection of the CF channel. In general the distributions of the background contributions are smooth and falling towards higher masses. In the CF channel the background tails are falling slower with respect to the CC channel due to the mentioned higher fake rates.

One additional feature that is visible in Fig. 8.2(b) is the turn on of the kinematic acceptance due to the selection requirements on p_T^e and η_e. This is especially visible in the multijet contributions in CF but also affects the Monte Carlo signal and backgrounds in a similar way.

Electron η Distribution

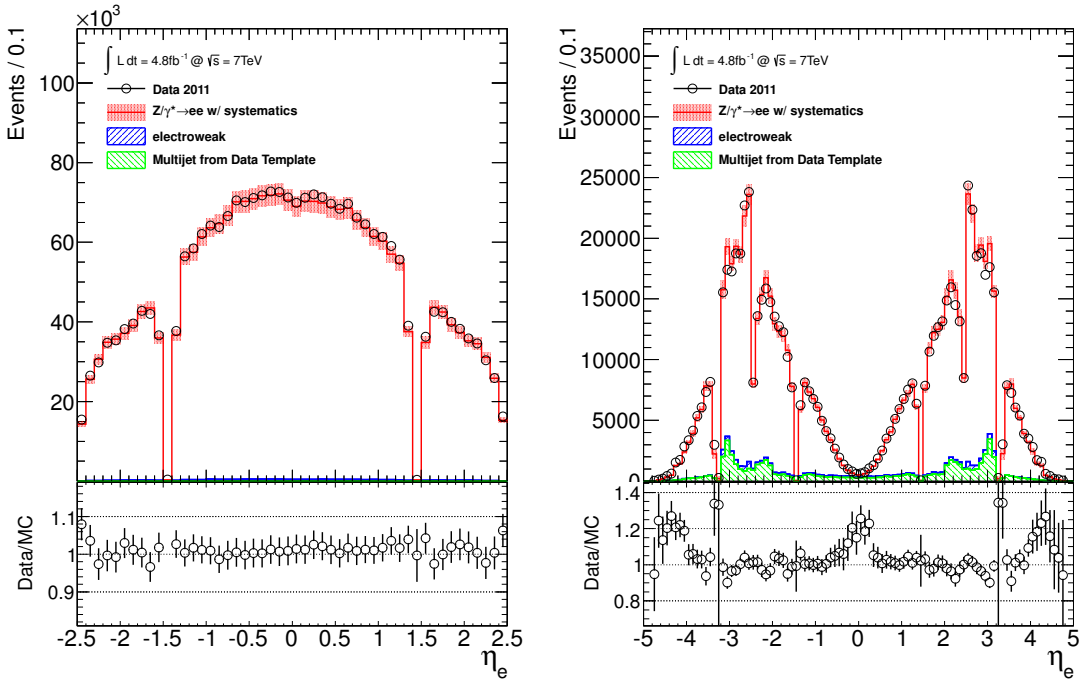

(a) (b)

Figure 8.3.: Electron η spectra of the Z/γ^* candidates in the CC (a) and CF (b) channel. Signal MC and backgrounds are shown in colored histograms, data is shown in black open circles. The ratio of data over the summed contributions of signal MC and backgrounds is shown in the lower part of the figures. Statistical and systematical uncertainties are taken into account.

Fig. 8.3 shows the distributions of the pseudo rapidity η_e of the electrons from the selected electron pairs. In the left figure (8.3(a)) the distributions from the CC channel and in the right figure (8.3(b)) the distributions from the CF channel are shown. Here only the summed electroweak backgrounds (electroweak) and the multijet estimate (Multijet from Data Template) are included in the comparison of data and the signal Monte Carlo. In both figures the distributions are to first order symmetric around $\eta_e = 0$, as the detector and the processes measured don't have a preferred orientation. The spectrum of data and the signal

MC in the CC channel are very close to one another already without taking further background contributions into account. In the CF channel a sizable contribution from electron fakes is visible at around $2 < |\eta_e| < 3$ close to the central - forward transition region. The distributions in the CC channel are centered around $\eta_e = 0$ and the event rates fall off towards higher values in $|\eta_e|$. This is because of the phase space restrictions of the selection and the contributing process. These restrictions include the fact that the available rapidity range of the production of resonances on the scale of about $Q = 100\,\text{GeV}$ is restricted to about $|y| \lesssim 5$. The requirements concerning the range of detector acceptance in the two channels are further restricting the mentioned phase space. This even more holds for the CF channel, where, due to the mentioned selection requirements on η_e, the distribution is centered around the transition regions at $|\eta_e| = 2.5$ and the event rates fall off towards higher values in $|\eta_e|$ as well as towards $\eta_e = 0$. These tails are therefore a result of the available phase space in the CF selection and the asymmetric requirement of the allowed combination of $\eta_e^{c,f}$. In both figures for CC and CF the transition regions between the different electromagnetic calorimeters are visible. At the respective bins around $\eta_e \approx 0$, $|\eta_e| \approx 1.45$, $|\eta_e| \approx 2.5$ and $|\eta_e| \approx 3.2$, dips in the event yields are visible. This is a result of the cleaning cuts in the event selection at these positions. Here the energy measurement as well as the electron shower shapes in the calorimeters are potentially distorted, in addition to a lower sensitivity of the calorimeters them self. These distortions are e.g. a result of the support structures that hold the calorimeter compartments in place. Here also the agreement between data and MC is worse with respect to other bins in the distributions, because differences in the selection and identification efficiencies are not easily recoverable by scale factors.

The effect that there seems to be a modulation in the ratio between data and MC can be explained by two issues: the first is, at least in the CF channel, the simple fact that the exact misidentification rate of fakes in the selection is not a constant across η_e and that this is one of the flaws of the reverse ID method. The other point is that the p_T^{ee} as well as the rapidity y_{ee} of the Z/γ^* boson is not perfectly modeled by the chosen event generator and the currently used Monte Carlo tune.

Finally there is a small asymmetry in the spectra in the positive half barrel visible for the distributions of both channels. This is the resulting deficiency affecting about 1-2% of the events that was caused by the failure of the FEB as discussed in Sec. 4.1.

Electron ϕ Distribution

Fig. 8.4 shows the distributions of the azimuthal angle ϕ_e of the electrons from the selected electron pairs. In the left figure (8.4(a)) the distributions from the CC channel and in the right figure (8.4(b)) the distributions from the CF channel are shown. Here only the summed electroweak backgrounds (electroweak) and the multijet estimate (Multijet from Data Template) are included in the comparison of data and the signal Monte Carlo.

Both figures show a flat behaviour that is consistent with the 2π rotation symmetry of the detector and beam collision setup as well as all hard processes expected to be produced in the experiment. The small crossing angle, in which the proton beams are passing through one another, does not affect this behaviour. The distortion in the uniformity of the distributions is caused by the failure of the FEB as previously explained in Sec. 4.1. Though this failure is only present in a short period of the data taking it still affects the overall uniformity. The region that is affected is located in one half-barrel at about $0 < \eta \lesssim 1.45$ in one slice in the read out in ϕ at about $-0.8 \lesssim \phi \lesssim -0.6$. The other dip at $\phi \approx 2.5$ is a result of the electron pair based selection, in which also the companion electrons is removed from the affected events. Because the faulty detector region is located in the barrel section, the effect on the CF selection is hardly visible.

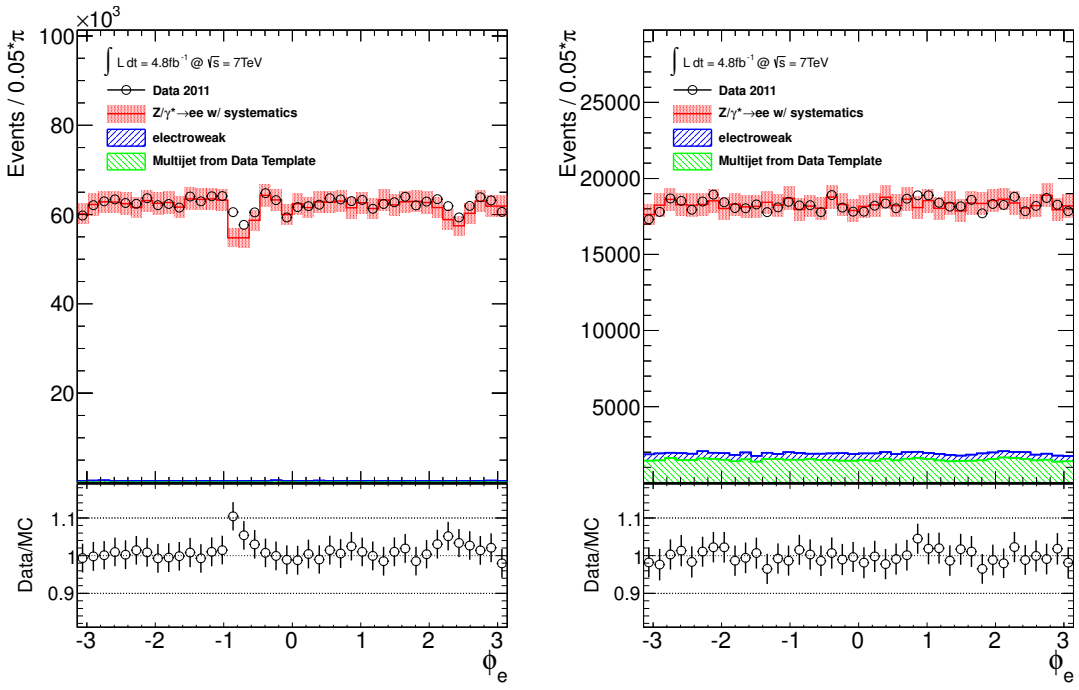

Figure 8.4.: Electron ϕ spectra of the Z/γ^* candidates in the CC (a) and CF (b) channel. Signal MC and backgrounds are shown in colored histograms, data is shown in black open circles. The ratio of data over the summed contributions of signal MC and backgrounds is shown in the lower part of the figures. Statistical and systematical uncertainties are taken into account.

In the CF channel, where the background contributions is visible in the ϕ distribution, also there are as expected no distortions from the uniform behavior visible. The modulations that can be seen in the data selection in CF are most likely due to the response of the accordion structure of the EM calorimeter as described in Sec. 3.2.4.1.

Electron p_T Distribution

Fig. 8.5 shows the distributions of the transverse momentum p_T^e of the electrons from the selected electron pairs in logarithmic scale for the y-axes. In the left figure (8.5(a)) the distributions from the CC channel and in the right figure (8.5(b)) the distributions from the CF channel are shown. Here only the summed electroweak backgrounds (electroweak) and the multijet estimate (Multijet from Data Template) are included in the comparison of data and the signal Monte Carlo. The signal follows the behaviour of a Jacobean distribution while the background contributions have a more or less exponential behaviour. The most frequented value in the distributions is the reflection of the Z/γ^* resonance at about the half of the mass of the Z boson. In the CF distributions this most probable value is shifted towards lower transverse momenta.

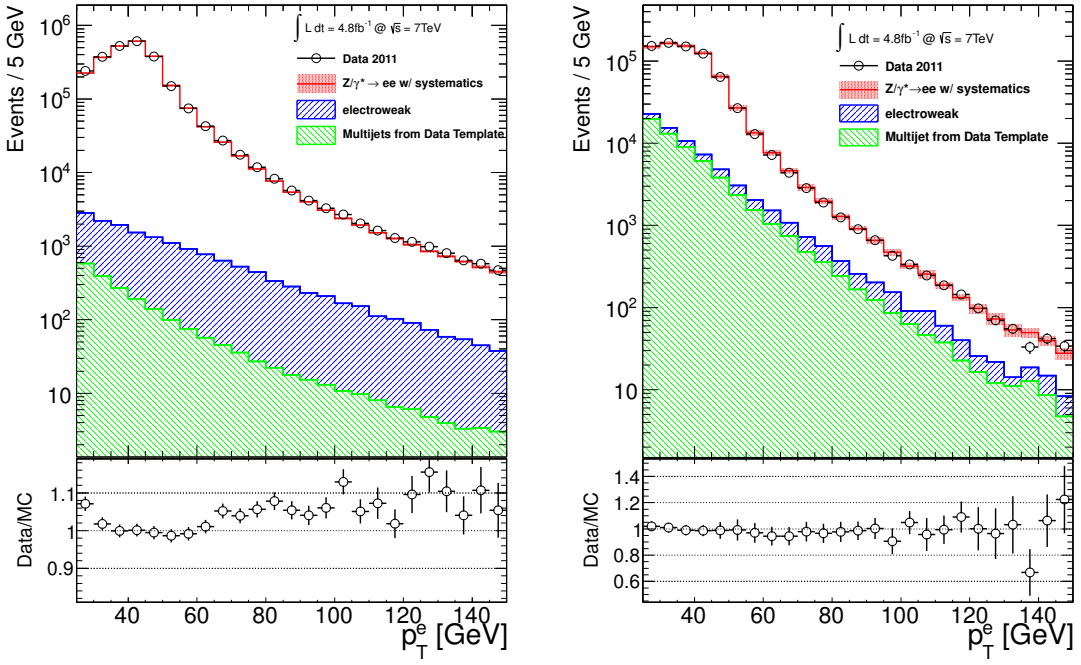

(a) (b)

Figure 8.5.: Electron p_T spectra of the Z/γ^* candidates in the CC (a) and CF (b) channel. Signal MC and backgrounds are shown in colored histograms, data is shown in black open circles. The ratio of data over the summed contributions of signal MC and backgrounds is shown in the lower part of the figures. Statistical and systematical uncertainties are taken into account.

Di-Electron Rapidity Distribution

Fig. 8.6 shows the distributions of the di-electron rapidity y_{ee} of the selected electron pairs. In the left figure (8.6(a)) the distributions from the CC channel and in the right figure (8.6(b)), the distributions from the CF channel are shown. Here only the summed electroweak backgrounds (electroweak) and the multijet estimate (Multijet from Data Template) are included in the comparison of data and the signal Monte Carlo. Both distributions are to first order symmetric around $y_{ee} = 0$, as the detector and the processes measured don't have a preferred orientation. In the CC channel the spectrum of data and the signal MC are very close to one another already without taking into account further background contributions. In the CF channel a sizable contribution from electron fakes is visible at $2 < |y_{ee}| < 3$ around the central-forward transition region. The distributions in the CC channel are centered around $y_{ee} = 0$ and the event rates fall off towards higher values in $|y_{ee}|$. This is a result of the phase space restrictions of the selection and the contributing process. The CF channel distributions are centered around the transition regions at $|y_{ee}| = 2.5$ and the event rates fall off towards higher values in $|y_{ee}|$ as well as towards $y_{ee} = 0$. These tails are also a result of the available phase space in the CF selection and the asymmetric requirement of the allowed combination of $\eta_e^{c,f}$. The combinatorial contributions, especially from higher invariant masses, are resulting in very central rapidities.

The effect that there seems to be a modulation in the ratio between data and MC, can be explained by two issues: the first is, at least in the CF channel, the simple fact that the exact misidentification rate of fakes in the selection is not a constant across y_{ee} and that this is one of the flaws of the reverse ID method. The

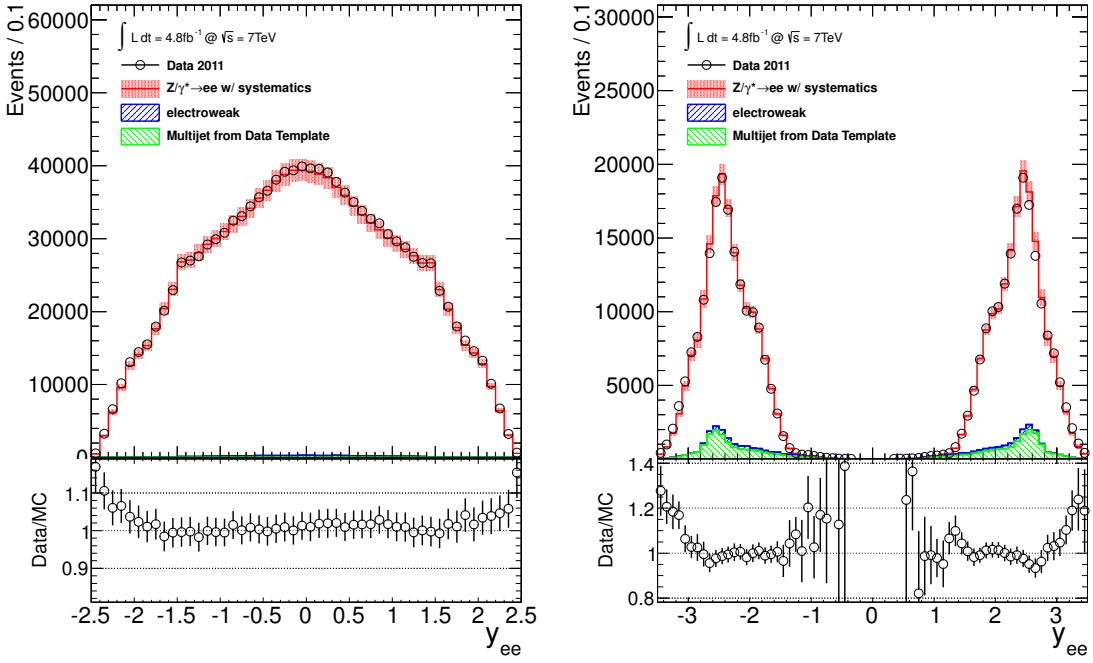

(a) (b)

Figure 8.6.: Di-electron rapidity spectra y_{ee} of the Z/γ^* candidates in the CC (a) and CF (b) channel. Signal MC and backgrounds are shown in colored histograms, data is shown in black open circles. The ratio of data over the summed contributions of signal MC and backgrounds is shown in the lower part of the figures. Statistical and systematical uncertainties are taken into account.

other point is that the p_T^{ee} as well as the rapidity y_{ee} of the Z/γ^* boson is not perfectly modeled by the chosen event generator and the currently used Monte Carlo tune.

The discrepancies in the estimate of the events with $|y| < 1.5$ in the CF channel are a result of the high background contamination from multijet events in the high mass region above $\sim 150\,\text{GeV}$, that can be seen in Fig. 8.2(b).

Di-Electron p_T Distribution

Fig. 8.7 shows the distributions of the di-electron transverse momentum p_T^{ee} of the selected electron pairs in logarithmic scale for the y-axes. In Fig. 8.7(a) the distributions from the CC channel and in Fig. 8.7(b) the distributions from the CF channel are shown. Here only the summed electroweak backgrounds (electroweak) and the multijet estimate (Multijet from Data Template) are included in the comparison of data and the signal Monte Carlo. The distributions of signal and backgrounds have their most probable values close to 0 and are falling according to a power law distribution. There are no structures in the tails, only the way the turn on is behaving differently.

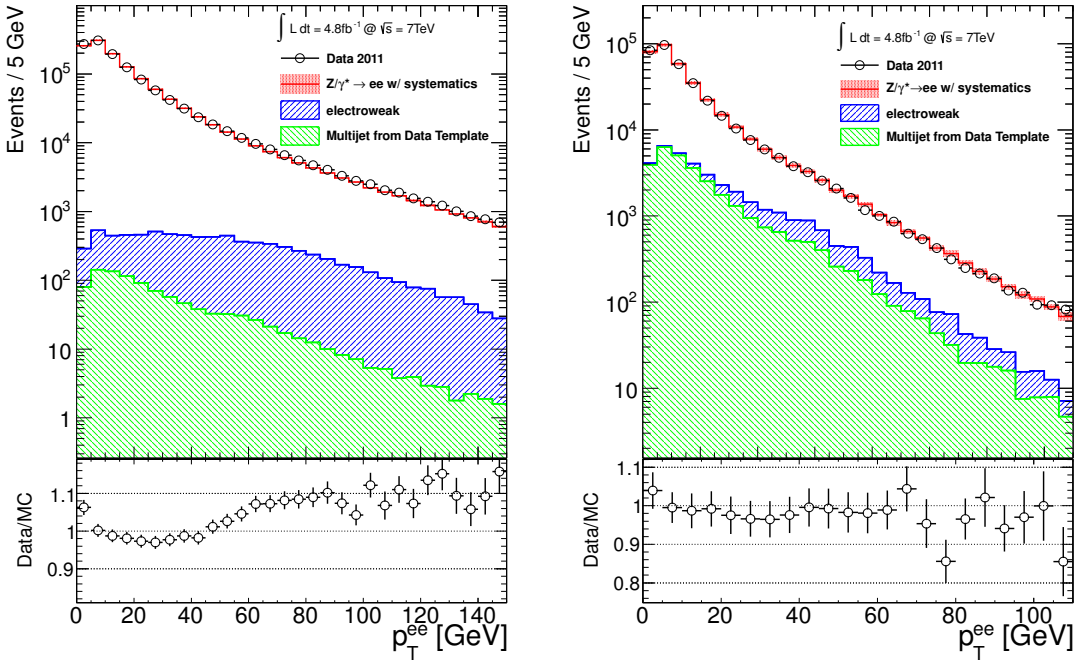

(a) (b)

Figure 8.7.: Di-electron p_T spectra of the Z/γ^* candidates in the CC (a) and CF (b) channel. Signal MC and backgrounds are shown in colored histograms, data is shown in black open circles. The ratio of data over the summed contributions of signal MC and backgrounds is shown in the lower part of the figures. Statistical and systematical uncertainties are taken into account.

9. Measurement of A_{FB}

In this chapter the distributions of the Forward-Backward-Asymmetry measured in the different samples contributing to this analysis are discussed. The discussion in this chapter focuses on the raw distributions of the selected events. In Sec. 9.1 the samples of data and signal Monte Carlo are compared in the distribution of $\cos\theta^*_{CS}$, that is the basis of the A_{FB} measurement as introduced in Sec. 2.3.1. This comparison includes the contributions of the background processes. The impact of the background samples and their behavior in terms of the A_{FB} are discussed in Sec. 9.2. Here also the correction of the background contributions off the measured data is discussed. In Sec. 9.3 the impact of the corrections as introduced in Sec. 6.1 is evaluated. These corrections can yield systematic variations to the selection and the line shape of $\cos\theta^*_{CS}$ and A_{FB}. They are treated as sources of systematical uncertainties. Finally in Sec. 9.4 a setup to unfold these raw distributions is introduced. Here the unfolding method is discussed, which was studied in the corresponding ATLAS publication [28], that is the basis for this thesis.

9.1. Raw distributions of $\cos\theta^*_{CS}$

The raw distributions of A_{FB} are based on the distribution of events in the spectra of $\cos\theta^*_{CS}$. These spectra reflect the decay angle of outgoing leptons with respect to the incoming partons in the Collins-Soper reference frame as defined in Sec. 2.3.1. The distributions of A_{FB} as well as $\cos\theta^*_{CS}$ are depending on the invariant mass of the selected events. To study the dependency of the asymmetry with respect to the invariant mass, it is also essential to investigate the distribution of the underlying quantity $\cos\theta^*_{CS}$ in specific ranges of the invariant mass spectrum before. The invariant mass range is studies in the windows $60-80\,\text{GeV}$, $80-100\,\text{GeV}$, $100-250\,\text{GeV}$ and $250-1000\,\text{GeV}$ for the CC and CF channel. Here it can be seen that the combined distributions of signal MC and the background contributions nicely agree with the distributions in data. The problematic estimate in the high mass region of the CF channel is dominated by the contributions from multijet events as expected. The results are shown in Fig. 9.1.

According to (2.3.8) the distributions of A_{FB} can now be calculated. As it can be seen in the distributions shown for the CF channel, the background contributions are not negligible, especially in higher ranges of the invariant mass. Therefore a correction of background contributions is needed. Because one aim of this thesis is to extract the weak mixing angle $\sin^2\theta^{\text{eff}}_W$ from the raw A_{FB} distributions, as will be discussed in Sec. 10, it is chosen to perform background subtraction on data in contrast to combining the backgrounds with the signal Monte Carlo. This way the line shape of A_{FB} in the signal process is kept and the formalism of the weak mixing angle extraction is simplified.

The same also holds for the unfolding of the A_{FB} distributions as introduced in Sec. 9.4, which is performed for the published ATLAS results.

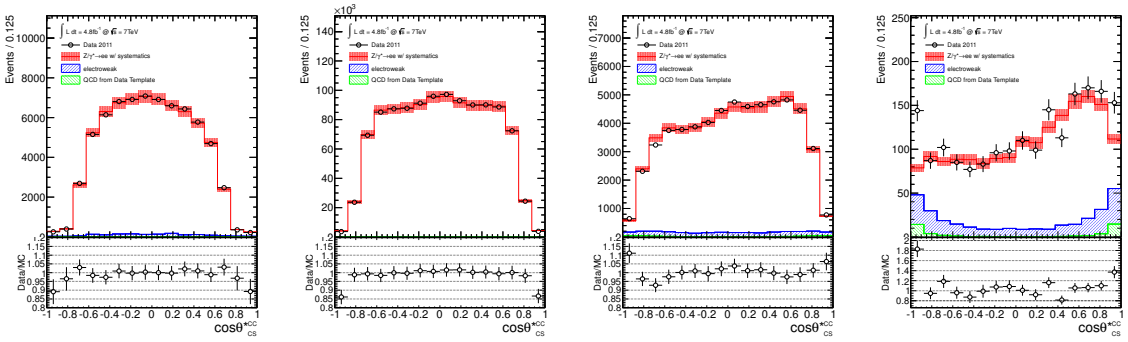

(a) CC 60-80 GeV (b) CC 80-100 GeV (c) CC 100-250 GeV (d) CC 250-1000 GeV

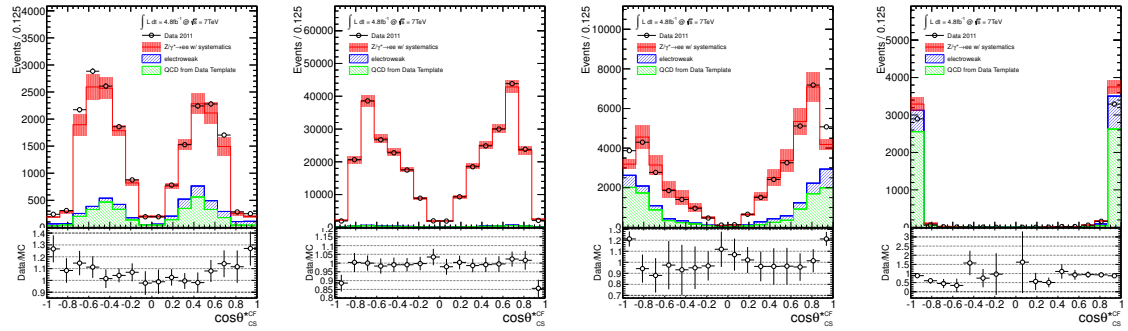

(e) CF 60-80 GeV (f) CF 80-100 GeV (g) CF 100-250 GeV (h) CF 250-1000 GeV

Figure 9.1.: Di-electron $\cos\theta^*_{CS}$ spectra of the Z/γ^* candidates in the CC (a-d) and CF (e-h) channel. Signal MC and backgrounds are shown in colored histograms, data is shown in black open circles. The $\cos\theta^*_{CS}$ distributions are binned in invariant mass ranges of 60-80 GeV, 80-100 GeV, 100-250 GeV and 250-1000 GeV. The ratio of data over the summed contributions of signal MC and backgrounds is shown in the lower part of the figures. Statistical and systematical uncertainties are taken into account.

9.2. Backgrounds in the A_{FB} measurement

In order to study the influence of the background samples in more detail, the A_{FB} distributions of the different classes of backgrounds are shown in Fig. 9.2. The distributions of A_{FB} for the electroweak and the multijet contributions are presented in the same binning, that is used for the signal A_{FB} distributions. This way the impact of the backgrounds can be estimated.

It is expected that the vanishing values of A_{FB} in the multijet backgrounds lead to an inverted dilution, when data is corrected. This means that the diluting impact of this background is removed from the A_{FB} again. The distributions of the electroweak backgrounds are not expected to just dilute the distributions. Especially in the CF channel the contribution of the $W \to e\nu$ background is expected to yield an asymmetric contribution to data. In this channel the strength of the background rejection in the chosen *EM-id* is not equal for the central and the forward electron of this selection. For this reason the probability to misidentify a jet from the forward region and combine it with a real electron that is emitted by the decay of a W boson in the central region is enhanced. If the rate of W decays with positive and negative charge would be the same, the effect might cancel out to first order. Due to the fact that in the experiment pp collisions are studied and the amount of valence u-quarks is increased by a factor two with respect to valence d-quarks, the rate of W decays is about twice as high for positively charged gauge bosons than for their negatively charged counter parts. Therefore there is no cancellation of the rates of W^+ and W^-

decays in this selection. The problem arises as the sign of $\cos\theta^*_{CS}$ in the Collins-Soper frame, which is measured on the reconstructed quantities, is defined with respect to the boost of the di-electron system. In the W^+ decays the direction of the e^- is pointing forwards, where as the e^- in the W^- decays is pointing backwards in terms of $\cos\theta^*_{CS}$. Therefore the rate of forward events is enhanced and the A_{FB} spectrum of the W sample in the CF selection is asymmetric.

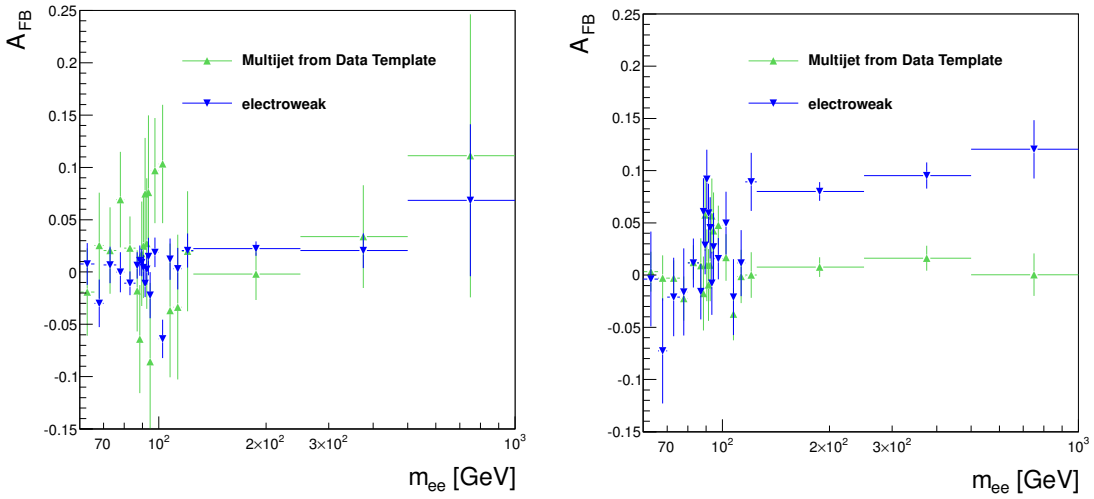

(a) A_{FB} spectrum for backgrounds in CC events.

(b) A_{FB} spectrum for backgrounds in CF events

Figure 9.2.: A_{FB} spectra of electroweak MC and Multijet events in the CC (a) and CF (b) channel.

The discussed background samples can now be taken into account and the corresponding event yields of forward and backward events can be used to correct the data distribution of the respective selection channel. The background corrected data distributions are shown in Fig. 9.3 compared to the A_{FB} distributions obtained from the signal Monte Carlo. Here only the propagated statistical uncertainties are applied to the displayed distributions.

9.3. Systematic variations

To derive the impact of the calibrations and the corrections applied to the input samples as discussed in Sec. 6.1, a corresponding set of variations within the uncertainties of these corrections has to be performed. Variations of the input samples are propagated through the full selection. The resulting distributions are compared to derive the impact of the respective parameter variations. The corrections with the largest set of variations are the calibration of the electron energies and the reweighting to different PDF eigenvectors. The uncertainties of the electron energies are parametrized with seven sets of respective variations. Six of these are within the uncertainty of the data energy scale while one additional set of variations is derived with respect to the calibration of the Monte Carlo energy resolution.

For the reweighting of the selected signal Monte Carlo sample within the uncertainties of chosen parton distribution functions, twenty to thirty eigenvectors can be defined, that build the basis of the respective PDF parametrisation. With this in mind there is a sizable effort in treating the variations properly.

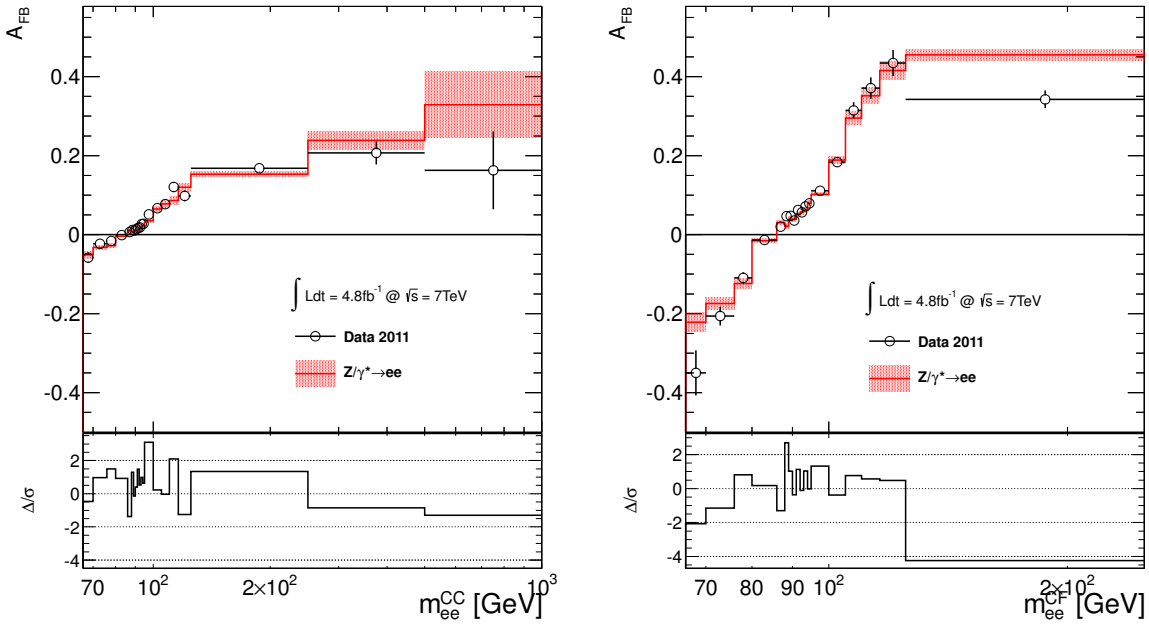

(a) (b)

Figure 9.3.: A_{FB} spectra of the Z/γ^* candidates in the CC (a) and CF (b) channel. Signal MC is shown with colored histograms, background subtracted data is shown in black open circles. Full background subtraction is performed on data, but only statistical uncertainties are shown. In the lower parts of the figures Δ/σ rations are shown, that give the difference Δ of the distributions above divided by the combined uncertainty.

Further variations are performed with respect to the reweighting of the Monte Carlo pile-up conditions and within the uncertainties of the electron dependent scale factors. For the impact of the variations in pile-up conditions the distributions of simultaneous interactions in the Monte Carlo signal was varied. For the scale factors the provided uncertainties were propagated to the events weights. The variation within the uncertainties of the scale factors are expected to yield only very low contributions to the overall systematical uncertainty of the A_{FB} distributions. This is because the scales should not affect the event weights differently for forward events with respect to backward events. Other sources that have the characteristics of a systematic uncertainty are the level of confidence that can be assigned to the background distributions and also the possible fluctuations, that are related to the statistical precision of the signal Monte Carlo sample. This can also treated as statistical uncertainty in the comparisons of data to Monte Carlo line shapes. In general the uncertainties can be treated fully un-correlated. Their contribution to the overall systematic variation is estimated by adding the individual uncertainties quadratically bin-by-bin in all relevant distributions. Because these variations have to be estimated for each distribution separately, there can also be differences between two related distributions of the same set of events with respect to the same systematic variation. Especially scale variations in general have strong impact on the quantities like the event yield but can hardly affect ratios of quantities or asymmetries. This holds as long as the scales are not directly depending on the inputs to that rational quantities or asymmetries.

9.3.1. Energy scale uncertainty

The propagation of the uncertainties of the energy calibration are performed according to the recommendations of the eGamma performance group. These variations are applied before performing the selection. As discussed in Sec. 6.1.3 and Sec. 7 the energy scale correction, that is to be applied on the electron energies in data, is provided with a set of six independent variations. The variation of the energy resolution, that is to be used with the simulated samples, is provided in only one respective uncertainty. These are the uncertainties that are also used in the propagation of the central electron energy scale uncertainties in the forward energy calibration section Sec. 7.3. Of course also the uncertainties derived in that respective part of the analysis are used, which are to be applied for the forward electrons energy calibration.

As discussed above, the effect of a variation on the energy scale is that the invariant mass spectrum in data is shifted to match the energy response in the detector simulation. On the simulated sample the width of the Z/γ^* resonance is broadened by the correction to the energy resolution to match the line shape in the calibrated distributions in data.

The uncertainties taken into account for the energy scale variation consist of contributions of the statistical precision of the nominal calibration constants as well as variations that are obtained by the different methods used to calculate the parameters for the calibration. Further, the effect of the sampling of the calorimeter was studied alongside with a special variation of the linearity of the energy response that only affects low energetic electrons with transverse momenta of $p_T^e < 15\,\text{GeV}$.

The uncertainty due to the variation in the calibration constants of the resolution correction has to be applied with a caveat: There are cases where the energy resolution is already worse in Monte Carlo as it is in data. Also in cases when the uncertainty on the resolution correction would imply to increase the resolution on the Monte Carlo, the variation can be limited by the resolution of the precalibrated electron response without applying an additional correction.

The resolution correction is only defined to provide an additional smearing factor according to a Gaussian distribution around 1.0, which uses the smearing constant as the width of the smearing function. This smearing factor is then multiplied to the original energy response to yield the calibrated result. Because the width is defined to be a positive number or zero, only variations of the resolution parameter in the up direction or variations in the down directions that are smaller or equal to the calibration constant can be propagated.

In the case when the down variation would cause the gaussian to use a negative width, the smearing is not applied, which corresponds to a Gaussian with a width of zero. This is independent of the fact whether the central resolution parameter is zero or not, but it has the effect that the variation can be asymmetric for some regions in η_e. The resulting deviations with respect to the default calibration are added in quadrature and can be used as a combined uncertainty envelope.

The impact of these variations on the A_{FB} distributions are shown in Fig. 9.6 together with the uncertainties of the other variations.

9.3.2. PDF uncertainty

As introduced above in Sec. 2.2.1 with the theoretical motivation of parton distribution functions, the set of PDFs that is used in the simulation of a Monte Carlo sample is usually related to uncertainties on the input distributions and quantities of the respective PDF. These uncertainties are propagated to build

so called PDF error sets of variations of the central set of predictions. The variations are provided with respect to a change of a combination of input parameters along an eigenvector of the internally arranged orthogonal dependencies of the PDF. Each PDF set inside these error sets corresponds to a variation along an eigenvector of the PDF that corresponds to a certain confidence level (CL) error interval. In the case of e.g. the PDF error set that is assigned to the *CT10* PDF of the CTEQ [37] collaboration, this error interval corresponds to 90% CL variations. To estimate the uncertainty that is comparable to a 1σ variation, which is equal to an error interval of 68% CL, it is recommended to calculate the full PDF uncertainty from all variations and scale the corresponding value of the uncertainty afterwards down by a factor of 1.64. This factor corresponds to the ratio of the sizes of the 90% CL and 68% CL intervals, assuming, that the distribution of the uncertainties is Gaussian.

The PDF reweighting is performed on the information stored in the signal Monte Carlo samples. It is used in the event generation step to calculate the respective event probability according to the default PDF. As discussed in Sec. 2.2.1 the probability $f_{\mathrm{PDF_j}}(x_i, q_i, Q^2)$ for a parton i to take place in a parton-parton interaction in a hadron-hadron collision with the PDF set j depends on the flavors q_i of the parton. It also depends on the momentum fraction of the parton in the respective hadron x_i, as well as the scale of the momentum transfer in the hard interaction Q^2. The weight w that is to be calculated for the reweighting of an event with the parton indices $i \in \{1, 2\}$ and the PDF sets $j \in \{1, 2\}$ is:

$$w = \frac{f_{\mathrm{PDF_2}}(x_1, q_1, Q^2) \cdot f_{\mathrm{PDF_2}}(x_2, q_2, Q^2)}{f_{\mathrm{PDF_1}}(x_1, q_1, Q^2) \cdot f_{\mathrm{PDF_1}}(x_2, q_2, Q^2)}. \tag{9.1}$$

Here the PDF indicated with $j = 1$ has to be the PDF used to generate the MC sample where as the PDF with $j = 2$ is the one that the sample is going to be reweighted to.

To estimate the related PDF uncertainty for this analysis, it was recommended by experts within the ATLAS collaboration [68], that are performing dedicated studies on PDF uncertainties, to use the PDF error set of the *CT10* PDF to cover all possible systematic effects due to PDF variation. It is further recommended to check that the variation to the central PDF of the *MSTW2008LO* PDF set is covered by the variations within the error set of the *CT10* PDF.

To calculate the combined PDF error from this error set, the eigenvector up and down variations are compared to the central PDF in the set. This makes a total of 56 PDF reweighting steps to be performed for each of the two selection channels. The rather large number of variations consists of the use of $1 + 52 + 2$ PDF sets from *CT10* PDF error set (one central PDF, 26 eigenvectors of two variations each as well as two the values of α_s of 0.116 and 0.120, with respect to the default value of the set of $\alpha_s = 0.118$ in this PDF) and in addition the reweighting to the *MSTW2008LO* PDF set to check the coverage of the variations. The variation of the α_s parameter to estimate the PDF uncertainty is an optional variation. Further the impact of this variation is small and it was decided to leave it out for the combination of the PDF uncertainty in the combined analysis.

The errors are to be calculated on a respective final quantity X. This means that for the case that the final quantity is a single number the analysis has to be performed with all reweighted PDF eigenvector variation to the point this number can be extracted. In the case where the final quantity is a distribution, each point in this distribution can be treated as a final quantity itself and the respective analysis has to be performed on all eigenvector variations to gather this final distribution. For this respective quantity X the symmetrical uncertainty ΔX, resulting from the PDF variations, can be calculated as follows:

$$\Delta X = \frac{1}{2} \sqrt{\sum_{i=1}^{N} \left(X_i^{(+)} - X_i^{(-)} \right)^2}. \tag{9.2}$$

Here it is assumed that asymmetrical contributions do not play a sizable role for the given quantity. Alternatively the uncertainty can also be derived asymmetrically from the set of variations. This way it can be tested if the amount of variations that lead to an upwards and downwards fluctuation of the final result, given the variations of the respective PDF, are equal. In that case a symmetrical uncertainty can be quoted that should be of the same order as the error derived by the calculation of (9.2). Otherwise the asymmetrical uncertainties can be cited for the final results.

The asymmetrical uncertainties to the quantity X can be calculated with:

$$\Delta X^{(+)} = \sqrt{\sum_{i=1}^{N} \left(\max\left(\left(X_i^{(+)} - X_i^0\right), \left(X_i^{(-)} - X_i^0\right), 0\right)\right)^2} \tag{9.3}$$

$$\Delta X^{(-)} = \sqrt{\sum_{i=1}^{N} \left(\max\left(\left(X_i^0 - X_i^{(+)}\right), \left(X_i^0 - X_i^{(-)}\right), 0\right)\right)^2}. \tag{9.4}$$

The propagation of uncertainties with use of the equations (9.2), (9.3) and (9.4) can also be performed to any other type of combined uncertainty due to a set of systematic variations.

The impact of these variations on the A_{FB} distributions is shown in Fig. 9.6 together with the uncertainties of the other variations.

9.3.3. Background modeling

The A_{FB} distribution in data has to be corrected for background contributions. The stability of the samples, that these corrections are built of, can be assigned as a systematic variation to the corrected line shape of the data sample. As the background corrections that are used in this analysis are constructed of Monte Carlo based and data driven contributions, the related treatment of the uncertainties can differ. For the MC-based corrections an uncertainty can be assigned to the statistical uncertainty as well as to the related uncertainty on the cross section of the chosen sample. The statistical component is already propagated with the subtraction of the background contribution to the uncertainty of the background corrected data distributions. For the uncertainty on the cross section of the background contributions a global scale of 10% is selected to be sufficient. On the systematical uncertainty of the data driven contributions, that are again referred to as multijet contributions, special estimates are made respective to the methods used in the CC and CF channel.

In the CC channel the multijet background is constructed from the reverse ID and fake factor method. The two methods are combined in the invariant mass spectrum at 125 GeV as described in Sec. 8.2.3. In the nominal setup the scale for the reverse ID template is determined by the fake factor method in an invariant mass range where both methods are checked to describe the background contributions reasonably well. This is shown in Fig. 8.1. As a first variation to asses the systematic uncertainty in the lower part of the invariant mass spectrum, the scale factor that is needed for the reverse ID method is fit by the same fractional fit method that is used in the CF channel. The difference in the event yield of these two estimates is assigned as the systematic uncertainty in the range up to 125 GeV. Above this range the difference between the reverse ID template scaled with the nominal scale factor and the distribution obtained by the fake factor method is used to describe the uncertainty of the multijet background in the CC channel.

To assess the uncertainty of the reverse ID template in the CF selection, the alternative definition of the multijet template that is introduced in Sec. 8.2.1 is used. Fig. 9.4 displays the difference of the two

templates, after subtraction of the background Monte Carlo from the data A_{FB} distribution. Additionally it is taken into account how large the effect of no multijet background correction is. The resulting values for the corrected A_{FB} distributions are also listed in Tab. 9.1. As shown in Fig. 9.4(a) the omission of the multijet background corrections is producing a very strongly diluted A_{FB} distribution at invariant masses above $\sim 100\,\text{GeV}$. Using the alternative definition of the multijet template, that has stronger statistical limitation with respect to the nominal selection, there is a equally sized pull in the other direction in the asymmetry spectrum. This is shown in Fig. 9.4(b). Because of these findings the difference between the nominal and alternative modeling of the multijet contribution to the CF selection is applied as a systematic to the current multijet distribution.

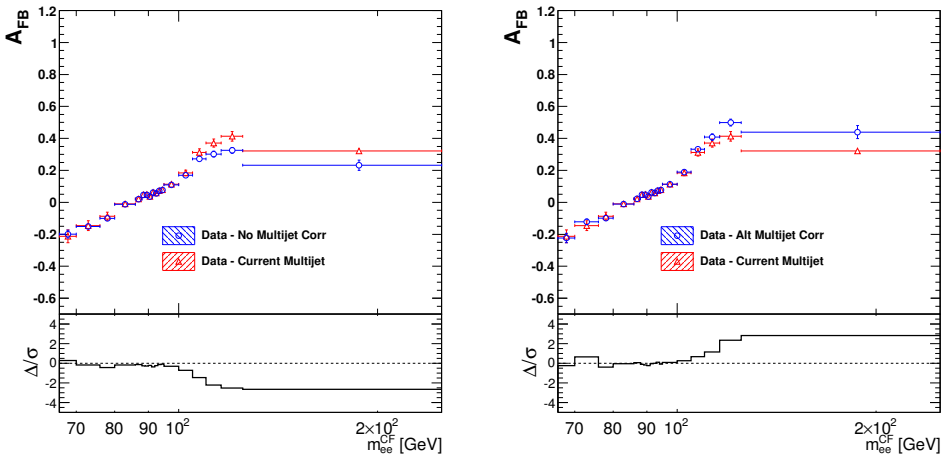

(a) (b)

Figure 9.4.: A_{FB} distribution in data with the nominal multijet estimate compared to no subtraction of multijet contributions at all (a) and the alternative multijet template (b). All uncertainties are showing statistical errors only.

9.3.4. Other uncertainties

The variation of the remaining corrections, that are studied for their impact on the systematical variation of the A_{FB} distribution are the pile-up correction and the electron scale factors. As mentioned before the impact of the scale factor uncertainties on A_{FB} is expected to be small, but it was taken into account as it does have a sizable influence on the systematic uncertainties of the kinematic distributions shown in Sec. 8.3. Each set of scale factors was varied independently, which includes the reconstruction and track matching, the trigger, as well as the identification scale factors. The variation of these scales is performed correlated for all scales of the same type. For example for the variation of the identification scale factors, the scales of both electrons were varied in the same direction in both selection channels. That means that especially in the CF channel, there are always the two independent sets of central and forward scales varied in the same attempt.

The variation in terms of the pile-up conditions on the signal Monte Carlo has an impact on the amount of hadronic activity in the calorimeters. Therefore an effect on the combinatorial background contribution as well as on the energy measurement is expected to be present. As there was no official recommendation present that was applicable to this analysis, it was decided within the analysis group to perform a variation of the input distribution of simultaneous interactions μ in the signal Monte Carlo sample.

m_{ee}^{CF} Range [GeV]	A_{FB}^{data} Nominal	A_{FB}^{data} None	A_{FB}^{data} Alternative
66-70	-0.2126	-0.1996	-0.2246
70-76	-0.1456	-0.1526	-0.1226
76-80	-0.0876	-0.1006	-0.0996
80-86	-0.0106	-0.0136	-0.0116
86-88	0.0215	0.0205	0.0225
88-89	0.0485	0.0465	0.0475
89-90	0.0495	0.0475	0.0485
90-91	0.0375	0.0365	0.0355
91-92	0.0635	0.0615	0.0625
92-93	0.0585	0.0565	0.0585
93-94	0.0735	0.0725	0.0745
94-95	0.0785	0.0775	0.0775
95-100	0.1135	0.1095	0.1145
100-105	0.1845	0.1695	0.1905
105-110	0.3125	0.2725	0.3325
110-116	0.3715	0.3025	0.4085
116-125	0.4135	0.3255	0.4995
125-250	0.3225	0.2325	0.4405

Table 9.1.: This table shows the numerical results of the A_{FB} per invariant mass bin for three different types of modeling of the multijet background in the CF selection channel:
the nominal model used in the analysis, not taking the multijet contributions into account at all, and the alternative model of the multijet background including an inverted isolation requirement are shown.

This distribution is used to determine the scaling factor applied to the Monte Carlo event with a certain value μ with respect to the measured number of simultaneous interactions in data. By scaling the values of μ by $\pm 10\%$ in the simulation, the level of uncertainty that is inherent to this method should be well covered. Also the impact of these variations on the A_{FB} distributions is shown in Fig. 9.6 together with the uncertainties of the other variations.

In these official variations also the effect of higher order contributions to the A_{FB} line shape have been studied in the common analysis [28]. These uncertainties are obtained by calculating k-factors for the A_{FB} distributions for the NLO effects of the QCD HO with the MCFM event generator and the HO EW contributions with the HORACE event generator. The resulting uncertainties due to the application of the mentioned k-factors have been included in the official figures of the raw asymmetry as shown in Fig. 9.5 and are included in the systematic uncertainties of the weak mixing angle extraction discussed in Sec. 10.3.3.

9.3.5. Combined uncertainty

To combine the different contributions of uncertainty the individual variations with respect to the nominal calibration are added in quadrature bin-by-bin to a common systematical uncertainty envelope. As the uncertainties are seen to be largely symmetric only a symmetrical uncertainty envelope is built. The resulting combined uncertainty per bin is shown in Fig. 9.6. Here the distributions of the A_{FB} in the signal Monte Carlo are plotted for the two selection channels. The statistical uncertainties of the signal samples and the individual contributions to the uncertainties are compared to the combined

uncertainty bands. This is done with respect to relative as well as the absolute contributions to the uncertainty.

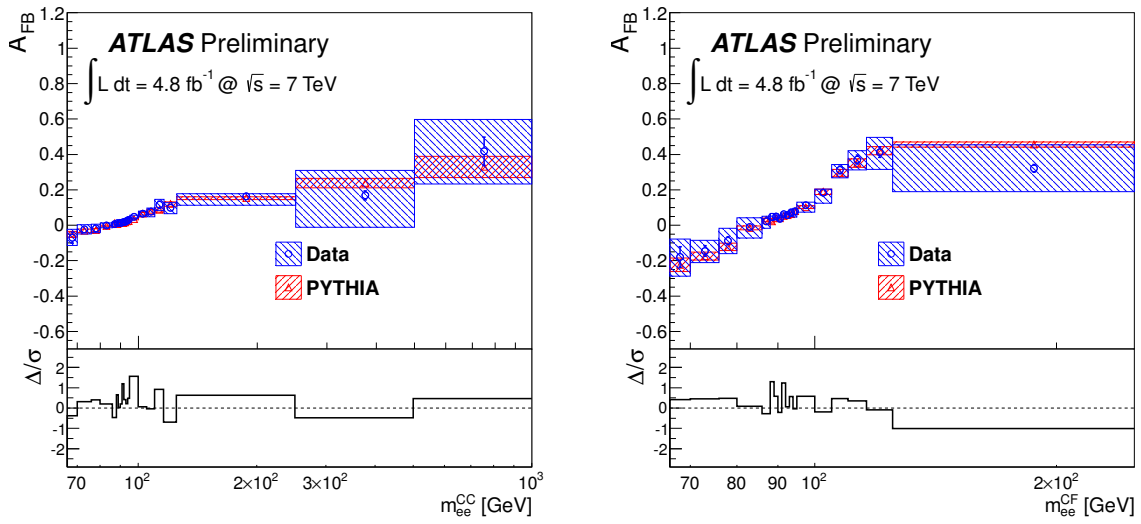

Figure 9.5.: Raw A_{FB} distributions for the CC (a) and CF (b) channel, after background subtraction. For the data, the boxed shaded region represents the total (statistical+systematic) uncertainty and the error bars represent the statistical uncertainty. The boxed shaded regions for the MC represent only the statistical uncertainty. The ratio plots at the bottom of each figure display the distribution of pulls (Δ/σ) for each A_{FB} distribution, where Δ is the difference between data and MC and σ is the quadratic sum of the data and MC uncertainties. Taken from [28].

9.4. Unfolding of detector effects

The raw distributions of A_{FB}, as discussed until now, are representing only a part of the spectrum of A_{FB} in the Z/γ^* process due to the kinematic and selection restrictions given with the detector and data taking setup. To be able to compare the distributions obtained from data to the predictions in theoretical calculations, it is a widely used approach to perform an unfolding with respect to the restrictions on the distributions. This was performed in the studies discussed in the Z/γ^* A_{FB} conference note [28] this analysis is also part of. The unfolding procedures described there are defined to treat different restrictions in the selected data:

First of all the principle detector effects as mass bin migration and the misidentification of the electron charges can be corrected for. Further the phase space restrictions in the lepton selection can be inter- and extrapolated to ease a comparison of different selection channels like the electron CC channel discussed in this analysis and a selection using muons from the same data sets that is also discussed in the Z/γ^* A_{FB} conference note. Then there is the possibility to extrapolate the analyses to the full phase space using the underlying signal Monte Carlo as reference and to correct the dilution arising from the choice of the (mis-)tagging of the initial quark direction in the hard process. The dilution correction discussed in [28] though is only the leading order (LO) interpretation of this effect as the event generator used is a LO choice for other reasons.

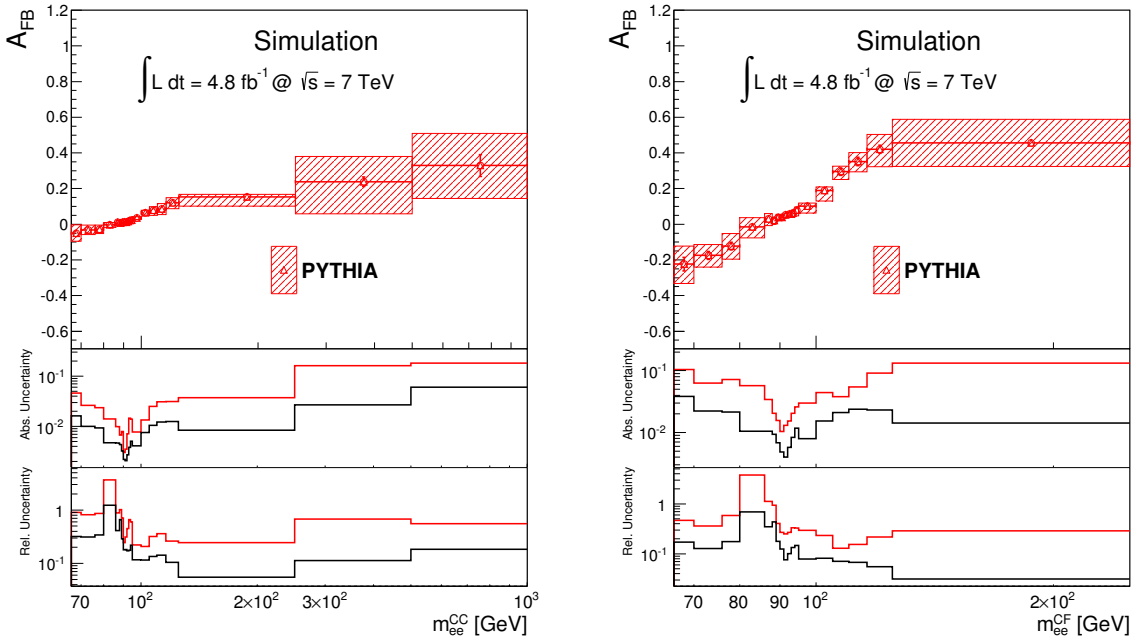

(a) (b)

Figure 9.6.: Impact of the systematical uncertainties with respect to the signal Monte Carlo A_{FB} distributions in the CC (a) and CF (b) channel. In the top most part ot the figures, the distributions of A_{FB} of the signal MC in the respective selection channel are shown including the error bands of statistical and systematical uncertainties. In the middle and bottom plots the absolute and relative size of the different contributions to the combined uncertainty bands are shown. It has to be considered that for values of the asymmetry close to zero the relative uncertainties can get exceptionally large where as the absolute amount of uncertainty to the respective bin is similar or even smaller compared to neighbouring bins in the same distributions.

9.4.1. Bayesian Unfolding

The unfolding routines in the studies discussed in [28] are using a Bayesian unfolding method. It is implemented in the RooUnfold toolkit [69], which is a collection of algorithms to consistently perform unfolding in a set of available methods.

The unfolding procedure is initialised by building an object called response matrix that relates the reconstructed or measured quantities of a simulated signal sample with its true quantities. These response objects can be either constructed by providing plain true and measured distributions and their correlation matrix to RooUnfold or by filling the response object directly from the correlated true and reco information of the simulated events into the RooUnfold response object. Here the events that contain both true and reconstruction information are directly filled into the matrix. The events that either do not have true or reconstructed information can be added to the matrix by adding so called miss and fake contributions to the response. Here it is let up to the use case whether and how the true quantities are selected and which acceptance requirements are used. The selected acceptance cuts are directly related to the available phase space, that the unfolding is trying to extrapolate data to. The modular structure of the RooUnfold implementation allows to switch between simple bin-by-bin unfolding, Bayesian unfolding and three

other approaches by just asking for the corresponding routines and schemes to be used in the unfolding step. This is discussed in the RooUnfold documentation [69].

In the Bayesian unfolding, as summarized by D'Agostini [70], Bayes' theorem, relating initial and conditional probabilities, can be used to perform an iterative inversion of the response matrix used in the unfolding.

9.4.2. Implementation of unfolding the A_{FB} distributions

The unfolding studied in [28] is performed using born level leptons. The unfolding working points are three different main goals: the correction of detector effects dominated by the mass bin migration but including charge mis-identification in the response, the additional extrapolation to the full phase space, and the final inclusion of the LO interpretation of a dilution correction on top of the other corrections. Here the statistical and systematical influences on the unfolding routine are taken into account by performing variations of the response matrices according to the systematic sources mentioned in Sec. 9.3 if applicable to the Monte Carlo. In case the variations are corrections, that are applied on data, the input to the unfolding is varied accordingly.

9.4.3. Results of the unfolded A_{FB} distributions

The distributions of A_{FB} with respect to the invariant di-electron mass is shown in Fig. 9.7 for the unfolded results with respect to the mass bin migration level, as well as the unfolding with respect to the full acceptance including the LO interpretation of the dilution. The unfolded line shapes of the background corrected data are in very good agreement with the truth line shapes from signal Monte Carlo.

The largest contributions to the systematic uncertainties are originating from the uncertainties of the unfolding method, that was determined in a fold-unfold closure test on the Monte Carlo, and the effects from the PDF variations. Especially the full unfolding, that includes the unfolding of the dilution effect, is largely depending on the PDF as well as on the underlying generator. In the CF channel the impact of the background modeling also yields a non-negligible contribution to the combined uncertainty. As it is only possible to consistently define the correction of the dilution on leading order diagrams, the quality of the interpretation depends on the implementation of the higher order effects into the LO setup.

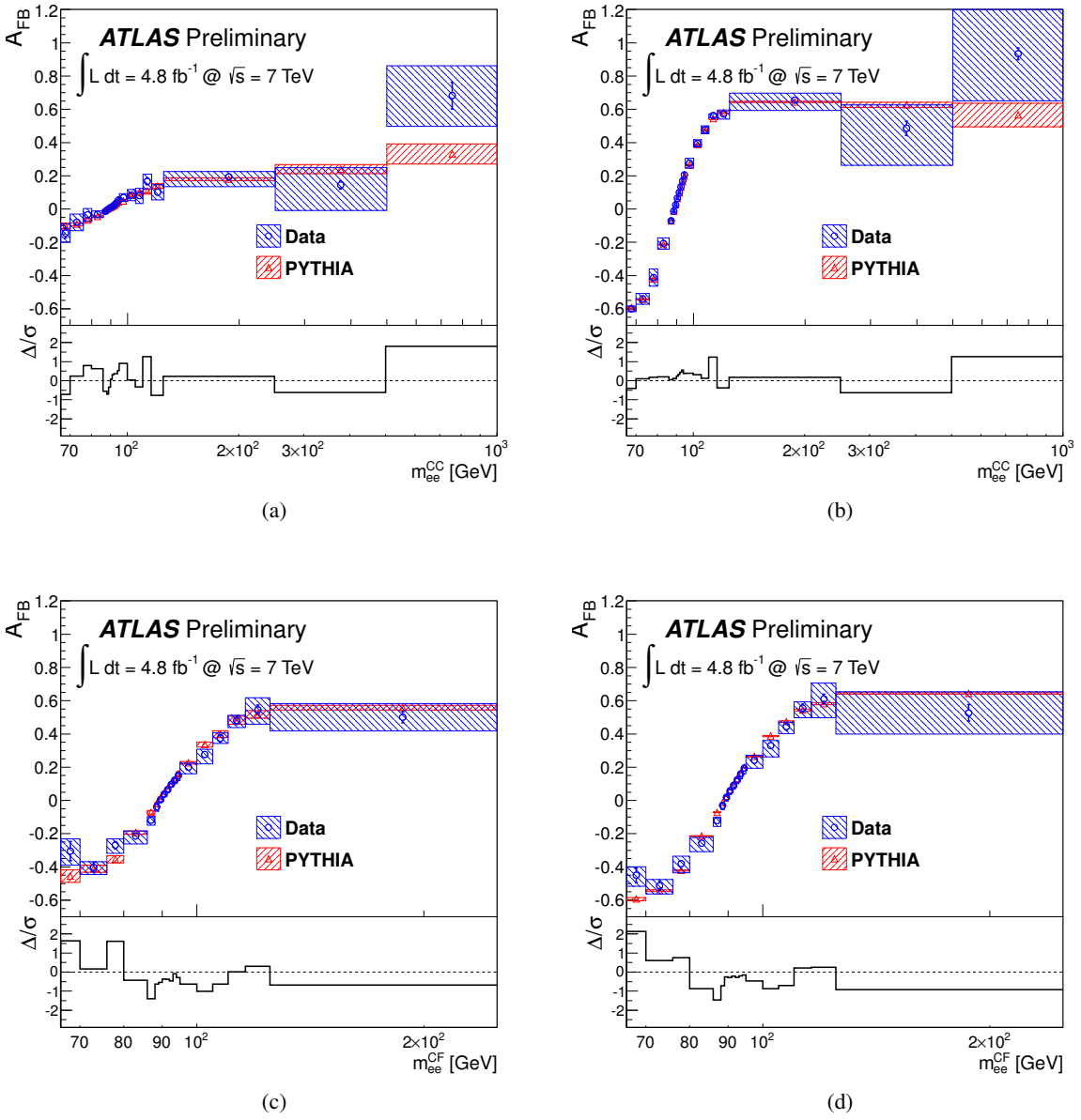

(a) (b)

(c) (d)

Figure 9.7.: A_{FB} distributions from the published note [28] after mass bin migration unfolding (a), (c) and after full unfolding including the dilution correction to the leading order interpretation (b), (d) in the CC (a), (b) and CF (c), (d) channel. The ratio plots at the bottom of each figure display the distribution of pulls (Δ/σ) for each A_{FB} distribution, where Δ is the difference between data and MC and σ is the quadratic sum of the data and MC uncertainties. Taken from [28].

10. Extraction of $\sin^2\theta_W^{\text{eff}}$ with the Template Method

This chapter describes the extraction of the fundamental parameter $\sin^2\theta_W^{\text{eff}}$ of the Standard Model from the raw A_{FB} distributions. This analysis is using a template based approach. In this approach Monte Carlo generated distributions of the A_{FB} spectrum are compared in χ^2 tests to the distribution in data. In these template distributions the parameter of the effective weak mixing angle $\sin^2\theta_W^{\text{eff}}$ is varied. In this setup the unfolding step is not necessary. Instead the raw distribution from data is compared to the generated samples after full detector simulation, which can be interpreted as forward folding technique. All events on the Monte Carlo samples have to fulfill the same selection requirements as the events in the raw data sample. To compare data to the signal Monte Carlo distributions, either the contributions in the data selection that do not originate from the signal process have to be subtracted from data or added to the signal distributions. As the choice for the unfolding study has a preference to correct the data distributions and as this also makes the computation easier for the template extraction, also in the extraction study with the template method the background contributions are subtracted from data. For that reason the treatment of this correction is the same as described in detail in Sec. 8 and Sec. 9.2.

The template extraction method is structured as follows:
The Monte Carlo templates are generated in the same setup as the signal Monte Carlo sample with the only respective difference of the value of the leading order weak mixing angle. From the templates the distributions of A_{FB} are built so that the line shapes can be compared to the line shape on data. The comparison is performed with χ^2 tests for each template. The best match of the value of the weak mixing angle (*wma*) from these templates to data can be extracted by fitting the results of the χ^2 tests with respect to their *wma* value by a parabolic function. The minimum of the parabola is therefore the best match, where as the width of the parabola at $\chi^2_{\text{min}} + 1$ can be used as the statistical uncertainty of the template comparison. This is explained in detail in Sec. 10.1. The influence of the chosen of the background samples, that are subtracted from data, is discussed in Sec. 10.3.1, while the impact of systematic variations as seen in Sec. 9.3 are described in Sec. 10.3. Finally in Sec. 10.4 the results are summarized and compared to previous measurements as well as the world average on the value of $\sin^2\theta_W^{\text{eff}}$.

10.1. Basics of the Template Method

As introduced above the extraction of the Standard Model parameter $\sin^2\theta_W^{\text{eff}}$ with the template method uses raw data and Monte Carlo distributions after a sensible selection on the reconstructed electrons in the events. The distributions in data are corrected for background contributions by selections on Monte Carlo and data driven samples. This is described in the previous chapters.

The background corrected data is compared to $Z \rightarrow ee$ signal Monte Carlo that is generated with different values of the *wma*. These comparisons consist of the calculation of the compatibility of the pairs of distributions in χ^2 tests. To create the different template Monte Carlo samples one approach would be to

generate a set of signal Monte Carlo samples with equal amount of statistics and perform the full detector simulation, reconstruction and selection on them. Because this procedure is consuming lots of time and resources, the template samples are built from generator level only samples, that are used to reweight the single official fully simulated signal Monte Carlo. This setup uses the official ATLAS software to build the generator level inputs for these templates. This is validated by the comparison of a reweighted template to a purposefully produced signal Monte Carlo both using a value of the weak mixing angle of 0.235. This validation is shown for the muon channel of the common analysis this thesis is sharing contributions with. It is shown that the two samples are agreeing in the A_{FB} distribution well within the statistical uncertainties [28].

The set of *wma* samples that is used to determine the weak mixing angle value in data is consisting of 19 generator level samples with a range from 0.218 to 0.236 in $\sin^2\theta_W^{\text{eff}}$, parametrised in the generator options. The samples are also generated with the PYTHIA event generator and use about 40 million events each. To change the *wma* in the PYTHIA configurations the command *pydat1 paru 102 wma* with weak mixing angle value $\sin^2\theta_W^{\text{eff}} = wma$ is adapted accordingly. The mentioned samples were produced on behalf of the common analysis [28] by Kristof Schmieden [71].

These generator level samples are used to build event maps in the distributions of $\cos\theta^*_{CS}$ and m_{ee} for true electron pairs originating from the generated Z-boson. Here the values of $\cos\theta^*_{CS}$ are defined with respect to the true incoming quark direction in LO interpretation of the PYTHIA events. Further the electrons are selected to match the born-level description of the generator output where the FSR has not yet changed the properties of the electrons. Depending on the channel these maps are selected for, acceptance requirements are applied on the electrons: For the CC channel both electrons have to be produced within the central detector acceptance $|\eta^{true}_{e_{1,2}}| < 2.5$ and their transverse momentum has to be at least $p_T^{true} > 25\,\text{GeV}$. The CF channel requirements are to keep events with one central and one forward electron according to $|\eta^{true}_{e_c}| < 2.5$ and $2.5 < |\eta^{true}_{e_f}| < 5$. Here also a minimum transverse momentum requirement of $p_T^{true} > 25\,\text{GeV}$ is applied.

For the reweighting procedure the maps are classified as *target (tar)* and *reference (ref)* maps where the *ref* map corresponds to the same *wma* value that is also used in the official signal Monte Carlo sample. These maps are now used to build maps of weight in the same binning as in the *tar* and *ref* maps. The weight maps are filled with the weights $w_{ij} = tar_{ij}/ref_{ij}$ where i and j denote the bin numbers in m_{ee} and $\cos\theta^*_{CS}$. The uncertainties δw_{ij} of these weight maps is calculated with respect to the statistical uncertainties in the input maps *tar* and *ref* by taking into account (10.1).

$$\delta w_{ij} = \sqrt{\left(\frac{\delta tar_{ij}}{ref_{ij}}\right)^2 + \left(\frac{tar_{ij}\cdot\delta ref_{ij}}{{ref_{ij}}^2}\right)^2}, \quad \delta tar_{ij} = \sqrt{tar_{ij}}, \quad \delta ref_{ij} = \sqrt{ref_{ij}} \tag{10.1}$$

With these weight maps the fully simulated signal sample can be reweighted to the correspondingly changed *wma* values. Here the statistical uncertainties of the weight maps are propagated to the reweighted templates. Also bin-by-bin migration between truth and reco in the fully simulated sample is taken into account. This is done by using the generator level quantities of the signal MC to gather the weight corresponding to the respective event. While the bin contents $f_{template}$ in the templates are filled by looping over the corresponding weights w_{ij} in the weight maps, the uncertainties in a given bin $\delta f_{template}$ is calculated by the quadratic sum of the weighted bin content and the sum over all contributing weights:

$$\delta f_{template} = \sqrt{\left(\sum_{k=1}^{n}\delta w_k\right)^2 + \left(\bar{w}\,\sqrt{n}\right)^2}. \tag{10.2}$$

Here n is the number of events, w_k the weight of event k and $\bar{w}$ the average weight of events in the corresponding bin. As the weights being added are highly correlated their uncertainties are added linearly.

Additionally it is recommended for this treatment to reweight the PDF used in these templates to the central PDF of the *MSTW2008LO* PDF set [68].

It is shown in Fig. 10.1 that the reweighting in *wma* does not affect the mean of the invariant mass distributions of the template samples.

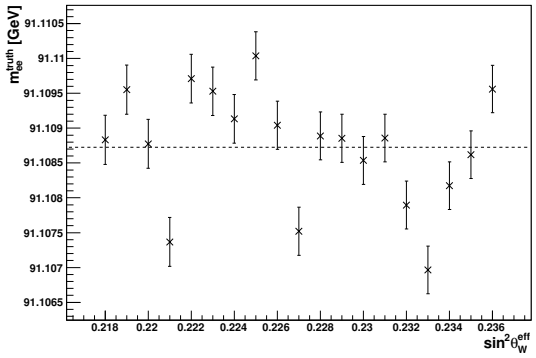

Figure 10.1.: Truth mean di-electron invariant mass in the mass range 80 GeV to 100 GeV for different values of $\sin^2\theta_W^{\text{eff}}$. No systematic change of the Z mass with respect to $\sin^2\theta_W^{\text{eff}}$ is visible. The distributions mean values are obtained from corresponding weight map inputs with truth quantities that are used in the extraction of the CC channel.

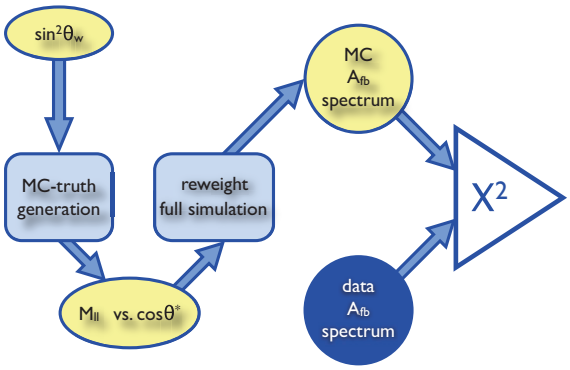

Figure 10.2.: Schematic overview of the extraction of the weak mixing angle using MC templates. Taken from CERN-THESIS-2012-332 [71][1].

The A_{FB} distributions, that are built from the template samples, can now be compared to background corrected data distributions in the range of 70 – 250 GeV separately for CC and CF channel. This is done by the previously introduced calculation of χ^2 tests, as described in (10.3) for the combination of the template j and the to be tested distribution referred to as *probe*.

$$\chi^2_j = \sum_{i=1}^{N} \frac{\left(probe_i - template_{ij}\right)^2}{\sigma(probe)_i^2 + \sigma(template)_{ij}^2 + \sigma(systematic)_i^2} \tag{10.3}$$

Here N is the number of bins in the A_{FB} spectrum ($N = 17$) and $\sigma(probe_i)$ ($\sigma(template_{ij})$) corresponds to the uncertainty on the asymmetry in the i-th mass bin for the corresponding *probe* (*template*$_j$) sample. The *probe* sample can be either the measured and background corrected distribution from data or a sample of modified signal Monte Carlo input. The contributions denoted with *template* are always the reweighted Monte Carlo templates, that contain the variation in $\sin^2\theta_W^{\text{eff}}$. The statistical uncertainties of the *probe* (*template*$_j$) sample in the bins are calculated by

$$\sigma = \frac{2}{(f+b)^2}\sqrt{(f\cdot\delta b)^2 + (b\cdot\delta f)^2}, \tag{10.4}$$

[1]This figure is yet an unofficial update from the internal supporting note and draft of the public document to the figure shown based on Figure 6.5 of the ATLAS thesis by Kristof Schmieden [71].

where f (b) is the number of forward (backward) event and $\delta f(b)$ is the corresponding uncertainty in the selected mass bin. This is a only using gaussian error propagation of the uncertainties to the asymmetry calculation formula (2.3.8) defined in Sec. 2.3. Additionally systematic uncertainties can also be taken into account in this calculation. This is done in Sec. 10.3 to derive the impact of systematical variations on the extracted *wma* values. In Fig. 10.2 the schematic flow of this extraction setup is summarized. The resulting χ^2 results of 19 templates can be histogramised with respect to the corresponding value of $\sin^2\theta_W^{\text{eff}}$ and fitted by a parabolic function:

$$\chi^2(x) = a + b \cdot (x - c)^2. \tag{10.5}$$

Here the mean of the polynomial c is the central value of this extraction, whereas the width is obtained by reading off the width $w = x_2 - x_1$ of the parabola with $\chi^2(x_{1,2}) = \chi^2_{min} + 1$. This width is related to the fit uncertainty $\sigma = \frac{w}{2}$. When only taking into account the statistical uncertainties of either the *probe* or *templates*, this uncertainty can be interpreted as the statistical uncertainty of the respective source. If also the systematical uncertainties are used the combined uncertainty can be read off.

10.2. Closure Test and Extraction of $\sin^2\theta_W^{\text{eff}}$

With the extraction scheme discussed above firstly the consistency of the method has to be shown. This closure test is using either the unmodified A_{FB} distribution of the signal MC or the central template corresponding to the *wma* value of 0.232 as *probe* distribution in the extraction as pseudo data. This is shown in Fig. 10.3 comparing the unweighted signal Monte Carlo distribution to the set of templates. The extracted values for the *wma* are close to the default value of 0.232. In the CC channel the agreement is better than in the CF channel. Here the same result is achieved using the *probe* template with the PYTHIA default value or the unweighted signal MC. Also there is only a small variation in the impact of the fitted uncertainty when either using the statistical uncertainties of only the *probe* or only the *template* in the fit. These errors are used further as the statistical uncertainties due to the templates and the statistics of the signal Monte Carlo. For the CC and CF channel the values obtained for the minimum of the χ^2 parabola is well below the number of degrees of freedom in this extraction. This is because the templates and the *probe* distribution are highly correlated.

In Fig. 10.4 the background corrected data distribution is used to extract the nominal values for $\sin^2\theta_W^{\text{eff}}$ as well as the statistical uncertainty of the data distribution. The data statistics error is derived by only taking the statistical uncertainty of the data sample into account when performing the extraction. The quadratic sum of the individually extracted statistical uncertainties of the data distribution and of the Monte Carlo uncertainty in the templates is consistent with the values of the combined statistical error, when using both sources of uncertainty in the same fit.

10.3. Systematics in $\sin^2\theta_W^{\text{eff}}$ extraction

Systematic uncertainties on the *wma* are evaluated by using the A_{FB} distributions with the respective variations as *probe* in the extraction and calculating the difference to the default result. Alternatively the systematic variations can be extracted by using the systematics term in (10.3) to take into account additional systematic uncertainties and subtract the nominal statistical uncertainty quadratically from the combined uncertainty.

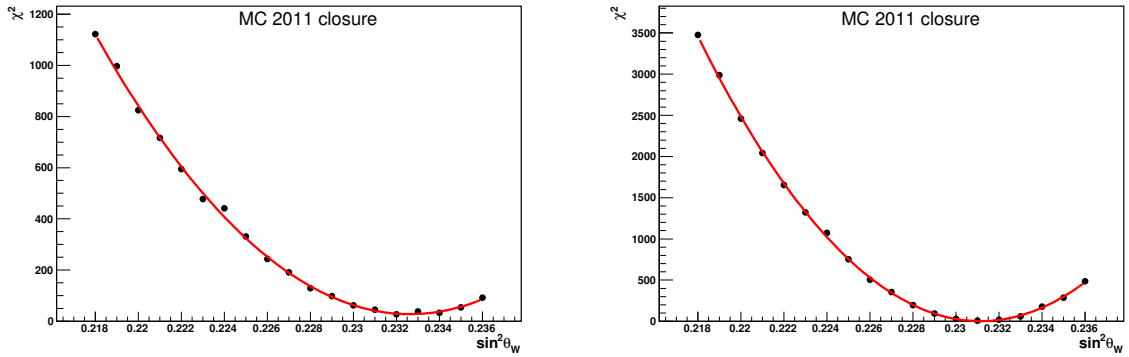

(a) (b)

Figure 10.3.: Closure spectra of the Z/γ^* candidates in the CC (a) and CF (b) channel.

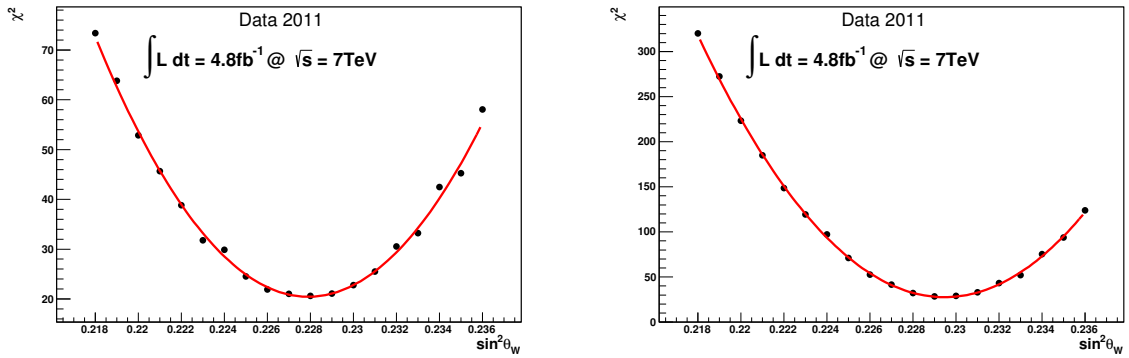

(a) (b)

Figure 10.4.: Extraction spectra of the Z/γ^* candidates in the CC (a) and CF (b) channel. The extraction in these figures only uses statistical uncertainties of data.

10.3.1. Backgrounds in $\sin^2\theta_W^{\text{eff}}$ extraction

The systematic variations of the background samples, that are discussed with respect to the A_{FB} distributions in Sec. 9.3.3, are also evaluated in the extraction of $\sin^2\theta_W^{\text{eff}}$. The samples that contribute are

1. Electroweak single boson production
2. Electroweak Diboson production
3. $t\bar{t}$ production
4. QCD processes with light jets and electrons in the final state.

Here the electroweak and $t\bar{t}$ contributions are grouped and referred to as "EW" backgrounds in the following.

The impact of a background contribution to the systematic uncertainty is evaluated by omitting the sample(s) the background correction of data. As this is overestimating the systematic uncertainty on the single contributions, the background correction uncertainty for the Monte Carlo based backgrounds is estimated by 10% of the variation. This is still a conservative estimate on the cross section uncertainty on the respective samples. To evaluate the contribution of the $W \to e\nu$ background specifically, which was a requested cross check for the ATLAS internal documentation, this background is varied in addition also by ±100% in the CC channel. This contribution is additionally added to the combined background uncertainty but does not have a sizable impact.

The uncertainty due to the variation of the multijet background is also taken into account for the systematic uncertainty by treating the variation due to the omission of the respective contribution by 10%. As discussed above the correction of the multijet contribution is providing a dilution correction only. This is due to the fact that the multijet background is flat in terms of A_{FB}, as explained in Sec. 9.3.3.

The tables 10.1 and 10.2 list the different contributions to the propagated systematic uncertainty on the background correction. The effects listed there are the fitted values of $\sin^2\theta_W^{\text{eff}}$ as well as the full deviation with respect to the default A_{FB} distribution with all background corrections applied. Additionally in Tab. 10.2 the variation due to the alternative background correction is shown. This variation gives negligible difference to the default multijet template. Therefore the total systematic uncertainty is estimated by using 10% of the effect of the omission of the multijet background corrections ($18 \cdot 10^{-5}$).

Backgrounds used in correction	fitted $\sin^2\theta_W^{\text{eff}}$	difference to fully corrected data
no correction	0.22811	$23 \cdot 10^{-5}$
all but multijet	0.22791	$4 \cdot 10^{-5}$
all but EW	0.22805	$18 \cdot 10^{-5}$
all but $W \to e\nu$	0.22786	$-0.8 \cdot 10^{-5}$
all plus $W \to e\nu$	0.22789	$1.4 \cdot 10^{-5}$
All	0.22787	–

Table 10.1.: Impact of background subtraction on the extracted $\sin^2\theta_W^{\text{eff}}$ value in the electron CC channel.

Backgrounds used in correction	fitted $\sin^2\theta_W^{\text{eff}}$	difference to fully corrected data
no correction	0.23165	$218 \cdot 10^{-5}$
all but multijet	0.23123	$176 \cdot 10^{-5}$
all but EW	0.22914	$-34 \cdot 10^{-5}$
EW and alternative multijet	0.22938	$-9 \cdot 10^{-5}$
only alternative multijet	0.22872	$-75 \cdot 10^{-5}$
All	0.22947	–

Table 10.2.: Impact of background subtraction on the extracted $\sin^2\theta_W^{\text{eff}}$ value in the electron CF channel.

10.3.2. Systematic PDF uncertainty in $\sin^2\theta_W^{\text{eff}}$ extraction

In most cases both strategies of the calculation of the systematic uncertainty result similar results. This is not the case for the uncertainties due to PDF variation. Here the individually varied distributions have a too high influence on the slope of the A_{FB} line shape. For this reason the calculation of the PDF uncertainty in the $\sin^2\theta_W^{\text{eff}}$ extraction is required to take all distributions of the eigenvector variations into account as *probe* in the χ^2 fits. The related uncertainty of the PDF has to be determined from the variation of the final quantity, calculated by taking into account every variation of the corresponding PDF eigenvectors. The results of these pseudo data extractions of the PDF varied Monte Carlo distributions are plotted in Fig. 10.5. Using the PDF variations of the A_{FB} distribution to build an uncertainty envelope that is fed into the *wma* extraction leads to a drastic underestimation of the systematic impact on the value for $\sin^2\theta_W^{\text{eff}}$.

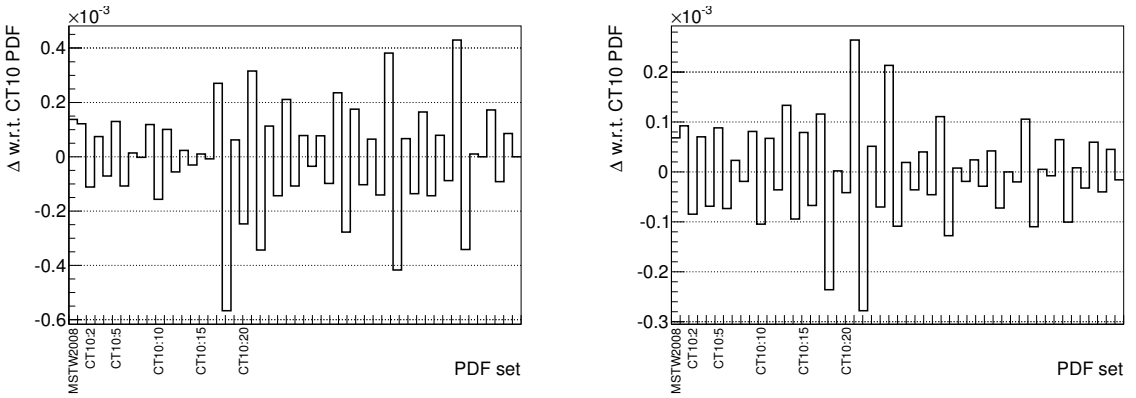

(a) (b)

Figure 10.5.: Impact of variations to the central *MSTW2008LO* and all *CT10* PDF sets in CC (a) and CF (b) channel. The first bin contains the difference found in $\sin^2\theta_W^{\text{eff}}$ between using the default *MSTW2008LO* and the central PDF of the *CT10* set in the CC (a) and CF (b) channel. All other bins show the difference between the 90% CL up / down variation of the 26 eigenvectors and the central PDF of the *CT10* PDF set.

The PDF variations of the *CT10* PDF, as discussed in Sec. 9.3.2, are evaluated at 90% CL, whereas all other uncertainties are corresponding to 1σ and correspond to 68% CL uncertainties. The resulting PDF systematic uncertainty is scaled by $\frac{1}{1.64}$ to get 1σ correspondent uncertainties as recommended in [37].

Systematic uncertainty	Deviation [10^{-5}]
PDF	91
Energy Scale	35
Energy Smearing	42
Electron scale factors	1
Pile-up	8
Background	3
MC statistics	47
EWK HO corrections	6
QCD HO corrections	32
Total	121

Table 10.3.: CC channel systematic uncertainty results.

Systematic uncertainty	Deviation [10^{-5}]
PDF	46
Energy Scale	57
Energy Smearing	45
Electron scale factors	4
Pile-up	5
Background	18
MC statistics	23
EWK HO corrections	6
QCD HO corrections	10
Total	92

Table 10.4.: CF channel systematic uncertainty results.

10.3.3. Summary of systematic uncertainties in $\sin^2\theta_W^{\text{eff}}$ extraction

Taking all known sources of systematic variations into account, the combined error on the extracted values for $\sin^2\theta_W^{\text{eff}}$ in the two analysis channels can be added up quadratically. This is because the sources of systematic variations are expected to be uncorrelated. The contributions to the combined systematical uncertainties are listed in Tab. 10.3 for the CC channel results and in Tab. 10.4 for the CF channel results.

Aside the statistical uncertainty of data, the dominating uncertainties are the variations of the PDF eigenvectors and the influence of the energy scale and resolution uncertainties. The systematic uncertainty due to the limited statistics of the signal Monte Carlo were already reduced by about a factor two by increasing the statistics of the *wma* template inputs as well as the fully simulated signal sample by a factor four in the number of events. Further the uncertainties due to the estimate of higher order corrections in additional EW and QCD contributions to the signal process are at least in the CC channel also providing a non-negligible contribution to the overall systematic uncertainty.

10.4. Results

The extracted value of the weak mixing angle from the CC channel is:

$$\sin^2\theta_{W\,CC}^{\text{eff}} = 0.2279 \pm 0.0009(stat.) \pm 0.0012(syst.) = 0.2279 \pm 0.0016(tot.)$$

and from the CF channel is:

$$\sin^2\theta_{W\,CF}^{\text{eff}} = 0.2295 \pm 0.0007(stat.) \pm 0.0009(syst.) = 0.2295 \pm 0.0011(tot.).$$

The results above, already in the early point in terms of the lifetime of a LHC experiment, are limited in precision by the influences of systematic uncertainties.

When combining the two measurements the impact of the statistical and some systematical uncertainties can be reduced. All systematics are treated as fully correlated uncertainties except the error from MC statistics and the uncertainties derived from varying the energy scale and smearing corrections.

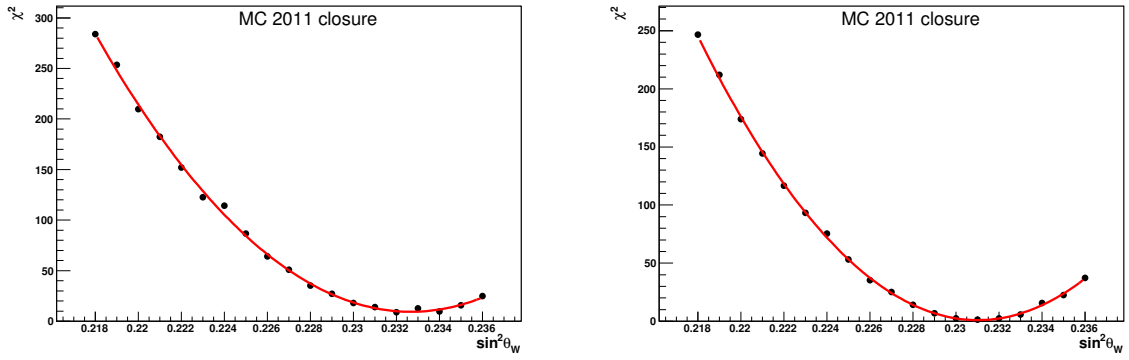

(a) (b)

Figure 10.6.: Closure with systematic uncertainties on the spectra of the Z/γ^* candidates in the CC (a) and CF (b) channel.

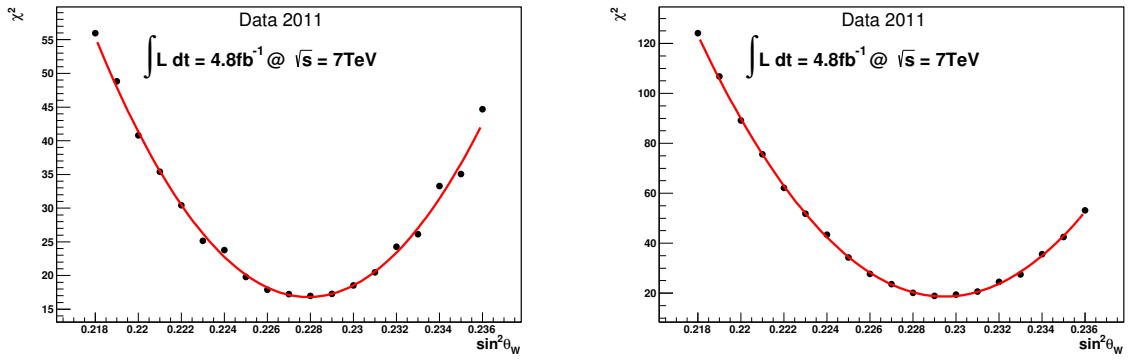

(a) (b)

Figure 10.7.: Extraction with systematic uncertainties on the spectra of the Z/γ^* candidates in the CC (a) and CF (b) channel.

Following this procedure, a combined (CC + CF) result is obtained:

$$\sin^2\theta^{\text{eff}}_{W\,comb} = 0.2288 \pm 0.0004(stat.) \pm 0.0009(syst.) = 0.2288 \pm 0.0010(tot.).$$

The dominating systematics are the uncertainties derived from the PDF eigenvector variations. Subleading contributions are the variations due to the energy calibration as well as the statistical limitations on the signal Monte Carlo.

10.4.1. Comparison to previous experimental results

As introduced in Sec. 2.3.2 the current precision of the world average in the measurement of the weak mixing angle is dominated by the measurements of the LEP and SLC experiments. These experiments used electron-positron colliders to produce "clean" samples of Z-events at varying center of mass energies around the Z resonance. This way energy scale uncertainties have very low influence on the measurement. Further the influence of PDF is not present as well the effect of dilution in the initial state. The estimate of background contributions and identification systematics is largely depending on the individual analysis channel. On the other hand the purity of the polarisation of the electron beams used at the SLC as well as the b quark identification and the different value of the effective weak mixing angle for processes including quarks - and especially b quark vertices as introduced in Sec. 2.3.2 - have to be added to the systematic sources of uncertainties, that are not used in the analysis of this thesis.

Comparing the combined result from the LEP and SLC experiments to the previously mentioned results of this thesis, the extracted values of $\sin^2\theta_W^{\text{eff}}$ differ by about 1.8 to 2.7 standard deviations from the previous result depending on the channel. On the other hand the results obtained in this study are in perfect agreement with the central value of the result obtained by the CMS experiment. This result shows an almost identical offset with respect to the world average but is derived with less data using a different extraction method. Therefore the difference in terms of standard deviations is smaller than one only because of the resulting combined uncertainty of the CMS result.

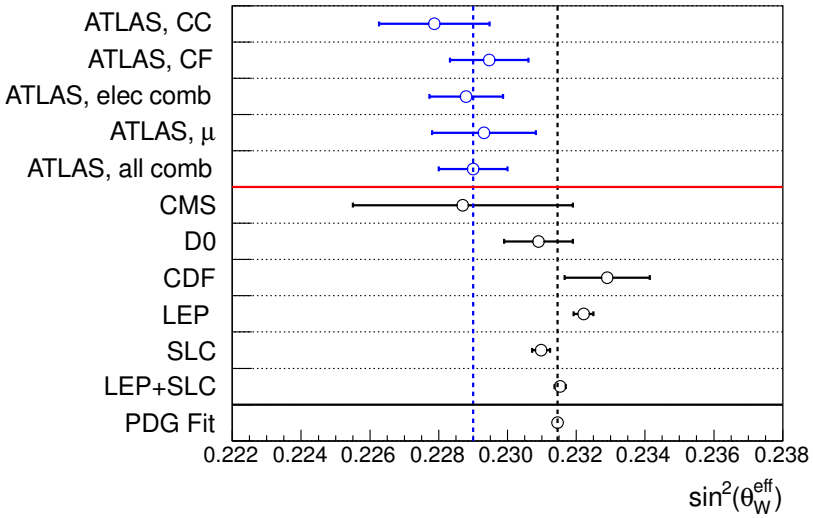

Figure 10.8.: Comparison of the PDG global fit expectation of $\sin^2\theta_W^{\text{eff}}$ and different experimental results.

Source	$\sin^2\theta_W^{\text{eff}}$	Δ/σ (w.r.t. LEP/SLC)	Δ/σ (w.r.t. ATLAS comb.)	Δ/σ (w.r.t. ATLAS electrons comb.)
ATLAS, electrons CC	0.2279 ± 0.0016	-2.3	–	–
ATLAS, electrons CF	0.2295 ± 0.0011	-1.8	–	–
ATLAS, electrons comb.	0.2288 ± 0.0010	-2.7	–	–
ATLAS, muons	0.2293 ± 0.0015	-1.5	–	–
ATLAS, combined	0.2290 ± 0.0010	-2.5	–	–
CMS [42]	0.2287 ± 0.0032	-0.9	-0.1	≤ ±0.1
D0 [27]	0.2309 ± 0.0010	-0.6	1.3	1.5
CDF [24]	0.2329 ± 0.0012	1.1	2.4	2.6
LEP [17]	0.23221 ± 0.00029	–	3.1	3.3
SLC [17]	0.23098 ± 0.00026	–	1.9	2.1
LEP+SLC [17]	0.23153 ± 0.00016	–	2.5	2.7
PDG global fit [32]	0.23146 ± 0.00012	-0.4	2.4	2.6

Table 10.5.: Comparison of the $\sin^2\theta_W^{\text{eff}}$ results with different experiments and the PDG global fit. Discrepancies with respect to the LEP/SLC combination and the present results are shown as well.

11. Summary and Outlook

The Standard Model (SM) of particle physics is a very successful and consistent theoretical parametrisations of the relation of three of the four fundamental forces and the particles at the sub-atomic scale. It is based on the gauge invariant formalisation of the fundamental interactions of bosons to the fermions that make up the known matter. The SM has been tested in various precision experiments and was found to be consistent with their results. On the other hand the SM as we know it is assumed to only stand as an effective theory of other more fundamental relations with respect to those that are currently included. For example there are still the missing description of gravity, the unification of more than two forces and the inclusion of the experimentally derived properties of cosmology. These cosmological measurements imply, that the part of the known universe, which is described by the Standard Model, only describes less than five percent of the overall energy content. The remaining parts are expected to be filled up by Dark Matter and Dark Energy.

The precision of the predictions made by the SM within its regime is unprecedented by theories of similar complexity. Because of this it has to be checked experimentally by improving the precision on key parameters of the SM if there are deviations showing up, that could give a hint towards some of the expected expansions to the SM. One of the precision tests of the Standard Model can be performed on the mixing parameter in the electroweak theory that relates the neutral current interactions of electromagnetism and weak force. Further it relates in lowest order of perturbation theory the masses of the charged and neutral boson of the weak force. In this thesis the weak mixing angle $\sin^2\theta_W^{\text{eff}}$ is extracted from the asymmetry between fermions and anti-fermions in the electroweak neutral current interaction, the forward backward asymmetry (A_{FB}). The A_{FB} is defined upon the distribution of the polar angle between the incoming quark (not anti-quark) and outgoing electron (e^-). The process of $pp \to Z/\gamma^* + X \to e^+e^- + X$ is studied in two distinct regions of phase space.

Starting with a symmetric initial state, with respect of the probability of the direction of the incoming quarks and anti-quarks of the colliding protons, the reference direction of the decay angle θ of the electron with respect to the incoming quark is not determinable. The missing information leads to a dilution of the spectra of A_{FB}. The probability to correctly tag the direction of the incoming quark is correlated with the longitudinal boost of the massive exchange boson. A high proton momentum fraction of an initial quark is propagated to the boost of the Z boson. If the invariant mass of the quark-anti-quark pair in the initial state is close to the Z mass, the anti-quark has to have a low proton momentum fraction.To take advantage of this correlation, one is obliged to take into account final state electrons, that are boosted to the highest detectable rapidities, while taking care of the signal purity. On the other hand on at least one of the electrons in the pair the charge has to be measurable to tag the event to be either forward or backward.

One option, that was chosen in this study, is to define the default channel using both electrons from the central region of the ATLAS detector (CC). These electrons are passing the tracking system, that provides the charge information. The accessible reach of boson rapidities in this channel is limited by the acceptance of the tracking system though. The other choice is to take one electron with charge information in the central region and pair it with a second electron from the forward region (CF). This way the reach in boson rapidity in increased and effect of dilution is reduced. The charge information

is still accessible and the probability of charge mis-identification is studied and shown to be negligible.

To include the forward electrons in the analysis, the energy scale of the forward region had to be re-calibrated. This was done in an inter-calibration attempt, using the central electron energy scale and pairs of central and forward electrons at the Z resonance as reference. In this setup the systematical uncertainty due to the central electron energy calibration as well as the systematical uncertainties due to the inter-calibration method and other data uncertainty dependencies like pile-up are taken into account.

The analysis was performed with an integrated luminosity of $\int \mathcal{L}\,\mathrm{dt} = 4.8\,\mathrm{fb}^{-1}$ collected in pp collisions at $\sqrt{s} = 7\,\mathrm{TeV}$. It is using a forward folding technique to prepare template distributions with varied values of the weak mixing angle to perform a χ^2 test based extraction. As systematic uncertainties several sources have been taken into account. The dominating sources are introduced by the current knowledge of the PDF that has a strong impact on the precision. One other dominant uncertainty is the estimated from the variation within the electron energy calibration, especially in the CF channel. The fact that the forward electron energy calibration was derived, taking the calibration of the central electron energies as input, leads to the need of propagating all known uncertainties through. The uncertainties of the central electron energy calibration as well as the variation in conditions of simultaneous interactions (pile-up) on the forward electron energy calibration were taken into account in this uncertainty. Therefore the full uncertainty had to be added to the extraction of the weak mixing angle in the CF channel. Subdominant uncertainties that are taken into account for the extraction are containing variations in the electron dependent scale factors, the pile-up conditions as well as the level of background contributions taken into account in the event selection.

The extractions in the two channels yield values for $\sin^2\theta_W^{\mathrm{eff}}$ of:

$$\sin^2\theta_{W\,CC}^{\mathrm{eff}} = 0.2279 \pm 0.0009(stat.) \pm 0.0012(syst.) = 0.2279 \pm 0.0016(tot.)$$

in the CC channel and:

$$\sin^2\theta_{W\,CF}^{\mathrm{eff}} = 0.2295 \pm 0.0007(stat.) \pm 0.0009(syst.) = 0.2295 \pm 0.0011(tot.)$$

in the CF channel.
The combination of the results above yields:

$$\sin^2\theta_{W\,comb}^{\mathrm{eff}} = 0.2288 \pm 0.0004(stat.) \pm 0.0009(syst.) = 0.2288 \pm 0.0010(tot.).$$

This is comparable or better than the precision currently published by the Tevatron experiments. The Tevatron results are limited in precision by the statistics available to the experiments, while the results discussed above are suffering from the limitations due to systematical variations. These results further are more precise than the results found by the CMS Collaboration, using muon events with less statistics and a slightly different extraction approach.

Current plans for analyses on the data collection period 2012 are to derive the so called angular moments, that are in a way related to the A_{FB}. These moments are taking in addition to the cosine of the decay angle in a reference frame, e.g. the Collins-Soper frame that was used in this study, and also the azimuthal angle and correlations between polar and azimuthal angles into account. With this set of parameters further constraining of parton distribution functions can be performed, which are seen to be limiting the current precision of the weak mixing angle extraction. The prospects towards the measurement of A_{FB}

and $\sin^2\theta_W^{\text{eff}}$ in data taken after the long shutdown in 2015 is also not as straight forward as just redoing the study presented above. The proposed conditions of data taking from 2015 on imply that the level of simultaneous interactions is increasing drastically. Therefore the inclusion of the channel that uses forward electrons is problematic in that respect that the level of background contributions to the selection will increase, while the signal and background separation will worsen. This of course assumes that there will not be major updates to the detector. Additionally it is possible that the trigger thresholds for single electron signatures will have to be prescaled. Alternative unprescaled single electron triggers are expected to require very high thresholds in p_T. On the other hand it is foreseen to study to expand the reach of the trigger and tracking system towards higher rapidities of about $|\eta| = 2.8$ or 3.2. This would increase the accessibility of charge measurement as well as more powerful signal to background separation. Unfortunately these updates are only proposed so far and will not be installed before about 2017 into the ATLAS detector. It is expected to slowly increase the precision on the weak mixing angle determination with more measured events on the one hand and better understanding, experience in modeling of the experimental and theoretical uncertainties on the other.

On top of the measurement at the Z boson resonance the potential appearance of an additional very heavy weak neutral gauge boson like a Z' is expected to be visible in the distribution of A_{FB} with respect to the invariant mass of the final state. A deviation of the measured and background corrected line shape of the A_{FB} distribution from the expected saturation at high invariant masses would imply an indirect contribution of such a new physics process. If a resonance as predicted by the various Z' models could be found, also the running of the weak mixing angle at scales above the Z resonance could be performed. On the low end of the spectrum of accessible scales μ the proposed experiments to study the weak mixing angle at electron - proton scattering e.g. at the MESA facility in Mainz could further increase the precision on the value of the weak mixing angle. Each of these direct measurements in resonant production at LHC or at MESA are in the long run expected to be able to reach or surpass the precision of the two most precise results achieved by the LEP and SLC experiments and their combined result. This can be achieved by progressing understanding of the detector performance as well as more advanced background separation techniques for the LHC experiments. Also the predictions of higher order corrections to the process at MESA as well as the inclusion of LHC data into new PDFs for the ATLAS and CMS measurements are expected to yield better estimates of the related uncertainties.

Bibliography

[1] M. Gell-Mann, *A schematic model of baryons and mesons*, Physics Letters **8** (1964) 214 – 215. http://www.sciencedirect.com/science/article/pii/S0031916364920013.

[2] V. E. Barnes et al., *Observation of a Hyperon with Strangeness Minus Three*, Phys. Rev. Lett. **12** (Feb, 1964) 204–206. http://link.aps.org/doi/10.1103/PhysRevLett.12.204.

[3] TASSO Collaboration, R. Brandelik et al., *Evidence for planar events in e+e annihilation at high energies*, Physics Letters B **86** (1979) 243 – 249. http://www.sciencedirect.com/science/article/pii/037026937990830X.

[4] PLUTO Collaboration, C. Berger et al., *Evidence for gluon bremsstrahlung in e+e annihilations at high energies*, Physics Letters B **86** (1979) 418 – 425. http://www.sciencedirect.com/science/article/pii/0370269379908694.

[5] JADE Collaboration, W. Bartel et al., *Observation of planar three-jet events in e+e annihilation and evidence for gluon bremsstrahlung*, Physics Letters B **91** (1980) 142 – 147. http://www.sciencedirect.com/science/article/pii/0370269380906802.

[6] MARK Collaboration, D. P. Barber et al., *Discovery of Three-Jet Events and a Test of Quantum Chromodynamics at PETRA*, Phys. Rev. Lett. **43** (Sep, 1979) 830–833. http://link.aps.org/doi/10.1103/PhysRevLett.43.830.

[7] UA1 Collaboration, G. Arnison et al., *Experimental Observation of Lepton Pairs of Invariant Mass Around 95 GeV/c^2 at the CERN SPS Collider*, Phys.Lett. **B126** (1983) 398–410.

[8] UA2 Collaboration, P. Bagnaia et al., *Evidence for $Z^0 \to e^+e^-$ at the CERN $p\bar{p}$ Collider*, Phys.Lett. **B129** (1983) 130–140.

[9] CDF Collaboration, F. Abe et al., *Observation of Top Quark Production in $p\bar{p}$ Collisions with the Collider Detector at Fermilab*, Phys. Rev. Lett. **74** (Apr, 1995) 2626–2631, arXiv:hep-ex/9503002.

[10] D0 Collaboration, S. Abachi et al., *Search for High Mass Top Quark Production in $p\bar{p}$ Collisions at $\sqrt{s} = 1.8$ TeV* , Phys. Rev. Lett. **74** (Mar, 1995) 2422–2426, arXiv:hep-ex/9411001.

[11] CDF and D0 Collaboration, Tevatron Electroweak Working Group, *2012 Update of the Combination of CDF and D0 Results for the Mass of the W Boson*, arXiv:1204.0042 [hep-ex].

[12] ALEPH Collaboration, D. Buskulic et al., *Performance of the ALEPH detector at LEP*, Nucl.Instrum.Meth. **A360** (1995) 481–506.

[13] DELPHI Collaboration, P. Aarnio et al., *The DELPHI detector at LEP*, Nucl.Instrum.Meth. **A303** (1991) 233–276.

[14] L3 Collaboration, *The Construction of the L3 Experiment*, Nucl.Instrum.Meth. **A289** (1990) 35–102.

[15] OPAL Collaboration, *The OPAL detector at LEP*, Nuclear Instruments and Methods in Physics Research Section A: Accelerators, Spectrometers, Detectors and Associated Equipment **305** (1991) no. 2, 275 – 319. http://www.sciencedirect.com/science/article/pii/0168900291905474.

[16] SLD Collaboration, *SLD DESIGN REPORT*, 1984.

[17] The ALEPH, DELPHI, L3, OPAL, SLD Collaborations, the LEP Electroweak Working Group, the SLD Electroweak and Heavy Flavour Groups, *Precision electroweak measurements on the Z resonance*, Phys.Rept. **427** (2006) 257–454, arXiv:hep-ex/0509008 [hep-ex].

[18] P. W. Higgs, *Broken symmetries, massless particles and gauge fields*, 1964. Phys. Lett. **12** (1964) 132–133. Phys. Lett. 12 (1964) 132.

[19] ATLAS Collaboration, *The ATLAS Experiment at the CERN Large Hadron Collider*, JINST **3** (2008) S08003.

[20] CMS Collaboration, *The CMS Experiment at the CERN LHC*, JINST **3** (2008) S08004.

[21] ATLAS Collaboration, *Observation of a new particle in the search for the Standard Model Higgs boson with the ATLAS detector at the LHC*, Physics Letters B **716** (2012) 1–29. http://www.sciencedirect.com/science/article/pii/S037026931200857X.

[22] CMS Collaboration, *Observation of a new boson at a mass of 125 GeV with the CMS experiment at the LHC*, Physics Letters B **716** (2012) 30–61. http://www.sciencedirect.com/science/article/pii/S0370269312008581.

[23] Nobelprize.org. Nobel Media AB 2013, *"The 2013 Nobel Prize in Physics - Press Release"*, Oct, 2013. http://www.nobelprize.org/nobel_prizes/physics/laureates/2013/press.html.

[24] CDF Collaboration, D. Acosta et al., *Measurement of the forward-backward charge asymmetry of electron positron pairs in $p\bar{p}$ collisions at $\sqrt{s} = 1.96$ TeV*, Phys.Rev. **D71** (2005) 052002, arXiv:hep-ex/0411059 [hep-ex].

[25] CDF Collaboration, T. Aaltonen et al., *First Measurement of the Angular Coefficients of Drell-Yan e^+e^- pairs in the Z Mass Region from $p\bar{p}$ Collisions at $\sqrt{s} = 1.96$ TeV*, Phys. Rev. Lett. **106** (2011) 241801, arXiv:1103.5699 [hep-ex].

[26] CDF Collaboration, T. Aaltonen et al., *Indirect measurement of $\sin^2\theta_W(M_W)$ using e^+e^- pairs in the Z-boson region with $p\bar{p}$ collisions at a center-of-momentum energy of 1.96 TeV*, Phys.Rev.D (2013) , arXiv:1307.0770 [hep-ex].

[27] D0 Collaboration, V. Abazov et al., *Measurement of $\sin^2\theta^{\ell}_{\text{eff}}$ and Z-light quark couplings using the forward-backward charge asymmetry in $p\bar{p} \to Z/\gamma^* \to e^+e^-$ events with $\mathcal{L} = 5.0\, fb^{-1}$ at $\sqrt{s} = 1.96$ TeV*, Phys.Rev. **D84** (2011) 012007, arXiv:1104.4590 [hep-ex].

[28] M. Boonekamp, R. Caputo, G. Cattani, A. Di Ciaccio, A. Di Simone, G. Gaycken, S. König, E. Richter-Was, K. Schmieden, S. Schmitt, N. Wermes, M. Woudstra, and C. Zimmermann, *Measurement of the forward-backward asymmetry of Z/γ^* bosons decaying into electron and muon pairs with the ATLAS detector at $\sqrt{s} = 7$ TeV*, Tech. Rep. ATLAS-CONF-2013-043, CERN, Geneva, Apr, 2013.

[29] S. L. Glashow, *Partial Symmetries of Weak Interactions*, 1961. Nucl. Phys. **22** (1961) 579–588. Nucl. Phys. 22 (1961) 579.

[30] J. Goldstone, A. Salam, and S. Weinberg, *Broken Symmetries*, 1962. Phys. Rev. **127** (1962) 965–970. Phys. Rev. 127 (1962) 965.

[31] S. Weinberg, *A Model of Leptons*, 1967. Phys. Rev. Lett. **19** (1967) 1264–1266. Phys. Rev. Lett. 19 (1967) 1264.

[32] K. Nakamura et al. (Particle Data Group), *Review of Particle Physics*, J. Phys. G **37** (2010) 075021.

[33] H. Fritzsch, M. Gell-Mann, and H. Leutwyler, *Advantages of the Color Octet Gluon Picture*, 1973. Phys. Lett. **B47** (1973) 365–368. Phys. Lett. B47 (1973) 365.

[34] J. M. Campbell, J. W. Huston, and W. J. Stirling, *Hard Interactions of Quarks and Gluons: A Primer for LHC Physics*, 2007. Rept. Prog. Phys. **70** (2007) 89, arXiv:hep-ph/0611148. Rept. Prog. Phys. 70 (2007) 89.

[35] S. D. Drell and T.-M. Yan, *Massive Lepton Pair Production in Hadron-Hadron Collisions at High-Energies*, 1970. Phys. Rev. Lett. **25** (1970) 316–320. Phys. Rev. Lett. 25 (1970) 316.

[36] J. Stirling. http://www.hep.ph.ic.ac.uk/~wstirlin/plots/plots.html, Sep, 2013.

[37] P. M. Nadolsky et al., *Implications of CTEQ global analysis for collider observables*, Phys. Rev. **D78** (2008) 013004, arXiv:0802.0007 [hep-ph].

[38] A. Sherstnev and R. Thorne, *Different PDF approximations useful for LO Monte Carlo generators*, arXiv:0807.2132 [hep-ph].

[39] J. C. Collins and D. E. Soper, *Angular distribution of dileptons in high-energy hadron collisions*, Phys. Rev. D **16** (1977) 22192225.

[40] U. Baur, S. Keller, and W. Sakumoto, *QED radiative corrections to Z boson production and the forward-backward asymmetry at hadron colliders*, Phys. Rev. D **57** (1998) 199–215.

[41] U. Baur, O. Brein, W. Hollik, C. Schappacher, and D. Wackeroth, *Electroweak radiative corrections to neutral current Drell-Yan processes at hadron colliders*, Phys.Rev. **D65** (2002) 033007, arXiv:hep-ph/0108274 [hep-ph].

[42] CMS Collaboration, *Measurement of the weak mixing angle with the Drell-Yan process in proton-proton collisions at the LHC*, Phys.Rev. **D84** (2011) 112002, arXiv:1110.2682 [hep-ex].

[43] CMS Collaboration, *Forward-backward asymmetry of Drell-Yan lepton pairs in pp collisions at* $\sqrt{s} = 7$ *TeV*, Phys. Lett. **B718** (2013) 752–772, arXiv:1207.3973 [hep-ex].

[44] S. Weinberg, *New Approach to the Renormalization Group*, Phys. Rev. D **8** (Nov, 1973) 3497–3509. http://link.aps.org/doi/10.1103/PhysRevD.8.3497.

[45] J. Erler, *Tests of the Electroweak Standard Model*, arXiv:1209.3324 [hep-ph].

[46] G. P. Zeller et al., *Precise Determination of Electroweak Parameters in Neutrino-Nucleon Scattering*, Phys. Rev. Lett. **88** (Feb, 2002) 091802. http://link.aps.org/doi/10.1103/PhysRevLett.88.091802.

[47] SLAC E158 Collaboration, P. L. Anthony et al., *Precision Measurement of the Weak Mixing Angle in Møller Scattering*, Phys. Rev. Lett. **95** (Aug, 2005) 081601. http://link.aps.org/doi/10.1103/PhysRevLett.95.081601.

[48] C. Wood, S. Bennett, D. Cho, B. Masterson, J. Roberts, et al., *Measurement of parity nonconservation and an anapole moment in cesium*, Science **275** (1997) 1759–1763.

[49] MOLLER Collaboration, J. Mammei, *The MOLLER Experiment*, Nuovo Cim. **C035N04** (2012) 203–208, arXiv:1208.1260 [hep-ex].

[50] ALICE Collaboration, *The ALICE Experiment at the CERN LHC*, JINST **3** (2008) S08002.

[51] LHCb Collaboration, *The LHCb Experiment at the CERN LHC*, JINST **3** (2008) S08005.

[52] T. Sjostrand, S. Mrenna, and P. Z. Skands, *PYTHIA 6.4 Physics and Manual*, JHEP **05** (2006) 026, arXiv:hep-ph/0603175.

[53] G. Corcella et al., *HERWIG 6 : an event generator for hadron emission reactions with interfering gluons (including supersymmetric processes)*, Journal of High Energy Physics. **1** (2001) 010. http://dro.dur.ac.uk/1548/.

[54] P. Golonka and Z. Was, *PHOTOS Monte Carlo: A Precision tool for QED corrections in Z and W decays*, Eur.Phys.J. **C45** (2006) 97–107, arXiv:hep-ph/0506026 [hep-ph].

[55] S. Alioli, P. Nason, C. Oleari, and E. Re, *NLO vector-boson production matched with shower in POWHEG*, JHEP **0807** (2008) 060, arXiv:0805.4802 [hep-ph].

[56] S. Frixione and B. R. Webber, *Matching NLO QCD computations and parton shower simulations*, JHEP **0206** (2002) 029, arXiv:hep-ph/0204244 [hep-ph].

[57] GEANT4 Collaboration, S. Agostinelli et al., *GEANT4: A simulation toolkit*, Nucl. Instrum. Meth. **A506** (2003) 250–303.

[58] M. L. Mangano et al., *ALPGEN, a generator for hard multiparton processes in hadronic collisions*, JHEP **07** (2003) 001, arXiv:hep-ph/0206293.

[59] J. Butterworth, J. R. Forshaw, and M. Seymour, *Multiparton interactions in photoproduction at HERA*, Z.Phys. **C72** (1996) 637–646, arXiv:hep-ph/9601371 [hep-ph].

[60] J. Pumplin, D. Stump, J. Huston, H. Lai, P. M. Nadolsky, et al., *New generation of parton distributions with uncertainties from global QCD analysis*, JHEP **0207** (2002) 012, arXiv:hep-ph/0201195 [hep-ph].

[61] W. Bhimji, A. Buckley, P. Clark, R. Harrington, V. Martin, and ATLAS Collaboration, *The ATLAS Simulation Infrastructure*, The European Physical Journal C - Particles and Fields **C70** (2010) 823–874.

[62] E. Barberio et al., *Fast simulation of electromagnetic showers in the ATLAS calorimeter: Frozen showers*, Journal of Physics: Conference Series **160** (2009) no. 1, 012082. http://stacks.iop.org/1742-6596/160/i=1/a=012082.

[63] ATLAS, *Electron performance measurements with the ATLAS detector using the 2010 LHC proton-proton collision data*, EPJC **72** (2012) 1–46. 10.1140/epjc/s10052-012-1909-1.

[64] ATLAS Collaboration, J. Kretzschmar and L. Iconomidou-Fayard, *Electron performances measurements using the 2011 LHC proton-proton collisions*, Tech. Rep. ATL-COM-PHYS-2012-1024, CERN, Geneva, Jul, 2012.

[65] W. Lampl et al., *Calorimeter clustering algorithms: Description and performance*, . ATL-LARG-PUB-2008-002.

[66] W. Verkerke and D. P. Kirkby, *The RooFit toolkit for data modeling*, eConf **C0303241** (2003) MOLT007, arXiv:physics/0306116 [physics].

[67] ATLAS Collaboration, *Search for high-mass dilepton resonances in 4.2/fb of pp collisions at sqrt(s)= 8 TeV with the ATLAS experiment*, Tech. Rep. ATLAS-COM-CONF-2012-122, CERN, Geneva, Jun, 2012.

[68] ATLAS PDF forum, U. Klein. "private communication", 2012.

[69] T. Adye, *Unfolding algorithms and tests using RooUnfold*, arXiv:1105.1160 (2011) .

[70] G. D'Agostini, *A Multidimensional unfolding method based on Bayes' theorem*, Nucl. Instrum. Meth. **A362** (1995) 487–498.

[71] K. Schmieden, *Measurement of the Weak Mixing Angle and the Spin of the Gluon from Angular Distributions in the Reaction $pp \to Z/\gamma^* + X \to \mu^+\mu^- + X$ with ATLAS*. PhD thesis, Universität Bonn, Dec, 2012. Presented 22 Apr 2013.

[72] M. Whalley, D. Bourilkov, and R. Group, *The Les Houches accord PDFs (LHAPDF) and LHAGLUE*, arXiv:hep-ph/0508110 [hep-ph].

List of Figures

List of Tables

A. Monte Carlo inputs

This appendix contains the full list of Monte Carlo samples used in the analysis with the ATLAS specific production tags and event generation production numbers. The analysis uses Monte Carlo samples from the MC11c production campaign.

$Z \to ee$

- mc11_7TeV.106046.PythiaZee_no_filter.*.e815_s1272_s1274_r3043_r2993_p833 (10 M events for early studies)
- mc11_7TeV.106046.PythiaZee_no_filter.*.e815_s1272_s1274_r3043_r2993_p1035 (40 M events for later results)

Diboson

- mc11_7TeV.105985.WW_Herwig.*.e825_s1310_s1300_r3043_r2993_p833
- mc11_7TeV.105986.ZZ_Herwig.*.e825_s1310_s1300_r3043_r2993_p833
- mc11_7TeV.105987.WZ_Herwig.*.e825_s1310_s1300_r3043_r2993_p833

$t\bar{t}$

- mc11_7TeV.105200.T1_McAtNlo_Jimmy.*.e835_s1272_s1274_r3043_r2993_p833

$W \to e\nu$

- mc11_7TeV.107680.AlpgenJimmyWenuNp0_pt20.*.e825_s1299_s1300_r3043_r2993_p833
- mc11_7TeV.107681.AlpgenJimmyWenuNp1_pt20.*.e825_s1299_s1300_r3043_r2993_p833
- mc11_7TeV.107682.AlpgenJimmyWenuNp2_pt20.*.e825_s1299_s1300_r3043_r2993_p833
- mc11_7TeV.107683.AlpgenJimmyWenuNp3_pt20.*.e825_s1299_s1300_r3043_r2993_p833
- mc11_7TeV.107684.AlpgenJimmyWenuNp4_pt20.*.e825_s1299_s1300_r3043_r2993_p833
- mc11_7TeV.107685.AlpgenJimmyWenuNp5_pt20.*.e825_s1299_s1300_r3043_r2993_p833

$W \to \tau\nu$

- mc11_7TeV.107700.AlpgenJimmyWtaunuNp0_pt20.*.e825_s1299_s1300_r3043_r2993_p833
- mc11_7TeV.107701.AlpgenJimmyWtaunuNp1_pt20.*.e825_s1299_s1300_r3043_r2993_p833
- mc11_7TeV.107702.AlpgenJimmyWtaunuNp2_pt20.*.e825_s1299_s1300_r3043_r2993_p833
- mc11_7TeV.107703.AlpgenJimmyWtaunuNp3_pt20.*.e825_s1299_s1300_r3043_r2993_p833
- mc11_7TeV.107704.AlpgenJimmyWtaunuNp4_pt20.*.e825_s1299_s1300_r3043_r2993_p833
- mc11_7TeV.107705.AlpgenJimmyWtaunuNp5_pt20.*.e825_s1299_s1300_r3043_r2993_p833

$Z \to \tau\tau$

- mc11_7TeV.106052.PythiaZtautau.*.e825_s1356_s1353_r3043_r2993_p833

B. PDF Reweighting

PDF reweighting is used in this thesis to extract the value of $\sin^2\theta_W^{\text{eff}}$ and to estimate its error due to the uncertainty on the PDF. This section reports on the studies performed to validate the PDF reweighting using a special PYTHIA sample, that was generated at the truth-level (no detector simulation) using a different PDF set (*MSTW2008LO*).

The new sample contains two million events, and its dataset name is

- mc11_7TeV.129997.PythiaZee_no_filter_MSTW2008LO.evgen.*.e1578

The reweighting is performed using the method outlined in the ATLAS PDF reweighting twiki:

- *https://twiki.cern.ch/twiki/bin/viewauth/AtlasProtected/PDFReweight*

The version of the tool used to reweight D3PDs is *PDFTool_standalone-00-00-04*, which works in conjunction with the Les Houches Accord PDF Interface (LHAPDF) [72] version *LHAPDF-5.8.8*.

The PDF the PYTHIA signal Monte Carlo is using as default is listed in the LHAPDF sets as: MRSTMCal.LHgrid(20651), and the new PDF set used in the reweighting is MSTW2008lo68cl.LHgrid(21000). The tool is initialized with the following variables:

- beam energy
- input and output PDF
- PDF Scale (Z mass)
- the truth-level variables per event: x1, x2, id1, id2

Fig. B.1 shows the results of reweighting from *MRST* to *MSTW*, and from *MSTW* to *MRST*. As can be seen in the plots, the A_{FB} distributions agree well within statistical uncertainties.

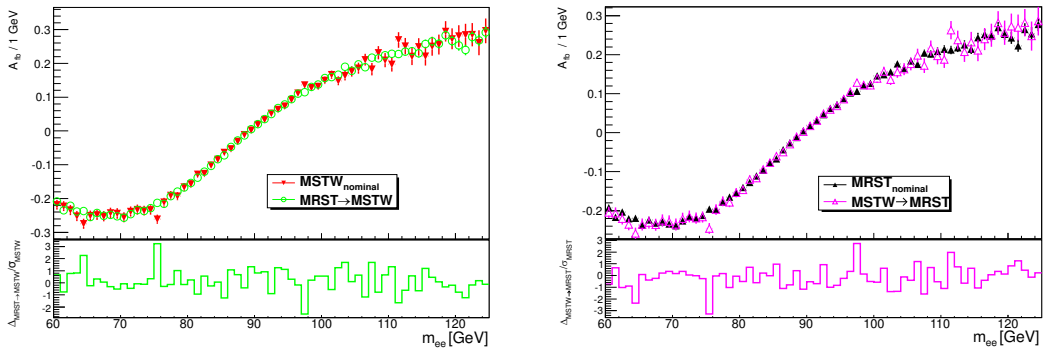

(a) (b)

Figure B.1.: Results of weighting the truth-level *MRSTMCal* default PYTHIA sample to the *MSTW2008LO* PDF (a). For completeness the *MSTW* to *MRST* conversion is also shown (b).

C. Energy scale tables

In this section the detailed tables of the forward electron energy calibration are collected.

η bin	Scale Factor [%] ± stat ± sys	Smearing Constant ± stat ± sys
$-4.90 < \eta < -4.00$	3.49 ± 0.26 ± 0.79	0.043 ± 0.006 ± 0.021
$-4.00 < \eta < -3.60$	1.54 ± 0.14 ± 0.28	0.032 ± 0.004 ± 0.011
$-3.60 < \eta < -3.35$	3.23 ± 0.17 ± 0.48	0.047 ± 0.004 ± 0.011
(crack) $-3.35 < \eta < -3.16$	−4.33 ± 1.69 ± 23.5	0.182 ± 0.013 ± 0.413
$-3.16 < \eta < -3.00$	0.31 ± 0.20 ± 0.25	0.039 ± 0.003 ± 0.016
$-3.00 < \eta < -2.90$	−0.02 ± 0.19 ± 0.50	0.022 ± 0.001 ± 0.011
$-2.90 < \eta < -2.80$	−0.30 ± 0.19 ± 0.23	0.036 ± 0.003 ± 0.037
$-2.80 < \eta < -2.70$	0.51 ± 0.25 ± 0.50	0.040 ± 0.004 ± 0.024
$-2.70 < \eta < -2.60$	3.29 ± 0.16 ± 0.30	0.017 ± 0.005 ± 0.030
$-2.60 < \eta < -2.50$	1.23 ± 0.20 ± 0.46	0.000 ± 0.015 ± 0.022
$2.50 < \eta < 2.60$	0.56 ± 0.16 ± 0.48	0.014 ± 0.013 ± 0.033
$2.60 < \eta < 2.70$	1.84 ± 0.17 ± 0.30	0.031 ± 0.003 ± 0.035
$2.70 < \eta < 2.80$	−0.87 ± 0.20 ± 0.55	0.047 ± 0.003 ± 0.024
$2.80 < \eta < 2.90$	−0.61 ± 0.19 ± 0.12	0.033 ± 0.004 ± 0.019
$2.90 < \eta < 3.00$	−0.06 ± 0.20 ± 0.42	0.031 ± 0.004 ± 0.021
$3.00 < \eta < 3.16$	−0.03 ± 0.20 ± 0.42	0.041 ± 0.003 ± 0.022
(crack) $3.16 < \eta < 3.35$	−4.12 ± 2.91 ± 34.6	0.164 ± 0.011 ± 0.522
$3.35 < \eta < 3.60$	2.45 ± 0.18 ± 0.41	0.041 ± 0.005 ± 0.016
$3.60 < \eta < 4.00$	0.23 ± 0.14 ± 0.28	0.044 ± 0.003 ± 0.014
$4.00 < \eta < 4.90$	2.65 ± 0.26 ± 0.63	0.036 ± 0.006 ± 0.056

Table C.1.: Scale factors and smearing constants per η bin for the forward electrons.

η bin	Statistics [%]	pile-up [%]	Fit range [%]	Fit variation [%]	Central ES [%]
$-4.90 < \eta < -4.00$	0.27	0.55	0.29	−0.16	0.46
$-4.00 < \eta < -3.60$	0.14	0.19	0.01	−0.03	0.19
$-3.60 < \eta < -3.35$	0.17	0.46	0.04	−0.01	0.11
(crack) $-3.35 < \eta < -3.16$	1.69	10.6	7.21	−13.5	14.4
$-3.16 < \eta < -3.00$	0.20	0.13	0.19	−0.08	0.08
$-3.00 < \eta < -2.90$	0.19	0.49	0.01	−0.03	0.07
$-2.90 < \eta < -2.80$	0.19	0.21	0.07	0.00	0.07
$-2.80 < \eta < -2.70$	0.25	0.42	0.24	−0.12	0.07
$-2.70 < \eta < -2.60$	0.16	0.30	0.01	0.00	0.05
$-2.60 < \eta < -2.50$	0.20	0.45	0.03	0.00	0.05
$2.50 < \eta < 2.60$	0.16	0.41	0.03	0.00	0.24
$2.60 < \eta < 2.70$	0.17	0.25	0.06	−0.03	0.15
$2.70 < \eta < 2.80$	0.20	0.49	0.22	0.01	0.11
$2.80 < \eta < 2.90$	0.19	0.10	0.02	−0.04	0.05
$2.90 < \eta < 3.00$	0.20	0.37	0.09	−0.05	0.18
$3.00 < \eta < 3.16$	0.20	0.29	0.24	−0.11	0.16
(crack) $3.16 < \eta < 3.35$	2.91	24.3	8.78	−18.9	13.2
$3.35 < \eta < 3.60$	0.18	0.23	0.07	0.01	0.34
$3.60 < \eta < 4.00$	0.14	0.18	0.01	0.03	0.21
$4.00 < \eta < 4.90$	0.26	0.51	0.10	−0.04	0.36

Table C.2.: Statistical and systematical uncertainties per η bin for energy scale for forward electrons.

η bin	Statistics [10^{-3}]	pile-up [10^{-3}]	Fit range [10^{-3}]	Fit Variation [10^{-3}]	Central ES [10^{-3}]	closure [10^{-3}]
$-4.90 < \eta < -4.00$	5.85	13.97	11.61	7.25	5.03	6.57
$-4.00 < \eta < -3.60$	3.58	3.52	3.55	1.30	4.44	8.16
$-3.60 < \eta < -3.35$	3.87	5.27	4.31	2.63	2.57	7.44
(crack)$-3.35 < \eta < -3.16$	13.25	337.25	103.37	182.09	85.48	74.35
$-3.16 < \eta < -3.00$	3.41	2.33	2.66	1.50	2.36	15.22
$-3.00 < \eta < -2.90$	1.33	6.83	0.46	0.20	6.42	5.31
$-2.90 < \eta < -2.80$	3.35	8.51	34.17	0.25	3.29	10.36
$-2.80 < \eta < -2.70$	3.99	9.16	2.12	2.37	4.53	21.59
$-2.70 < \eta < -2.60$	5.16	28.16	2.15	1.71	9.12	2.18
$-2.60 < \eta < -2.50$	15.10	9.51	5.88	1.03	18.19	5.18
$2.50 < \eta < 2.60$	13.08	22.66	1.74	0.54	18.53	15.79
$2.60 < \eta < 2.70$	3.14	23.99	1.68	0.10	5.85	25.29
$2.70 < \eta < 2.80$	2.94	5.20	2.32	0.16	3.21	22.76
$2.80 < \eta < 2.90$	3.70	3.75	1.85	2.52	1.86	17.98
$2.90 < \eta < 3.00$	4.19	9.85	1.86	1.92	2.78	18.42
$3.00 < \eta < 3.16$	3.29	6.91	4.83	3.34	2.46	20.15
(crack) $3.16 < \eta < 3.35$	11.45	321.22	214.53	163.85	310.59	0.00
$3.35 < \eta < 3.60$	5.15	10.14	3.96	7.89	3.62	8.82
$3.60 < \eta < 4.00$	2.83	3.50	7.60	2.85	1.74	10.85
$4.00 < \eta < 4.90$	6.48	52.92	5.68	1.43	4.62	16.45

Table C.3.: Statistical and systematical uncertainties per η bin for resolution for forward electrons.